universität wien

MASTERARBEIT / MASTER'S THESIS

Titel der Masterarbeit / Title of the Master's Thesis

"Petrogenesis of Triassic and Cretaceous metamorphic rocks from Khanom (Peninsular Thailand); thermo-barometry, monazite CHIME and zircon SIMS dating"

verfasst von / submitted by

Bernhard Neugschwentner, BSc

angestrebter akademischer Grad / in partial fulfilment of the requirements for the degree of

Master of Science (MSc)

Wien, 2021 / Vienna, 2021

Studienkennzahl lt. Studienblatt / degree programme code as it appears on the student record sheet:	A 066 815
Studienrichtung lt. Studienblatt / degree programme as it appears on the student record sheet:	Erdwissenschaften
Betreut von / Supervisor:	Ao. Univ. Prof. Mag. Dr. Urs Klötzli

Contents

List of Figures

List of Tables

Acknowledgement

This study could not have happend without the support of many people. Therefore I want to say thank you to all of them who supported me during this path. First of all Urs Klötzli my supervisor, who proposed me this exciting topic and gave me the chance to travel on the other side of the globe, to work on interesting new problems. Furthermore he always supported and encourged me at any time and taught me a lot over the years. A special thanks goes to Michael Oester who not only joined the field trip in Thailand, but also for lending an ear for questions and for proofreading and corrections. I also want to thank the University of Vienna and the Chulalongkorn University, Bangkok, as without their collaboration and financial support this study would not exist. A special thanks goes to Pitsanupong Kanjanapayont who managed and organized the trip in Thailand and also gave a lot of geological input during the field trip. Another thank you goes to Franz Biedermann who initiated me into the art of zircon and monazite separation. In addition I want to thank Igor Broska and Patrik Konečný who invited me to Bratislava to join the CHIME-dating method. Finally I want to thank my family, especially my parents, who always supported me.

1. Introduction

The Khanom metamorphic complex, located approximatly 70 km east of Surat Thani on the western coast of the Gulf of Thailand, is part of the Khao Luang batholith and consists mainly of granits, gneisses and schists (Kosuwan 1996). This complex, which is part of the crystalline basement rocks in Thailand, was subject of only a few studies in recent years (Hansen and Wemmer 2011, Kawakami et al. 2014, Sautter et al. 2017 and Sautter et al. 2019). Crystalline basement rocks found all over Thailand are typically high metamorphic and were initially thought to be of Precambrian age because of the Paleozoic sediments surrounding these rocks. Several geochronological data from various studies (e.g. Ahrendt et al. 1993, Lacassin et al. 1997) soon disproved this assumption, showing predominantly Middle-Late Triassic, Late Cretaceous and Paleogene ages. A model for the tectonic evolution of Thailand was derived, wherein the collision between Sibumasu and Indochina in the Middle-Late Triassic and the collision of the Indian plate with the Asian plate in the Paleogene are key moments (see chapter 2). This theory is now well accepted. However, it was established on the basis of data which almost exclusively come from the northern part of Thailand. The continuation of crystalline basement rocks belonging to Sibumasu towards the Malay Peninsular is thought to be realistic, but only little data are available to support this. The aim of this study was to gather petrological, geochemical and geochronolical data which can contribute to the assumption that high metamorphic basement rocks found in Peninsular Thailand have the same metamorphic and tectonic evolution as their northern counterparts. For this reason Al-in-hornblende barometry coupled with hornblende-plagioclase thermometry and Monazite–xenotime miscibility gap thermometry as well as in-situ CHIME (chemical Th–U–total Pb isochron method) monazite and SIMS (secondary-ion mass spectrometry) zircon dating were applied.

2. Geological setting

Thailand is located on the geological entity called Sundaland, which consists of Gondwana derived continental plates accreted over time to build the present mainland of SE-Asia (see fig. 2.1). Sundaland, bordered in the SE by the limit of continental crust and in the NW by major Cenozoic strike–slip faults (Ailao Shan–Red River shear zone and Sagaing fault), is moving eastward with respect to Eurasia and rotating clockwise (Searle and Morley 2011). Two main blocks of Sundaland, Sibumasu in the west and Indochina in the east, are located in Thailand. Although both have their origin in Gondwana they show a different history. While Sibumasu shows typical Permian sedimentation with warm water fauna, Indochina has a cooler water fauna sedimentation and exhibits glacial marine diamictites.

2.1. Paleozoic evolution

The Paleozoic evolution is dominated by the successive dispersion and amalgamation and accretion of Gondwana derived blocks. This is thought to have happened in three phases which opened and subsequently subducted three Tethyan oceans, Palaeo-Tethys (Devonian–Triassic), Meso-Tethys (Early Permian–Late Cretaceous) and Ceno-Tethys (Late Triassic–Late Cretaceous)(Metcalfe 2013). The subduction of the Palaeo-Tethys resulted in the collision of Sibumasu and Indochina. This collision which is thought to have happened between the Late Permian until the Late Triassic, where it reached its maximum, is also known as Indosinian Orogeny (see fig. 2.2). Between these two continental blocks lies the Inthanon Zone (Changning-Menglian suture, Chiang Mai-Inthanon suture, Bentong-Raub suture) and the Sukhothai Zone (Lincang terrane, Sukhothai terrane, Chantaburi terrane, Central and Eastern belts of the Malay Peninsula)(Metcalfe 2013). The latter is interpreted as a volcanic arc developed on rifted fragments of the Indochina block, probably separated in the Carboniferous by a back-arc basin (now represented by the Nan-Uttaradit sutur)(Metcalfe 2013), due to subduction of the Palaeotethys under Indochina. The Inthanon Zone is assumed to be a accretionary wedge where Palaeotethyan rocks (pelagic cherts and basaltic seamounts with carbonate caps) have been thrusted as nappes along a low-angle fault over sedimentary rocks of Sibumasu (Searle and Morley 2011, Metcalfe 2013, Hansen and Wemmer 2011, Hutchison 2014). Whereas the exact location of these zone of collision is still under debate its alignment is presumed N-S. (Ridd et al. 2011). Along a N-S trending line also several granitoid intrusions occurred during that time (Cobbing 2011, Searle et al. 2012)(see fig.2.4).

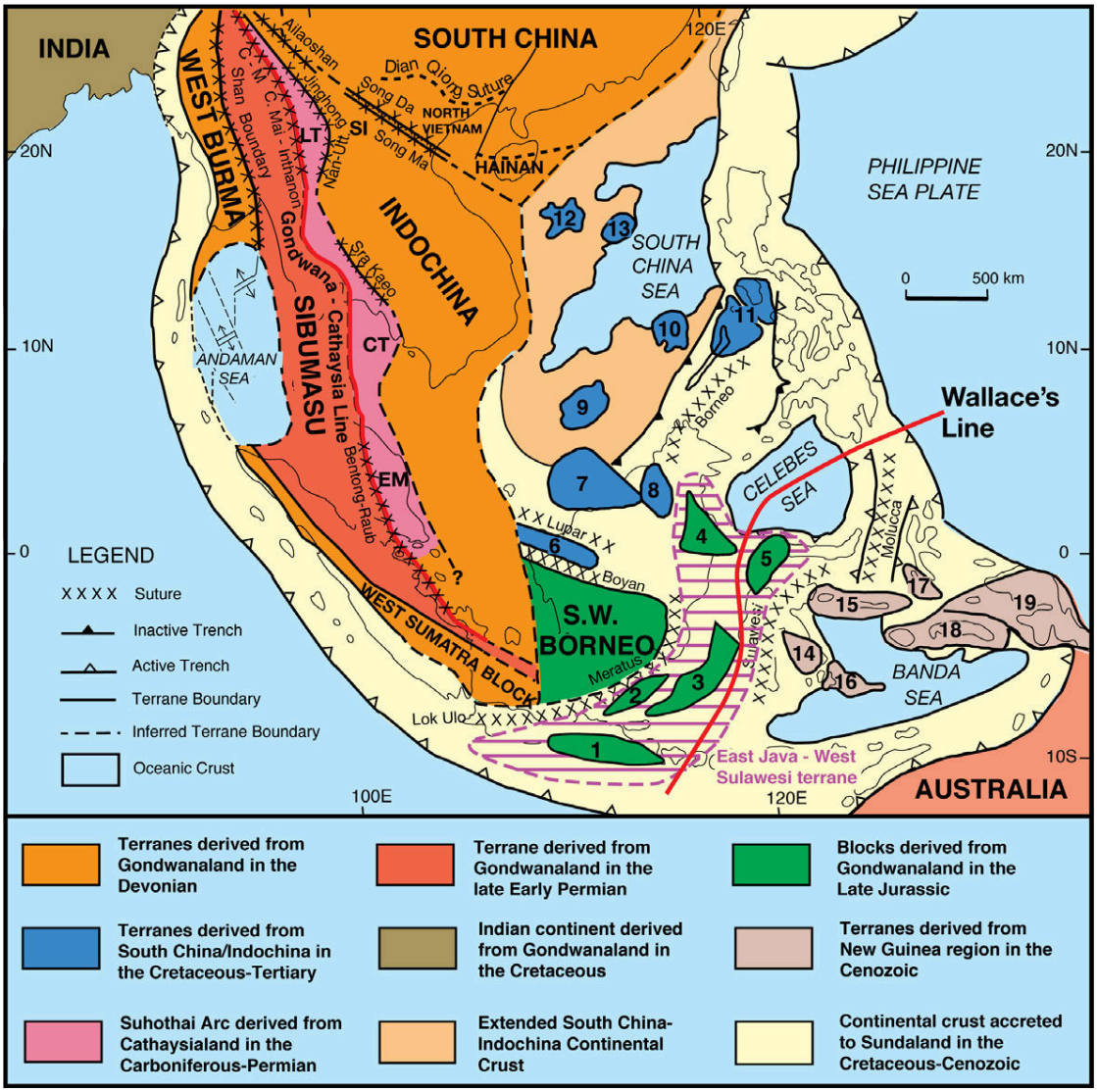

Figure 2.1.: Distribution of continental blocks, fragments and terranes, and principal sutures of Southeast Asia. Numbered micro-continental blocks, 1. East Java; 2. Bawean; 3. Paternoster; 4. Mangkalihat; 5. West Sulawesi; 6. Semitau; 7. Luconia; 8. Kelabit–Longbowan; 9. Spratly Islands–Dangerous Ground; 10. Reed Bank; 11. North Palawan; 12. Paracel Islands; 13. Macclesfield Bank; 14. East Sulawesi; 15. Bangai–Sula; 16. Buton; 17. Obi–Bacan; 18. Buru–Seram; 19. West Irian Jaya. LT = Lincang terrane, ST = Sukhothai terrane and CT = Chanthaburi terrane, EM = East Malaya. C–M = Changning–Menglian suture, C.-Mai = Chiang Mai suture, and Nan–Utt. = Nan–Uttaradit suture. After Metcalfe (2013)

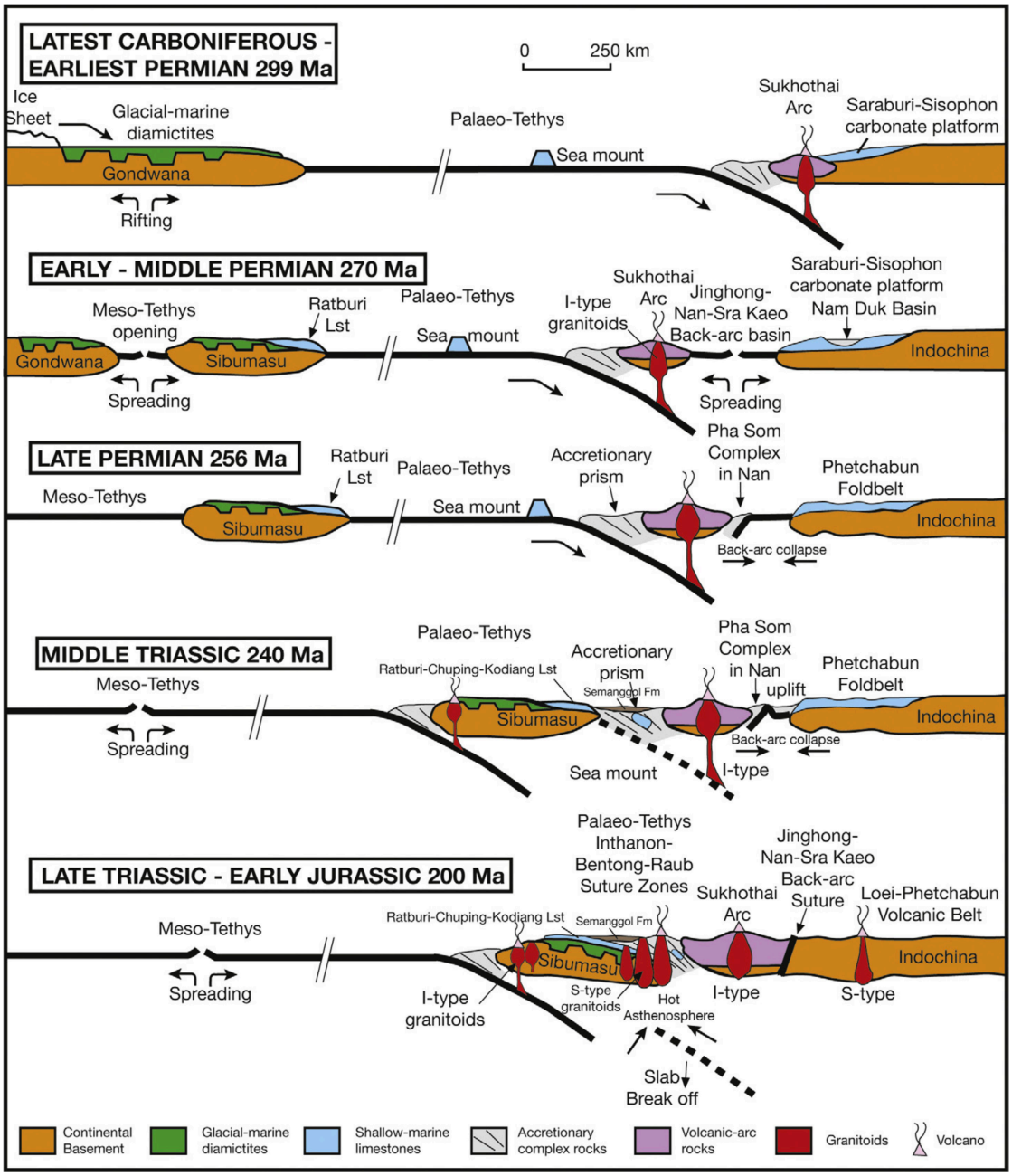

Figure 2.2.: Cartoon showing the tectonic evelution of Sunderland. After Metcalfe (2013)

2.2. Mesozoic evolution

After the accretion of SE-Asia a time of tectonic quiescence occured in the early Jurassic until the Cretaceous. In this time shallow marine sediments formed in the western part of Thailand while in the eastern part continental sediments were deposited. Today the continental sedimentation is known as the Khorat Plateau, which is located in the north-east of the country (see fig2.4).
The quiescence ended with the subduction of the Meso-Tethys beneath Sunderland, which reached its maximum in the Late-Cretaceous. This was accompanied by granite intrusions and intensified deformation (Ridd et al. 2011, Metcalfe 2013).

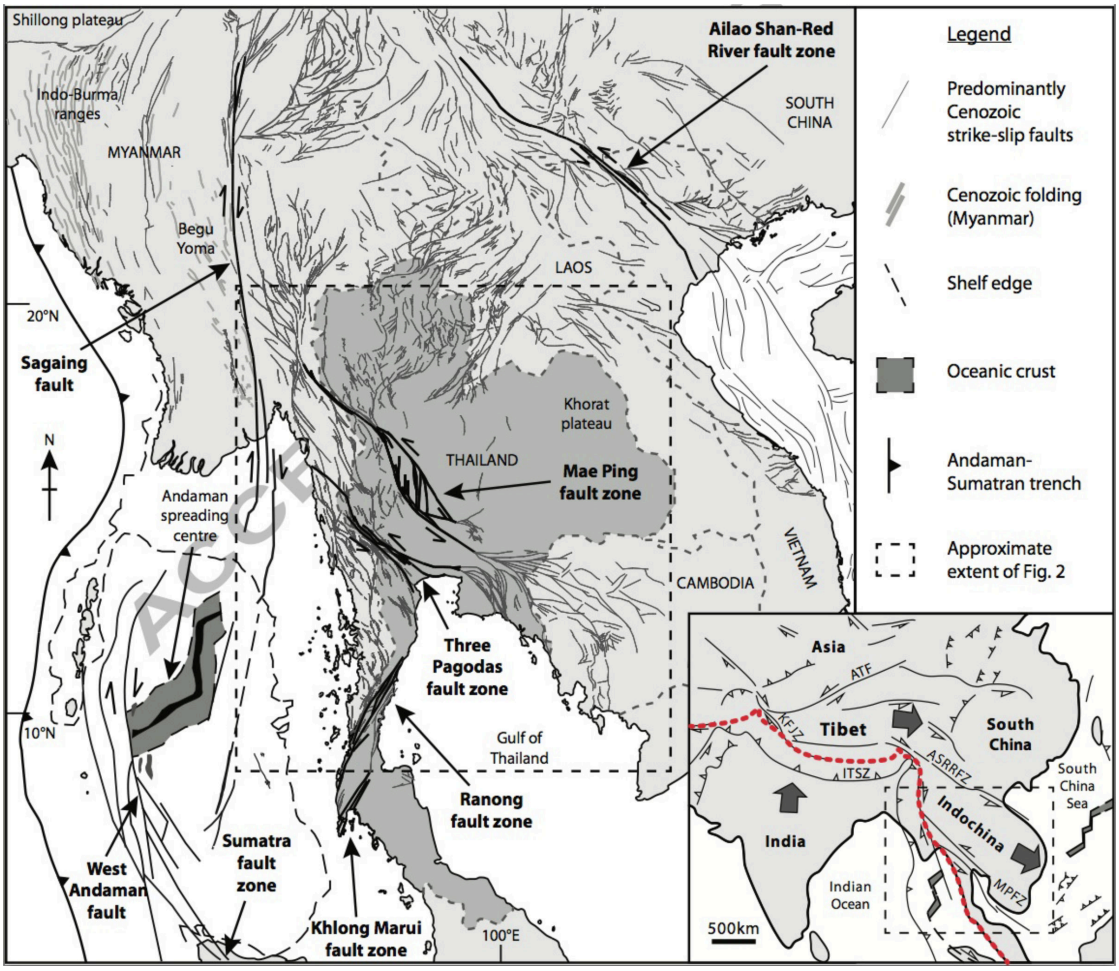

Figure 2.3.: Simplified tectonic map of SE-Asia showing regional fault patterns. ITSZ, Indus–Tsangpo suture zone (approximate position marked by bold dashed line); ATF, Altyn Tagh fault; KFJZ, Karakoram–Jiale fault zone; ASRRFZ, Ailao Shan– Red River fault zone; MPFZ, Mae Ping fault zone. After Palin et al. (2013)

2.3. Cenozoic evolution

The Cenozoic Evolution of Thailand is dominated by the collision of India with Eurasia. However the timing of this event is still under debate. While some authors prefer that the collision took place in the Late Cretaceous-Early Paleocene others prefer a much younger Eocene-Oligocene collision age (Metcalfe 2013). Recent studies by Searle (2018) however suggest rather a time period, of 15 Ma starting around 65 Ma until around 37 Ma. This event includes three separate subduction zones. In SE-Asia this collision lead to lateral extrusion along major strike-slip faults (Tapponnier et al. 1982). It is widely accepted that the N–S striking dextral Sagaing fault in Myanmar and the NW–SE striking sinistral Ailao Shan–Red River shear zone in China take up most of the lateral movement. The amount of lateral displacement is still under debate.
In Thailand four prominent strike slip faults, which are assumed to have part in the lateral extrusion, occur. In the west are the NW–SE striking sinistral Mae Ping and Three Pagodas shear zones, and in the south are the NE–SW striking dextral Ranong and Khlong Marui shear zones (see fig.2.3). Some authors (Palin et al. 2013) suggest, that the Mae Ping and the Three Pagodas fault zones splay out from the Sagaing fault, but the area in which they should merge is poorly documented. Furthermore the conjunction of the Mae Ping with the Klaeng fault zones and the Three Pagodas with the Ranong fault zone is still under debate (Morley et al. 2011).
A second dominant structural feature in the geology of Thailand are the abundant intramontane pull-apart basins which are also a result of Cenozoic processes. While for some authors the link between the fault zones and the basins is obvious, Morley et al. (2011) state the fault zones were active prior the formation of the basin and therefore another mechanism must be responsible for their occurrence. The authors suggest subduction-rollback as the major process for the formation of these basins and induce that strike-slip faulting played only a minor part. In addition they introduced the idea that subduction-rollback could have played a role in the genesis of metamorphic core complexes in Thailand (e.g. Doi Inthanon).
A recent study from Sautter et al. (2017) at the Malay Peninsular, tries to connect on- and offshore data to shed light on the transition from a late stage orogeny into the development of subsequent continental rifting. In their model the evolution of rifting is controlled by the presence and migration of a free edge (path of India) and the existence of a strong backbone (Malay Peninsula) separating two basin geometries. It took place in three stages including deposition of continental sediments in pre-existing depressions (Maastrichtian/Paleocene), followed by rifting along N-S faults branching on pre-existing segments of NW-SE shear zones (Upper Eocene - Lower Miocene) and finally a deepening of depocentres in the lateral regions (Andaman and Malay Pattani basins). The following study from Sautter et al. (2019) displays a compilation of thermochronological and geological data from various metamorphic core complexes located on a N-S transect in west Sundaland. These data suggest the same succession of events (HT metamorphic event, post-kinematic intrusion, exhumation and rifting),

whereas ages get younger northwards, which can be linked to the northward motion of the Indian Plate. Further studies are needed to verify or disprove these models.

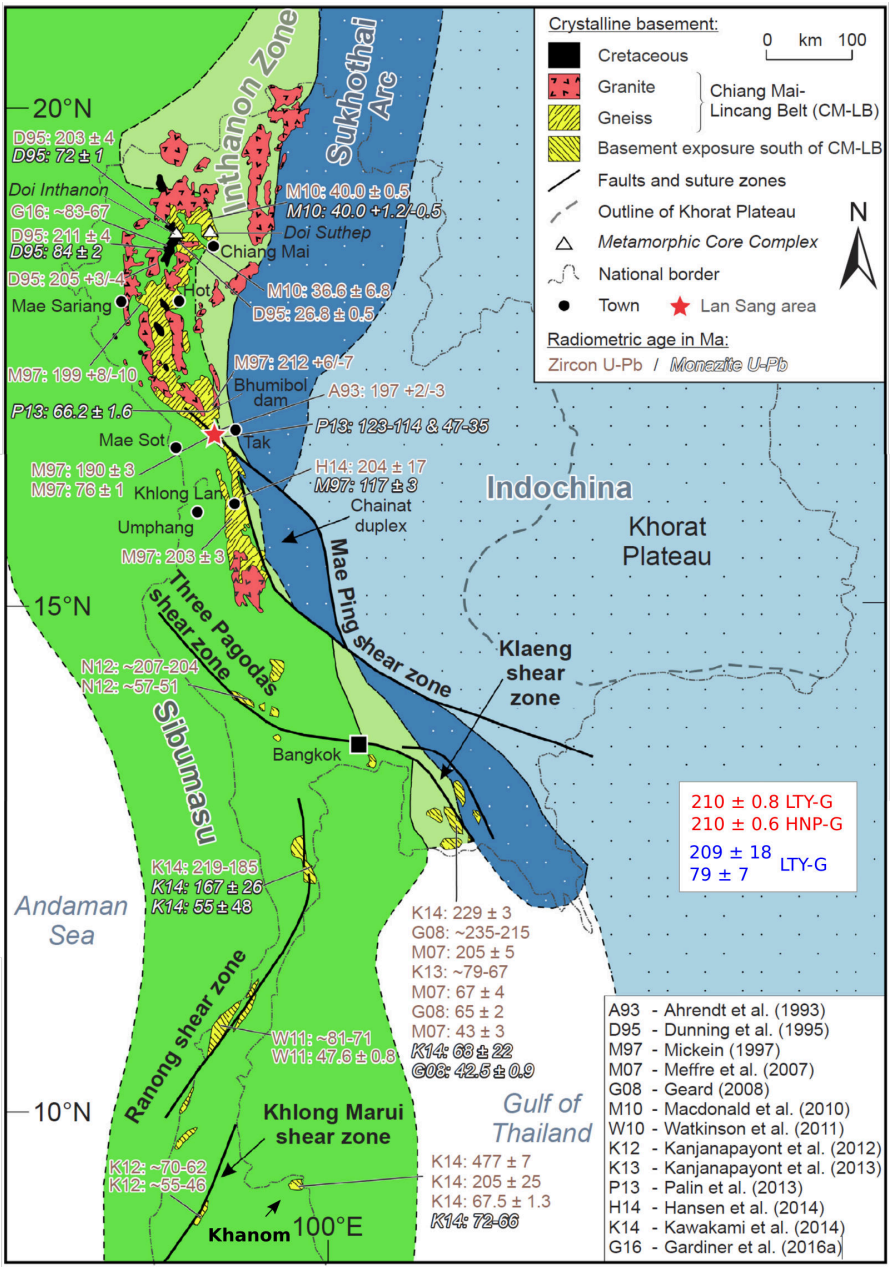

Figure 2.4.: Simplified geological map after Österle et al. (2019), showing terranes of Thailand and outcropping crystalline basement. Age data from this study are given by the red (zircon $^{206}Pb/^{238}U$) and blue (monazite CHIME) numbers.

2.4. Khanom complex

The Khanom complex was first described in detail by Kosuwan (1996) and is located between two faults which are named Khanom fault and Sichon fault (see fig.2.5). The contact with surrounding sedimentary units is covered by thick Quaternary sediments and dense vegetation.
Kosuwan (1996) distinguished 5 units. He described two granites, an older foliated garnet-bearing two mica granite (Khao Dat Fa granite) and a younger finer grained biotite granite (Khao Pret granite). In this work, the Khao Dat Fa granite is referred to as Khao Dat Fa gneiss because it is older than the gneisses in this area and has therefore undergone the same gneiss-forming process(es). At the borders of these granites garnet-bearing muscovite schists and quarzite are intercalated with calc-silicate and marble lenses (Khao Yoi schist).
Furthermore two gneisses where described. The first is a biotite and biotite-sillimanite gneiss (Haad Nai Phlao gneiss), occuring in alternating layers, with differences in grain size. He mentioned that the fine-grained layers are equigranular and the coarse-grained are more porphyroblastic. This gneiss also shows calc-silicates. Furthermore it is thought, that this gneiss would be of sedimentary origin.
The other gneiss is a biotite bearing augengneiss (Laem Thong Yang gneiss), which he classified as orthogneiss. Even tough they show the same structural overprint, the relation and contact between these gneisses remained unsolved. Despite his lack of geochronological data he assumed that the Khanom complex is of Lower Paleozoic or Precambrian age.
First attempts to date these rocks were made by Hansen and Wemmer (2011). U/Pb ages obtained by zircon multigrain analyses were carried out on an amphibol-bearing gneiss from the Khao Phra mountain. The data yield an upper intercept of 452 -84 Ma / +93 Ma (Late Ordovician) and a lower intercept of 45 -18 Ma / +12 Ma (Eocene). While the Eocene age was interpreted as a strong thermal pulse or high-temperature metamorphism without significant deformation, the meaning of the Late Ordovician age remained unsolved. The following study by Hansen et al. (2014), which used SHRIMP analyses of zircons on the same samples, gave a slightly older Paleocene age of 56.45 ± 0.72 Ma. The Late Ordovician age however could not be reproduced. Only a few concordant ages between 178 and 612 Ma could be obtained from the cores. Further research was carried out by Kawakami et al. (2014) using LA-ICP-MS U/Pb zircon and CHIME monazite dating. U/Pb zircon dating yielded a concordia age of 67.5 ± 1.3 Ma for the Khao Pret granite and a weighted average age of 477 ± 7 Ma for the Khao Dat Fa gneiss. The CHIME monazite dating yielded negative intercept ages which are highly controversial and therefore not very reliable. The authors interpret the older Ordovician age as evidence that the basement rocks of Sibumasu were formed during the Pan-African Orogeny. Therefore an Ordovician continental crust beneath the sedimentary rocks is still present. The Late Cretaceous age was interpreted as time of crystallisation. Whether this assumption is true or not is still matter of debate.
Sautter et al. (2019) present Fission track ages from zircons (ZFT) and apatites (AFT),

from the Haad Nai Phlao gneiss (ZFT: 33.5 ± 1.4 Ma; AFT: 24.6 ± 1.1 Ma) and the Khao Pret granite (ZFT: 32.9 ± 1.6 Ma; AFT: 17.9 ± 1.1 Ma). In addition modeling of the thermal history on confined horizontal tracks was done on the sample from the Haad Nai Phlao gneiss. The result revealed fast cooling from 36-26 Ma (23°C/Ma), which is related to strong tectonic-controlled exhumation, followed by lower to moderate cooling from 27-22 Ma (12°C/Ma). Afterwards cooling is assumed with rates lower than 2°C/Ma, which is considered being related to pure erosional unroofing processes.

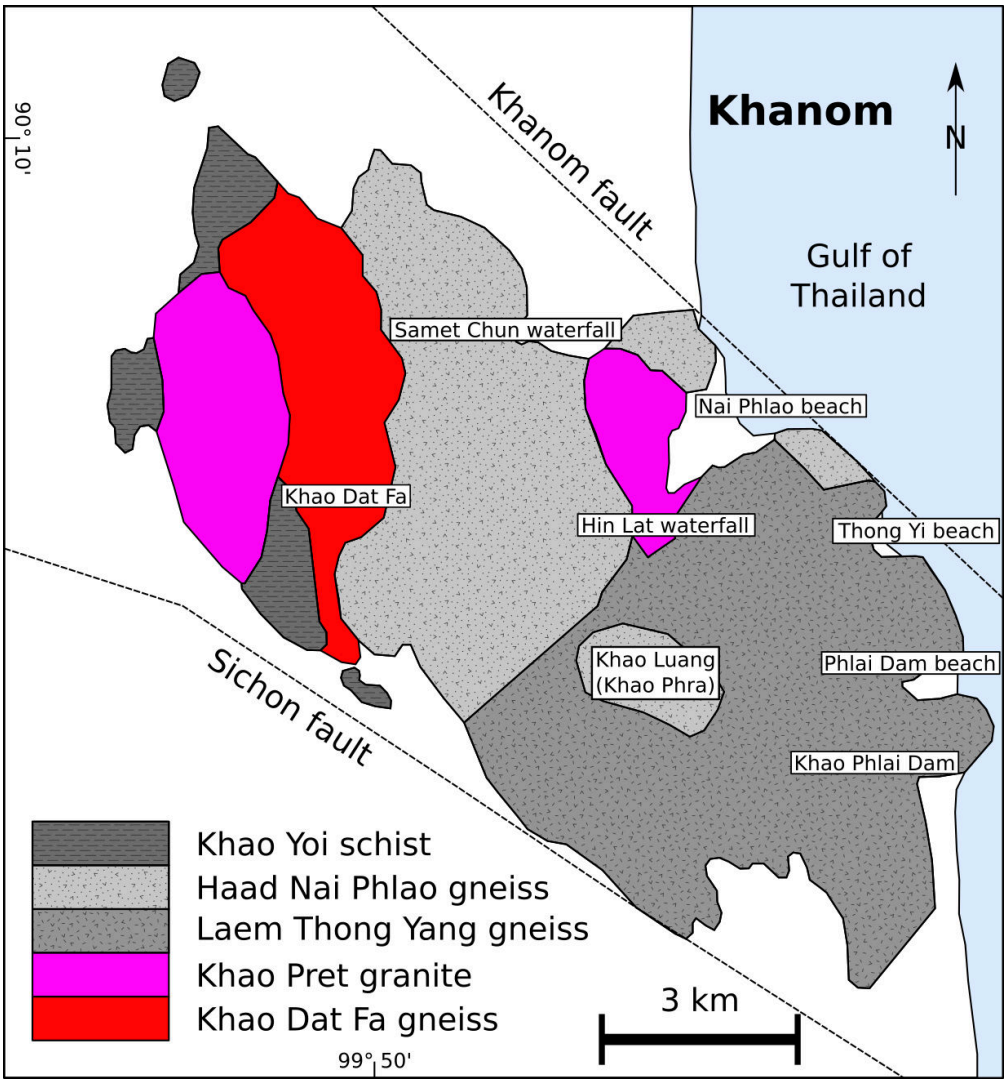

Figure 2.5.: Geological map of the Khanom area after Kosuwan (1996) and Kawakami et al. (2014)]

3. Fieldwork

Field-investigations were carried out from 18-22 February 2016. Most of the investigated outcrops were located along the coast, from Haad Nai Phlao in the north to Laem Thong Yang in the south, or along riverbeds (Hin Lad waterfall, Samet Chun waterfall)(see fig.2.5). Due to heavy vegetation or steep elevation it was not possible to follow riverbeds for a greater distance to obtain cross-sections. Apart from the coastline or riverbeds outcrops were hard to find or inaccessible because most of the area is jungle-covered. Quality of most outcrops suffered due to heavy weathering. Sample taking for petrological, geochemical and geochronological purpose were carried out in a traditional manner using hammer and chisel. Furthermore a GPS-device and field-compass were used for localization and taking measurements (see Appendix A).

3.1. Lithologies

The gneisses in Khanom were first characterized in detail by Kosuwan (1996). There were two gneiss units distinguished, the Haad Nai Phlao gneiss and the Leam Thong Yang gneiss. All gneisses in this area show a similar structural overprint with a foliation striking NW-SE and dipping 55° NE (see table A.2). The relationship between these two gneisses however remained unknown.
Furthermore one outcrop of a very fine-grained mylonite in the south of the Khanom complex was observed. In addition a small conglomerate boulder of blueshist and amphibolite facies units could be observed at Hin Lad waterfall. The Khao Dat Fa gneiss and Khao Pret granite as well as the Khao Yoi schist, which were discribed by Kosuwan (1996) are not discussed in this work.

3.1.1. Haad Nai Phlao gneiss (HNP-G)

Outcrops of the HNP-G can be found in northern an north-eastern part of the Khanom complex around Nai Phlao beach and Samet Chun waterfall. It is composed of coarse-grained and fine-grained biotite-gneiss. The relation between coarse-grained and fine-grained gneiss is not quite certain. On the one hand they occur in alternating successions whereas occasionally a gradual transition can be observed (see fig. 3.1), on the other hand the contact is not parallel to the shistosity but rather cuts discordantly through (see fig. 3.2). Whereas the layering might indicate a sedimentary origin of the gneiss, the other contact apparently is magmatic. The alternating layers usually have a thickness from a few centimetres to several decimetres. Single layers of some

metres where also observed. Furthermore intercalating of fine-grained, fine-laminated white-greenish calcsilicate can be observed, but this seems to be rather rare.

Figure 3.1.: Layered transition HNP-G

Figure 3.2.: Magmatic transition HNP-G

The coarse-grained HNP-G (see fig. 3.3) is characterised by porphyroblastic textures. K-Feldspar and Quarz blasts (in cm-scale) are floating in a matrix consisting of biotite, quartz and plagioclase. Furthermore a S-C-fabric could be observed. There are also pegmatite and aplite veins ranging from few centimeters up to a meter cutting through the coarse-grained HNP-G.

Figure 3.3.: Coarse-grained HNP-G showing porphyroblastic texture and S-C-fabric

Figure 3.4.: Fine-grained HNP-G showing dark elongated enclaves

The fine-grained HNP-G has darker and lighter layers and also elongated dark enclaves (see fig. 3.4). Furthermore it is more equigranular than the coarse-grained HNP-G. It is also mentionable that there were no pegmatites or aplites observed in the fine-grained HNP-G. In addition the foliation sometimes shows a slaty greenish

structure, which implies a late greenschist facies overprint.

3.1.2. Laem Thong Yang gneiss (LTY-G)

Furthermore a coarse-grained "augengneiss" occurs in the southern area of the Khanom complex at Thong Yi beach, Hin Lat waterfall, Khao Phlai Dam and Phlai Dam beach. Feldspar, quartz, biotite are the main components. Rectangular K-Feldspar blasts represents the "augen" and quartz, biotite and plagioclase the matrix. One of the main differences between the Laem Thong Yang gneiss and the coarse-grained Haad Nai Phlao gneiss is that the former is less deformed, has no quartz blasts and the K-feldspar are overall more rectangular. In addition there is less quartz and almost no white mica in the Laem Thong Yang gneiss (see fig. 3.5).

Figure 3.5.: LTY-G with rectangular K-feldspar blasts

Figure 3.6.: Contact LTY-G - L-G

3.1.3. Leucocratic gneiss (L-G)

The L-G occurs at Thong Yi beach and Hin Lad waterfall. This gneiss was not described by Kosuwan (1996), probably because of its minor expanse. It manly consist out of feldspar, quartz and white mica with a minor amount of biotite. It is mostly equigranular and is less strongly deformed, but it shows the overall overprint which can be found in all gneisses of the Khanom complex. The contact between LTY-G and L-G is clearly magmatic, where apophyses can be observed (see fig. 3.6).

3.1.4. Mylonite

This lithology at the southern border of the Khanom complex occurres only in one outcrop. It has fine layers of a dark greenish and brighter greyish rock types (see fig. 3.7). These layers range from some millimetres to a few centimetres in width. Pegmatites cut through this mylonite and are also strongly deformed. Some measurements of these layers show a strike NW-SE with a steep dip of ∼80° SW.

3.1.5. Conglomerate (not in-situ)

This interesting conglomerate with elongated cobbled sized clasts was only observed as boulder at Hin Lad waterfall (see fig. 3.8). Nevertheless it must be found as exposed rock further up in the drainage basin of the river. Matrix is greyish-brown in colour and very fine-grained. Individual minerals could not be determined. Clasts can be divided in two lithologies: one is darker bluish with abundant amphiboles and almost no quartz and feldspar, the other is also amphibole bearing but has more quartz and feldspar content.

Figure 3.7.: Mylonite with darker greenish and brighter greyish layers

Figure 3.8.: 'Conglomerate' with dark blueish and grey-blueish clasts in grey brownish matrix

4. Petrology

A set of petrological methods was used to describe the structures, textures and chemical composition of the samples, including optical microscope (OM), scanning electron microscope (SEM) and electron microprobe analysis (EMPA), to get a further understanding regarding the composition of lithologies and its evolution. For this reason 19 thinsections, for both OM and SEM, were studied.

4.1. Microscopic petrography

4.1.1. Augengneiss (LTY-G)

The mineral assemblage of the augengneiss is K-feldspar (40-50%), quartz (25-30%), plagioclase (15-20%) and biotite (5-10%). Other minor constituents are apatite, white-mica, illmenite, zircon, monazite and xenotime. The texture is porphyric, with big K-feldspar (and sometimes plagioclase) "augen", which are up to a few centimetres in size. The matrix consists of finer grained quartz, plagioclase and biotite, whereas the orientation of biotite grains defines the foliation. Apart from some big K-feldspar clasts and biotite, grains are rather anhedral. K-feldspars often show Karlsbarder twinning (see fig.4.1), microcline twinning, perthitic exsolutions and recrystallisation on rims. Furthermore bigger and smaller inclusions of quartz, plagioclase, biotite, apatite, monazite and zircon could be found within the K-feldspars. Plagioclase is characterized by polysynthetic twinning, relictic zonation and sometimes strong sericitic alteration. On the contact between K-feldspar and plagioclase myrmekites, which replace K-feldspars could be observed. Quartz grains show dynamic recrystallisation, which is characterized by patchy undulose extinction, grain boundary migration and sometimes weak shape preferred orientation (SPO). Biotite shows the typical brownish-greenish pleochroism and pleochroic halos around zircon and monazite grains. Most of the zircons and monazite are associated with biotite-clusters. In addition, paragenesis of zircon, monazite and xenotime, which are in contact with each other, could be observed.

4.1.2. Coarse-grained HNP-G

The analysed thinsections show many similarities between the LTY-G and the coarse grained HNP-G. The mineral assemblage consists of K-feldspar (35-45%), quartz (25-30%), plagioclase (15-20%) biotite (5-10%) and white mica (<5%). Minor constituents are apatite, illmenite, zircon, monazite and xenotime. Thus it is comparable to the

LTY-G with slightly more biotite and white mica in the coarse-grained HNP-G. Although the K-feldspar blasts are generally not as big and less euhedral, a porphyric texture is noticeable. Minerals are rather anhedral, apart from mica grains which also define the foliation. Feldspars often show sericitization, while plagioclase sometimes polysynthetic twinning (see fig.4.2). Quartz is characterized by dynamic recrystallisation. Karlsbarder twinning of K-feldspars is not as dominant as in LTY-G. Biotite also shows the typical brownish-greenish pleochroism and pleochroic halos around zircon and monazite grains. Monazites and zircons are commonly associated with biotite clusters.

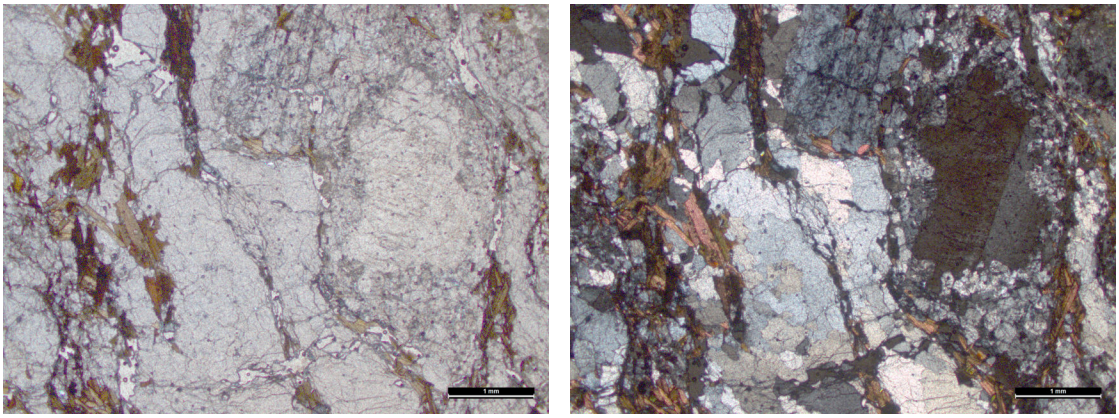

Figure 4.1.: Left: image showing the texture of the augengneiss; right: same picture (crossed-polarized) showing a strongly altered K-feldspar 'auge' with Karlsbarder twinning; TH1608A_1

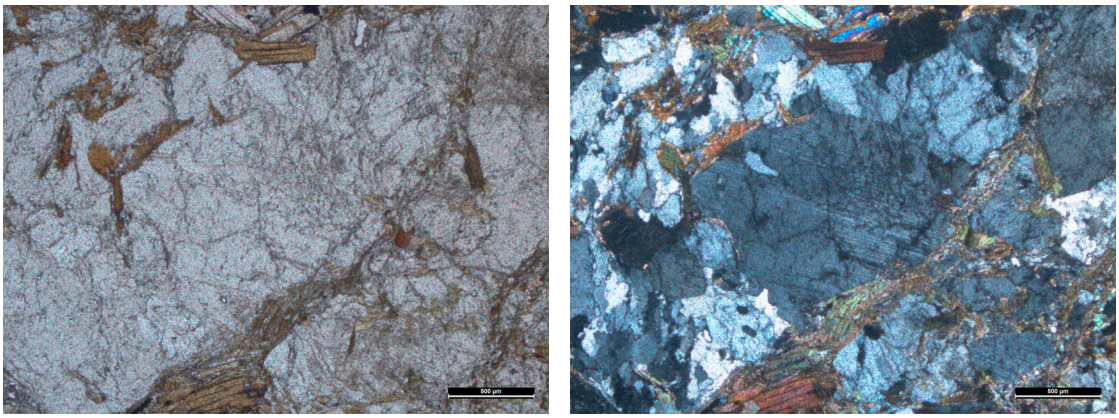

Figure 4.2.: Left: image showing the texture of the coarse grained HNP-G; right: same picture (crossed-polarized) showing polysynthetic twinn lamella from a plagioclase; TH1612C_1

4.1.3. Biotite gneiss (HNP-G)

The main constituents are K-feldspar (35-45%), quartz(25-30%), plagioclase (20-25%), biotite (5-10%), white mica (<5%). Minor constituents are apatite, illmenite, zircon, monazite (see fig.4.3) and xenotime. Grain sizes are distributed equigranularly and crystal borders are anhedral to subhedral. Quartz and biotite can show a shaped preferred orientation. K-feldspars can have crystals up to one millimetre and some of these grains are evocative of porphyric texture. Perthite exsolution could also be observed. Plagioclase is characterised by twin lamellae and sericitic alteration. Quartz grains are often elongated, show undulose extinction and dynamic recrystallisation (bulging, subgrains).

4.1.4. Amphibole-bearing gneiss (HNP-G)

The texture is similar to the biotite gneiss and the mineral assemblage is composed of quartz (20-30%), plagioclase (20-30%), K-feldspar (15-20%), Biotite (5-10%), hornblende (5-10%) and clinozoisite (<5%). Minor constituents are allanite, titanite, chlorite and zircon. Plagioclase shows the typical polysynthetic twinning and sometimes kink bands (see fig.4.4) and undulose extinction. Weak sericitic alteration was also observed. Biotite is marked by chloritisation. Furthermore zonation in plagioclase and allanite grains is visible. Quartz shows strong undulose extinction and dynamic recrystallisation. Its mentionable that no monazites could be found but zircons are abundant although their grain size is rather small (<50µm).

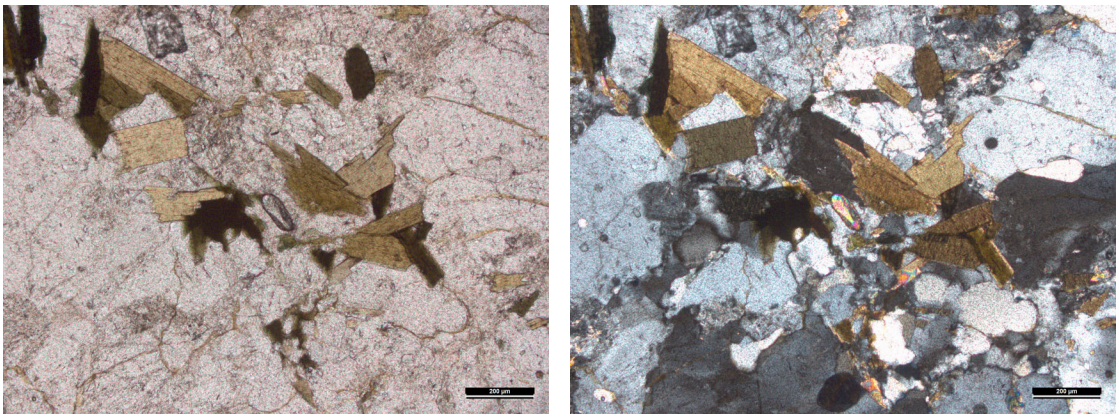

Figure 4.3.: Left: image showing texture of the biotite gneiss with a zircon grain; right: same image (crossed-polarized), notice the sericitic alteration of feldspar; TH1607_2

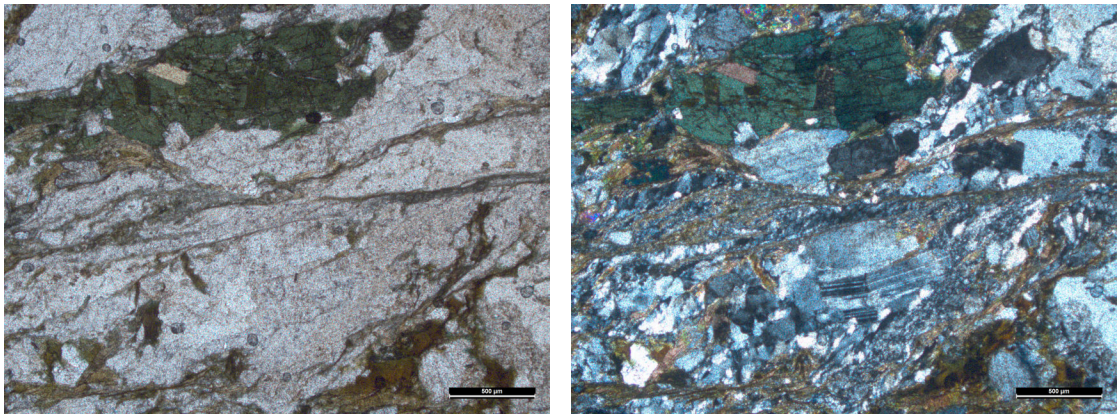

Figure 4.4.: Left: image showing texture of the amphibole-bearing gneiss; right: same image (crossed-polarized), notice the kink-band in the plagioclase twin lamellae; TH1611B_1

4.1.5. Calcsilicate (HNP-G)

Calcsilicate, which can be found intercalated with biotite gneiss have a thin-layered texture (see fig.4.5). Layers are around one centimetre thick and composition varies from centre to rim. While the centre predominantly consists of pyroxene (diopside) and some plagiclase (anorthite), the rim has quartz, plagioclase (albite), K-feldspar and only some hornblende and biotite. Accessories are apatite, zircon and titanite. The latter can reach a few millimetres in size. In contrast to these big euhedral titanites, grainsizes of the other minerals are small (50-500µm) and crystal outlines are rather anhedral. Plagioclase shows undulose extinction, weak sericitic alteration and polysynthetic twin lamellae. These lamellae are sometimes kinked. Quartz also exhibits undulose extinction. Furthermore dynamic recrystallisation of quartz could be observed (bulging, recrystallized subgrains). Where K-feldspar is in contact with plagioclase myrmekites could be observed.

4.1.6. Leucocratic gneiss (L-G)

This gneiss has almost no biotite, instead white mica is common. Mineral composition is K-feldspar (30-40%), quartz (25-30%), plagioclase (20-25%) and white mica (5-10%). Common accessory minerals are apatite, biotite, monazite, zircon and xenotime. It is noticeable that monazites, zircons and xenotimes are rather rare compared to other lithologies. K-feldspars often show Karlsbader twinning and sometimes relictic magmatic zoning. Furthermore quartz and plagioclase myrmekite and quartz and muscovite symplectite could be observerd. Quartz grains have undulose extinction and typically show signs of dynamic recristallisation. Mineral grains only seldom exhibit euhedral outlines and are rather anhedral. Mica grains are rarely oriented and overall the deformation record is less pronounced (see fig.4.6).

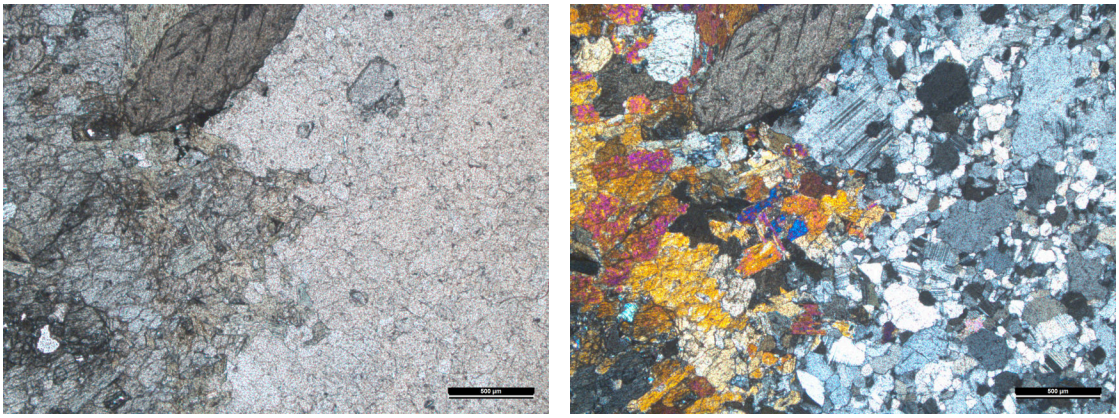

Figure 4.5.: Left: image showing the layering of the calcsilicate; on the left side: pyroxene rich layer; on the right side: plagiclase (anorthite) rich layer; top: big titanite; right: same image (crossed-polarized) showing polysynthetic twins of plagioclase; TH1605_R

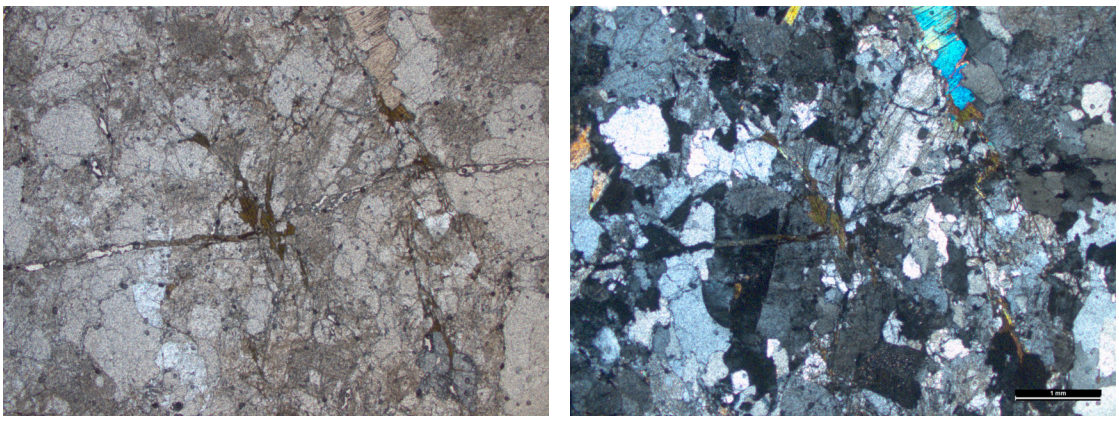

Figure 4.6.: Left: image showing texture of the L-G; right: same image (crossed-polarized); TH1613_1

4.1.7. Mylonite

Two layers could be distinguished. The first is very fine grained and equigranular. It consists out of hornblende (35-40%), plagioclase (30-35%), quartz (15-20%) and K-feldspar (10%). Minor constituents are pyrite, allanite, titanite and zircon. Grains are typical anhedral and around 100µm in size. Brighter elongated patches without amphibole are also common. The second layer consist of plagioclase (40-50%) , hornblende (30-35%), K-feldspar (15%), biotite (5%) and quartz (<5%). Minor constituents are pyrite, allanite, titanite and zircon. It is marked by a porphyroblastic texture with larger mostly euhedral hornblende (500µm) with distinctive pleochroism from green to brown and oblique cleavage planes of around 120°. The matrix contains plagioclase, K-feldspar, biotite and quartz (see fig.4.7).

4.1.8. Conglomerate (not in-situ)

This conglomerate consists of fragments from two similar lithologies in a very fine grained matrix. One lithology consists mainly of hornblende with some elongated plagioclase patches and veins (3mm). Grainsize is homogeneous and around 200-500µm. Accessory minerals are apatite, pyrite, allanite and zircon. The mineral composition of the other lithology is a bit more variable with hornblende (40-50%), plagioclase (35-45%), K-feldspar(5-10%) and quartz (5-10%)(see fig.4.8). Minor constituents are apatite, titanite, magnetite, pyrite and zircon. Grain size is typical around 100-200µm but amphibole commonly reaches up to 500µm. Both lithologies have a granoblastic texture with some well developed 120° triple junctions.
A sample of the matrix could not be obtained, thus it cannot be further described.

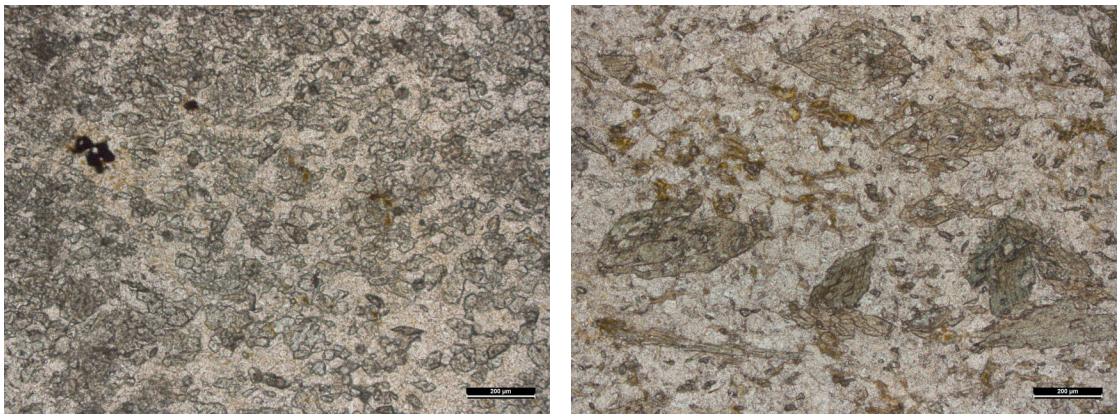

Figure 4.7.: Left: image showing texture of the fine grained mylonite layer whereas the black grains is allanite; right: image showing texture of the porphyric mylonite layer; TH1609A_1

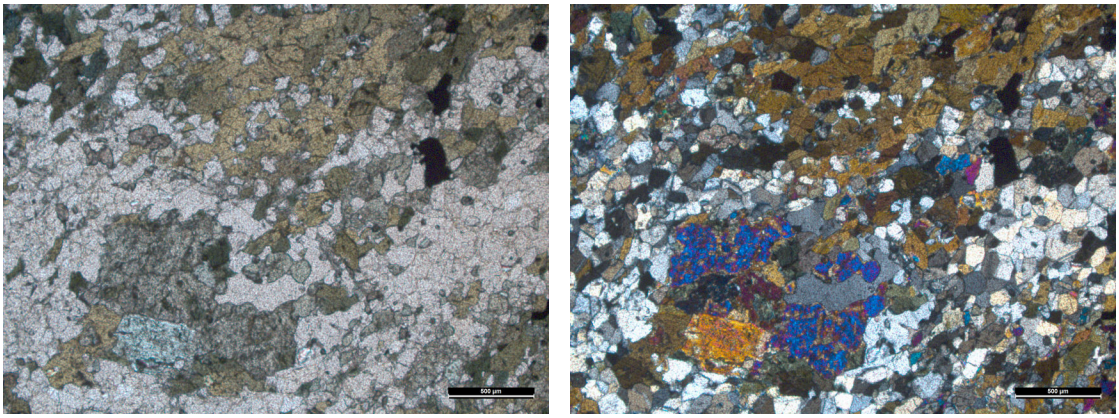

Figure 4.8.: Left: image showing texture of the conglomerate; right: same image (crossed-polarized); TH1604A_R

4.2. Whole rock geochemistry

Five whole-rock samples were analysed for major oxides and trace elements by Acme Analytical Laboratories (Vancouver) Ltd. A list of all data is available in the appendix (see B.1). Sample TH1608 and TH1610 from the LTY-G, sample TH1613 from the L-G and sample TH1611 and TH1612 from the HNP-G, whereas the latter is from the coarse-grained part and the former from the fine-grained. Sampled rocks were classified after O'Conner (1965) and Streckeisen (1974) using normative quartz and feldspar abundances (see fig.4.9). While both use a ternary diagram to classify rock types, O'Conner (1965) uses three feldspars (anorthite, albite, and orthoclase) for his classification and the streckeisen diagram uses the alkali-feldspars and plagioclase-feldspars in general and quartz. In addition rare earth elements (REE) analysis were carried out.

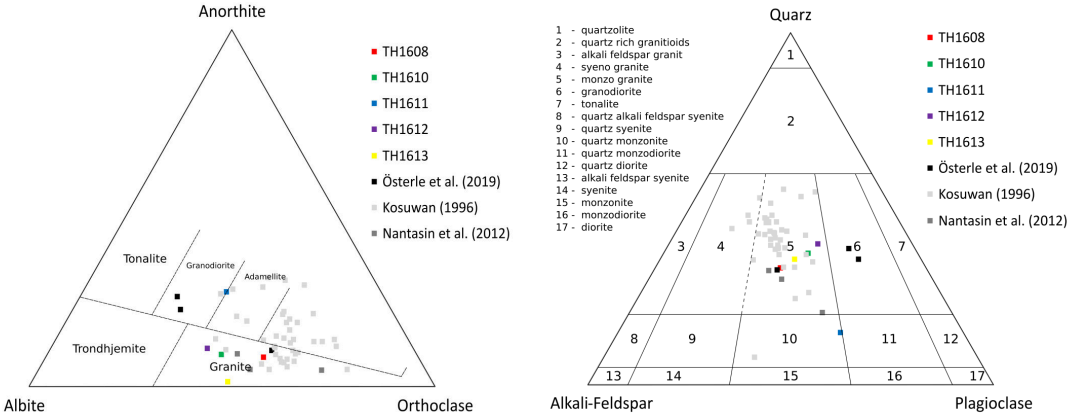

Figure 4.9.: Whole rock classification; left: after O'Conner (1965); right: after Streckeisen (1974); with data from Kosuwan (1996), Österle et al. (2019) and Nantasin et al. (2012)

For the classification after O'Conner (1965) and Streckeisen (1974) an excel spreadsheet called 'ternary-plot' (by Will Vaughan, 2010) was used. In both classifications sample TH1608, TH1610, TH1612 and TH1613 plot in the granitic field. Sample TH1611 shows a distinguished chemical composition and plots between granodiorite and adamellite in O'Conner's diagram and between quartz monzonite and quartz monzodiorite in Streckeisen's diagram (see fig. 4.9). All lithologies, except the amphibole-bearing gneiss (HNP-G, TH1611), show a peraluminous geochemical character within the Al / Ca + Na + K vs Al / Na + K diagram after Shand (1943) (see fig.4.10). In the diagram according to Pearce et al. (1984) the L-G (TH1613) plots in the middle of the volcanic arc & syn-collisional granites field whereas the other samples plot on the edge of this field bordering the within plate granites field.

All REE-pattern show a distinct behaviour, while they are enriched in light-REE, a decrease towards heavy-REE can be observed. The slope in which depletion takes

place is more or less constant. A steepening from Nd to Ga and its flattening out towards Lu is notable. It is also mentionable that all samples show a negative Eu anomaly, whereas it is not as well-marked in TH1611. Futhermore sample TH1613 is depleted in all REE in comparison to the other samples and its slope is flatter and not that consistent (see fig. 4.11)

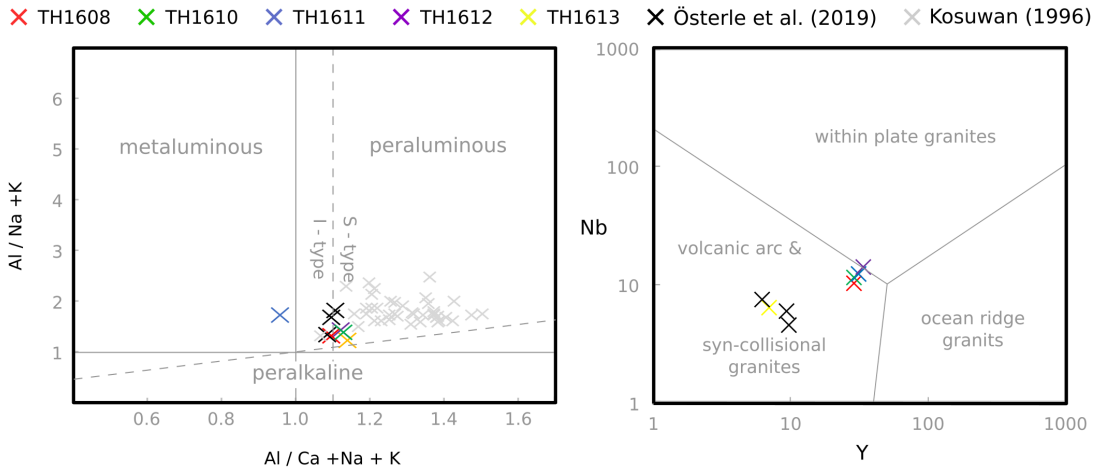

Figure 4.10.: Al / Ca + K + Na vs Al / Na + K diagram (after Shand 1943) and Y vs Nb diagram (after Pearce et al. 1984); with data from Kosuwan (1996) and Österle et al. (2019)

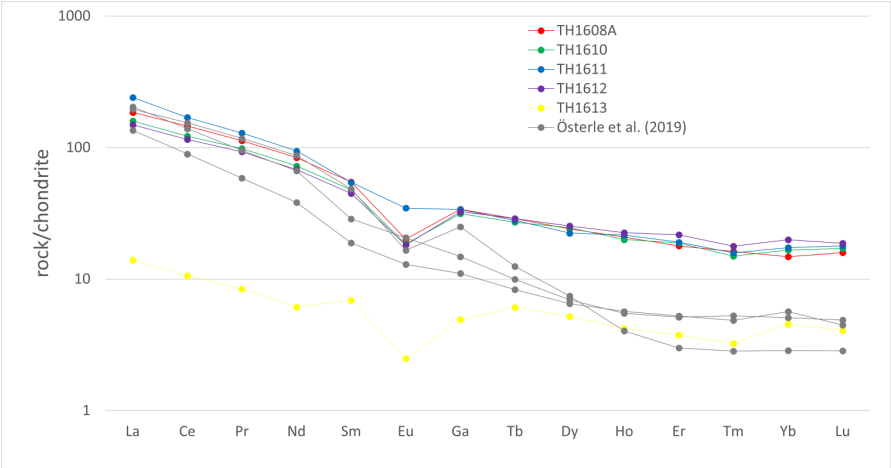

Figure 4.11.: REE-pattern whole rock; with data from Österle et al. (2019)

4.3. Mineral geochemistry

Mineral chemistry of main phases and monazites were made by EMPA using a Cameca SXFive instrument available at the University of Vienna, Department of Lithospheric Research. All data can be contemplated in the appendix B.2.

4.3.1. Feldspar

Microprobe data show that feldspars split into two major groups, orthoclase and plagioclase (see fig. 4.12). Samples TH1608A1/A2 and TH1612C1/C2 show comparable clusters in the orthoclase and plagioclase field. The measured plagioclase points of these samples plot in the oligoclase domain, with a few deviating data-points. Most of these aberrant points are relatively near alkali-feldspars. Differences between plagioclase in the matrix and those in big alkali-Feldspars could not be observed.
Its noteworthy that sample TH1611 shows a distinct feldspar chemistry in comparison to the other samples. Plagioclase data points are enriched in anorthite-component relative to the other samples and plots in the andesine field. Also alkali-feldspars are enriched in K_2O and therefore show relative pure orthoclase grains. The few points of sample TH1608A2 that show a higher orthoclase-component are very small grains of alkali-feldspars which are located adjacent to or within biotite and hence may be contaminated.

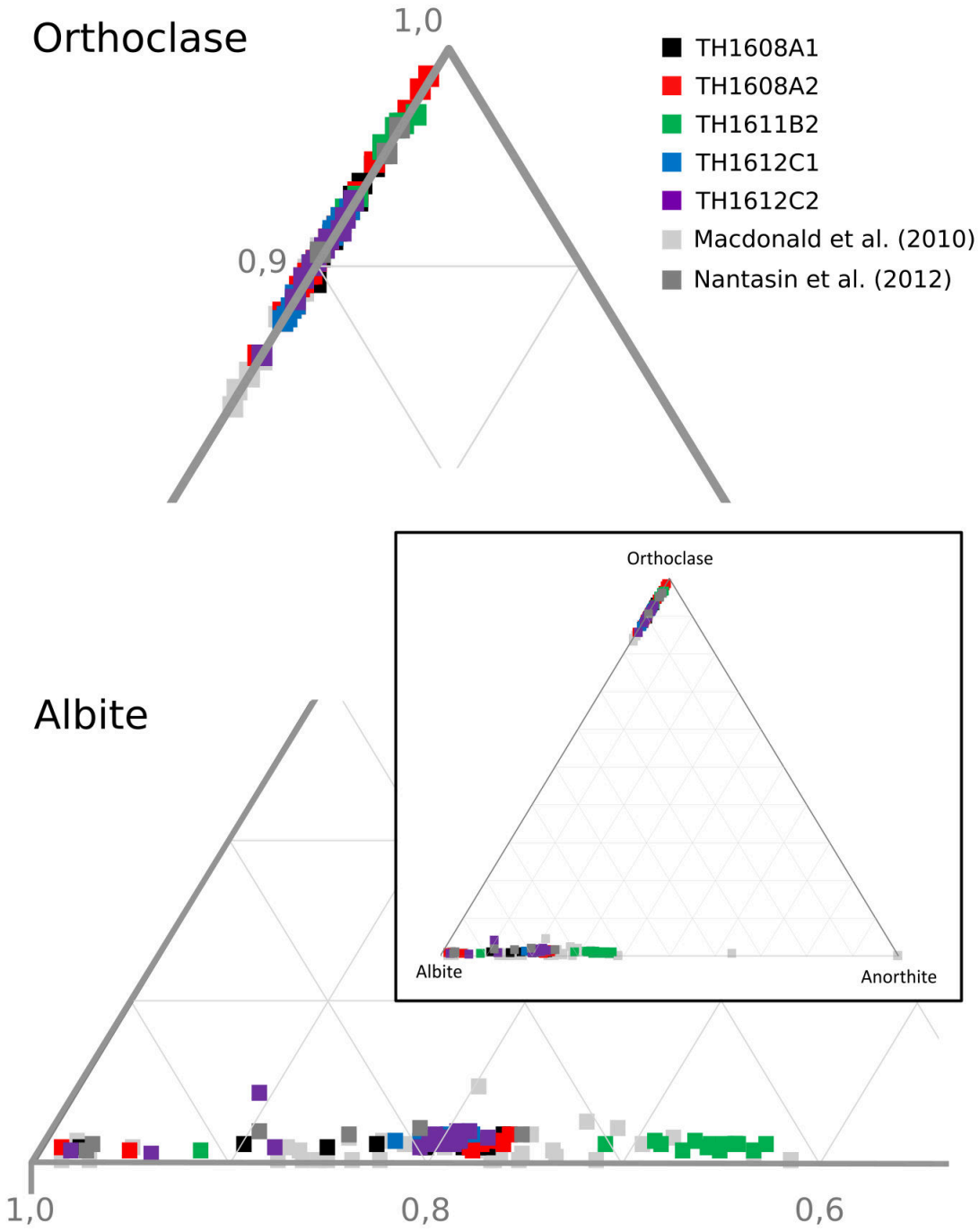

Figure 4.12.: Composition of feldspars showing two clusters in the plagioclase field and a more or less wider range in alkali-feldspar, with data from Nantasin et al. (2012) and Macdonald et al. (2010)

4.3.2. Biotite

Biotite chemistry shows, like the feldspars, two distinct clusters. Sample TH1611B2 shows a distinctive chemical signature from the other samples with lower Al/(Al+Mg) and Fe/(Fe+Mg) values. With a few exceptions, all the remaining samples plot in one seperate cluster (see fig. 4.13). The main geochemical differences between these clusters lies in there total Al and Mg contents. In both clusters the total Al is relatively low. In sample TH1611C it ranges from 1.39 to 1.48 apfu (mean: 1.45 apfu), whereas in the other samples it ranges from 1.56 to 1.80 apfu (mean: 1.66 apfu). Total Mg contents are significantly higher in sample TH1611C ranging from 1.07 to 1.20 apfu (mean: 1.12 apfu), whereas the other sample show a range of 0.62 to 0.89 apfu (mean: 0.71 apfu). Different generations of biotite within a sample could not be observed.

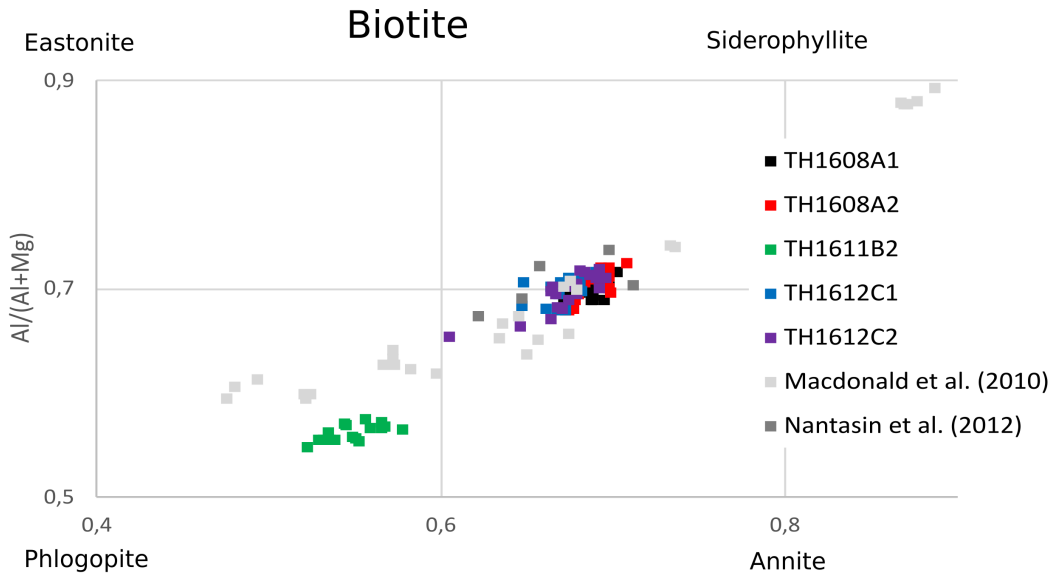

Figure 4.13.: Composition biotite; with data from Macdonald et al. (2010) and Nantasin et al. (2012)

4.3.3. White mica

White mica could only be measured in sample TH1608A1/A2 and TH1612C2. Whereas in TH1608A1 only two grains with a rather big spread could be observed, samples TH1608A2 and TH1612C2 show seperate clusters. TH1612C2 shows lower Mg+Fe and Si numbers in comparison to TH1608A2. Total Mg and Fe show a similar order of magnitute with slightly more total Fe. Whereas total Mg ranges in sample TH1612C2 from 0.071 to 0.083 apfu (mean: 0.077 apfu) and total Fe from 0.087 to 0.11 apfu (mean: 0.097). In sample TH1608A2 total Mg ranges from 0.105 to 0.150 apfu (mean: 0.124 apfu) and total Fe from 0.121 to 0.156 apfu (mean: 0.136 apfu). With one exception, the measured point show a linear Mg+Fe to Si ratio (see fig. 4.14).

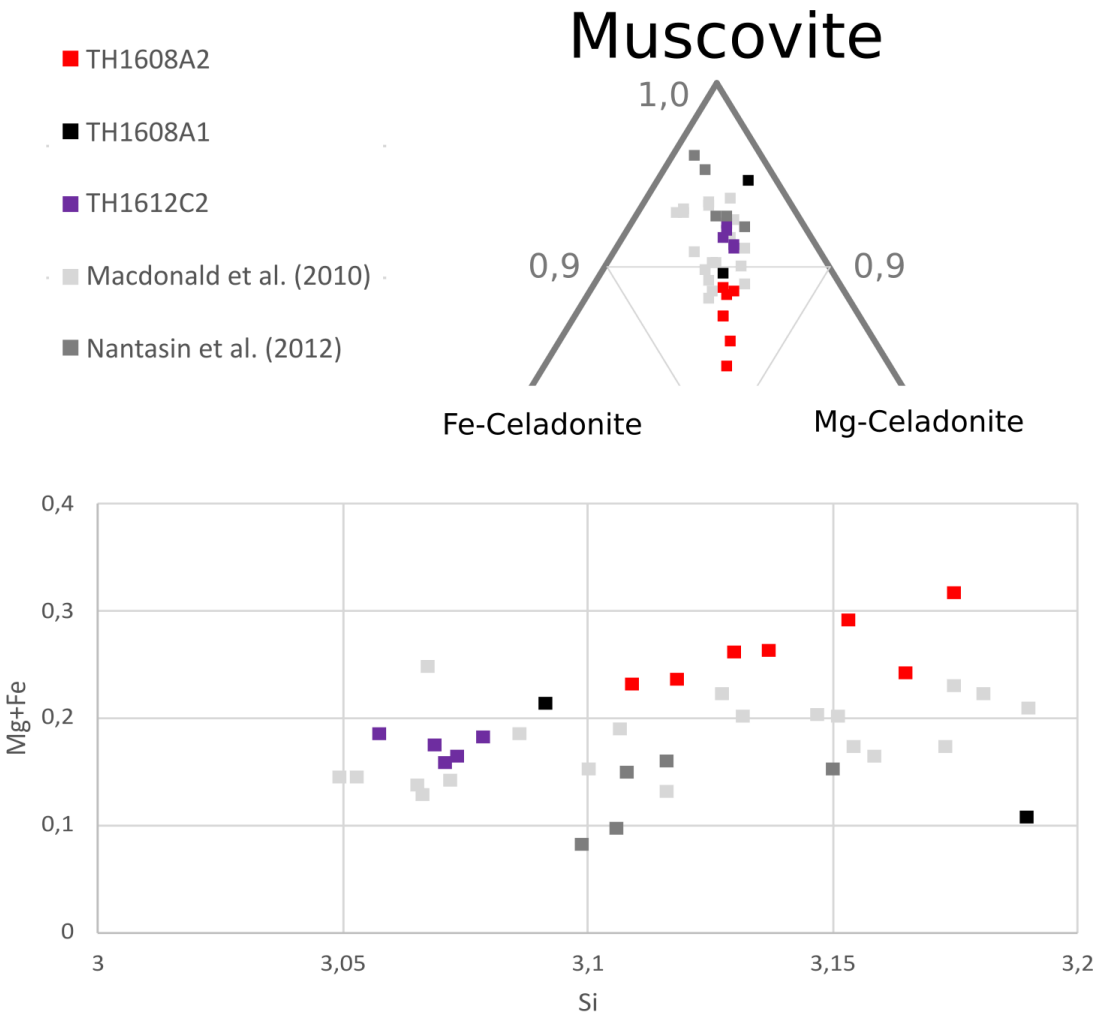

Figure 4.14.: Composition muscovite; with data from Macdonald et al. (2010) and Nantasin et al. (2012)

4.3.4. Amphibole

TH1611B2 was the only analysed sample which contains amphiboles. Calculations where done with a excel spreadsheet called ACES_1 by Locock (2014) who follows the recommendations from the IMA 2012 published by Hawthorne et al. (2012). All measured amphiboles are hastingsites (see fig.4.15). This means they belong to the calcium amphibole subgroup (^{B} (Ca + $\sum M^{2+}$)/$\sum$B $\geq$ 0.75, ^{B}Ca/$\sum$B $\geq$ B$\sum M^{2+}$/$\sum$B) which is part of the w(OH, F, Cl)-dominant amphibole group (W((OH)+F+Cl) >1 apfu). Hastingsite itself is defined by 0.5 <^{A}(Na+K+2Ca) <1.5 where Na or K is dominant,. The C position is occupied by Mg or Fe^{2+} as dominant divalent ions and 0.5 <^{C}(Al+Fe^{3+}+Cr+2Ti) < 1.5 where Fe^{3+} is dominant.

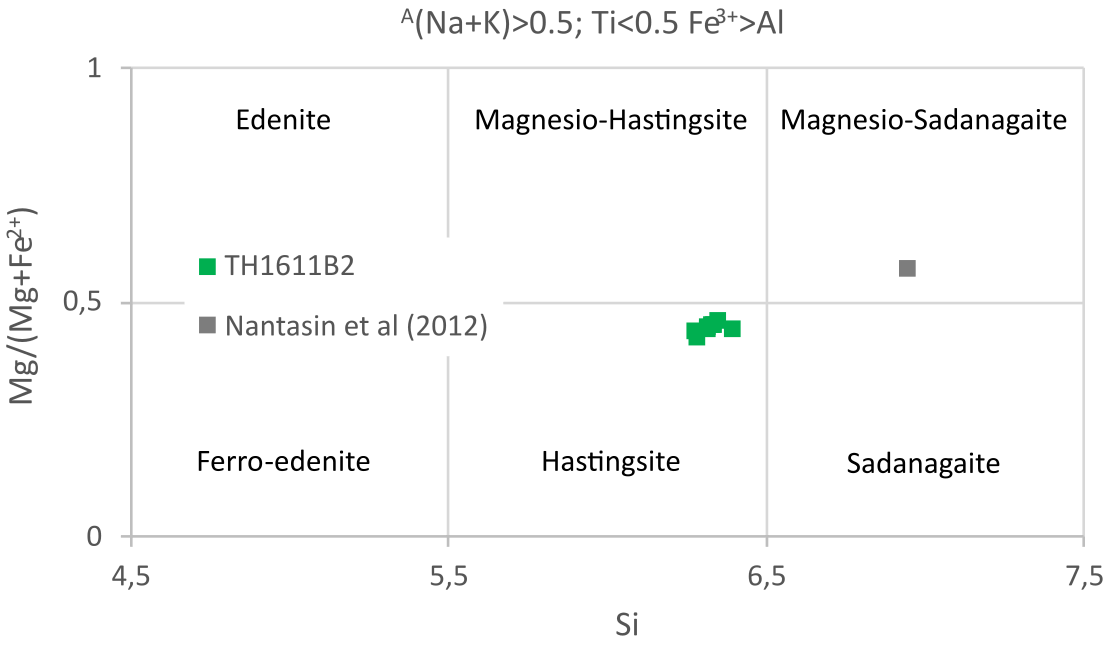

Figure 4.15.: Composition of all measured amphiboles from sample TH1611B2 plot in the Hastingsite field; with data from Nantasin et al. (2012) (whereas Fe^{3+} < Al in their data)

4.3.5. Monazite

Monazite measurements were conducted on thinsections from the HNP-G (TH1612C2) and the LTY-G (TH1608A1/A2). All analysed monazites plot in a small cluster within the Ce-La-Nd ternary diagram (see fig.4.16). A core-rim increase in HREE for monazites in metapelites (Heinrich et al. 1997) is only visible in the HNP-G and not in the LTY-G. Futhermore it is worth mentioning that the rim zonation in HNP-G has a significantly higher uranium-concentration. Moreover in the LTY-G huttonite substitution is clearly dominant and in the HNP-G cheralite substitution is also relevant (see fig.4.17).

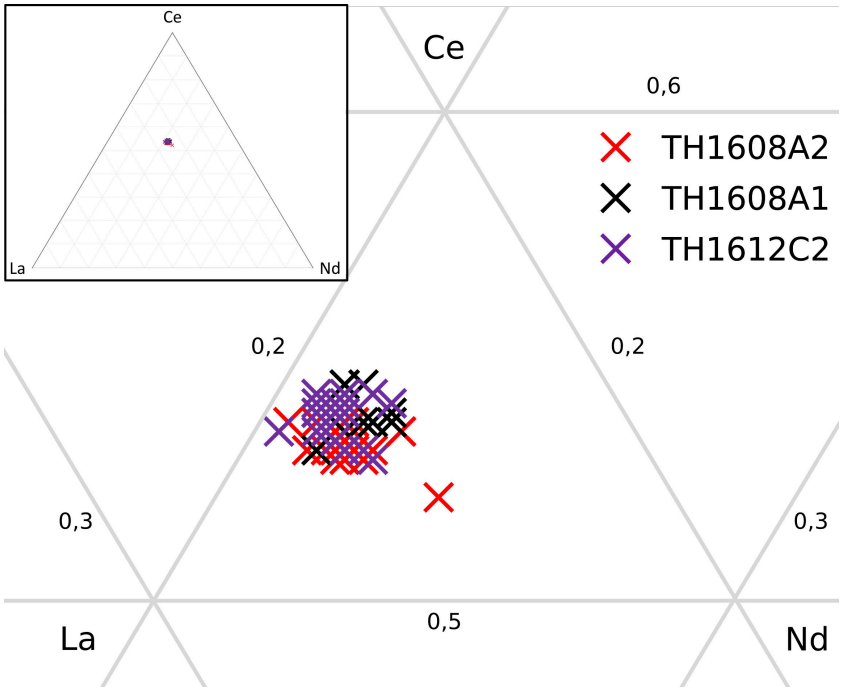

Figure 4.16.: Ternary diagram of Ce-La-Nd (after Spear and Pyle 2002) for investigated monazite from sample TH1612C and TH1608A

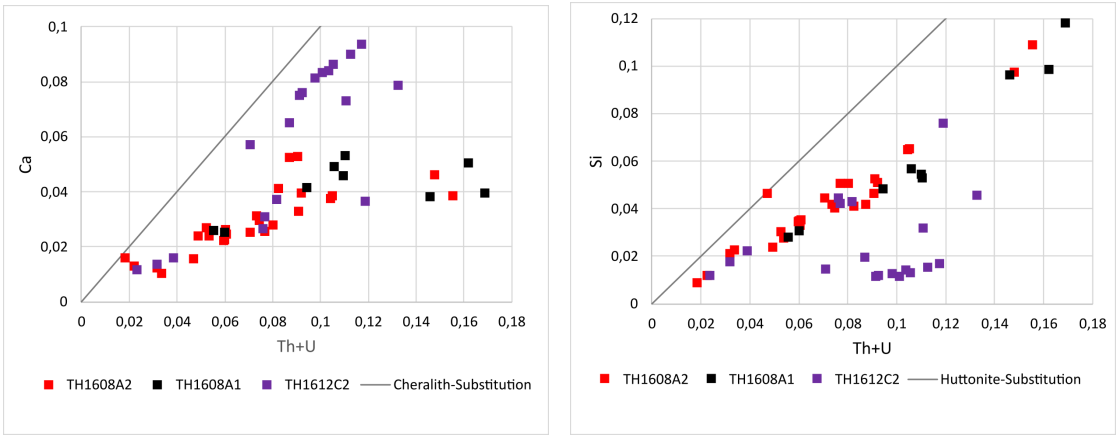

Figure 4.17.: Diagrams showing the cheralite (left) resp. huttonite (right) substitution in monazite (after Spear and Pyle 2002)

4.3.6. Other minerals

In sample TH1611B2 from the amphibole-bearing gneiss five measurements of clinozoisite could be obtained. These clinozoisites have almost no Mn^{3+} and Cr^{3+} but some Fe^{3+} component (see fig.4.18). Also few chlorites could be measured in sample TH1611B2 and in sample TH1608A1/A2 (see fig.4.18). Chlorites in TH1611B2 are plotting in two clusters, one within the ripidolite field and the other on the border of ripidolite, pycnochlorite and brunsvigite. The four analysed chlorites from sample TH1608A1/A2 are more spread and two plot in the diabantite field. The wide spread and strange composition may be due to close contact with biotite and K-feldspar and therefore contamination. Furthermore two titanites and one calcite were measured, but not further analysed because of minor abundance.

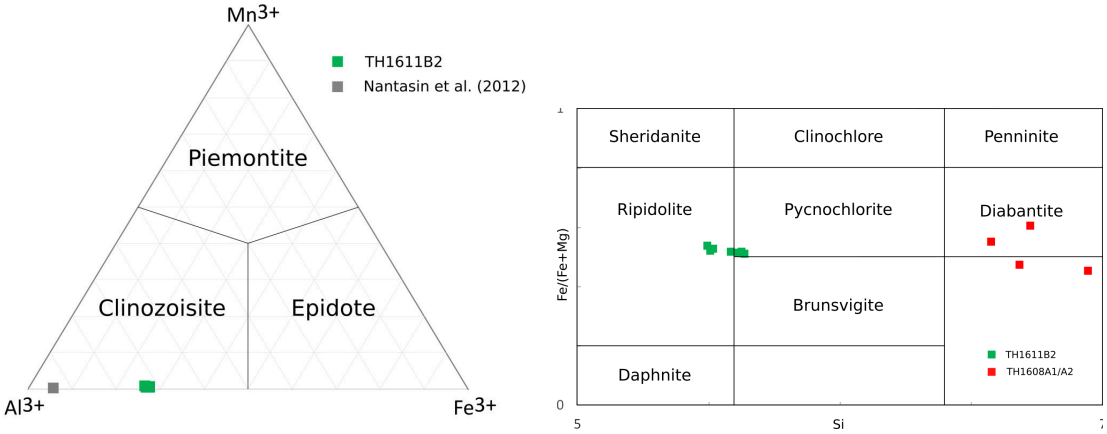

Figure 4.18.: Left: Ternary diagram of Mn-Al-Fe for analysed clinozoisite from sample TH1611B2; right: Fe/(Fe+Mg) to Si diagram for analysed chlorites from sample TH1611B2 and TH1608A1/A2

5. Thermobarometry

5.1. Method

5.1.1. Al-in-hornblende barometry and hornblende-plagioclase thermometry

The original idea of Al-in-hornblende barometry is based on the assumption that the total aluminium content (Al^{tot}) of magmatic hornblende is in a linear relationship to crystallisation pressure of intrusion. This correlation can be applied to calcalkalic rocks with a mineral assemblage of plagioclase (andesine - oligoclase), K-feldspar, quartz, hornblende, biotite, titanite, magnetite or ilmenite (and epidote), which buffer the system (Hammarstrom and Zen 1986). A possible buffer-reaction is mainly ascribed to a tschermak-exchange and would be:

$$phlogopite + 2quartz + 2anorthite = tremolite + orthoclase + 2\vec{tk} \tag{5.1}$$

Schmidt (1992) experimentally calibrated this geobarometer under water-saturated conditions at pressures of 2.5-13 kbar and temperatures of 700-655°C and proposed a formula for calculating pressures:

$$P(\pm 0.6kbar) = -3.01 + 4.76Al^{tot}_{hbl} \qquad r^2 = 0.99 \tag{5.2}$$

Another experimental calibration was done by Johnson and Rutherford (1989) which was accomplished at higher temperatures, stabilizing the required buffer assemblage by the use of mixed H_2O-CO_2 fluids. The two calibration are consistent, but comparison shows the importance of fluid composition, which affects solidus temperature and therefore the hornblende equilibrium in the buffering assemblage.
Anderson and Smith (1995) doubted the assumption that many or most granitic plutons where emplaced on or near a H_2O-saturated solidus and derived a formula based on the work of Johnson and Rutherford (1989) and Schmidt (1992) which is also temperature dependent:

$$P(kbar) = 4.76Al - 3.01 - [(T(°C) - 675)/85]x[0.530Al + 0.005294(T(°C) - 675)] \tag{5.3}$$

For the hornblende-plagioclase thermometry formula B from Holland and Blundy (1994) was used which is based on the ideal equilibrium of edenite + albite = richterite + anorthite but takes non-ideal mixing of amphibol and plagioclase into account:

$$T_B(\pm 35 - 40K) = \tag{5.4}$$

$$\frac{78.44 + Y_{ab-an} - 33.6X_{Na}^{M4} - (66.8 - 2.29P(kbar)) \cdot X_{Al}^{M2} + 78.5X_{Al}^{T1} + 9.4X_{Na}^{A}}{0.0721 - R \cdot ln\frac{27 \cdot X_{Na}^{M4} \cdot X_{Si}^{T1} \cdot X_{an}^{plag}}{64 \cdot X_{Ca}^{M4} \cdot X_{Al}^{T1} \cdot X_{ab}^{plag}}}$$

$$\text{where the } Y_{ab-an} \text{ term is given by: } X_{ab} > 0.5 \text{ then } Y_{ab-an} = 3.0kJ$$
$$\text{Otherwise } Y_{ab-an} = 12.0(2X_{ab} - 1) + 3.0kJ$$

Calculations were performed with an excel spreadsheet called 'adaptiertes Sheet von Hol+Bl' which was original prepared by Lawford Anderson, University of Southern California. This spreadsheet uses wt% oxides from amphiboles to calculate amphibole mineral composition after Holland and Blundy (1994). Furthermore the X_{ab} and X_{an} of plagioclase must be given. It calculates by using iteration of the geothermometer from Holland and Blundy (1994) (see Eq.5.4) and the geobarometer from Anderson and Smith (1995) (see Eq.5.3). Initially the pressure for iterations is calculated with the formula from Schmidt (1992) (see Eq.5.2).

5.1.2. Monazite–xenotime miscibility gap thermometry

Monazite coexisting with xenotime has a potential use as geothermometer. This is due to the fact that incorporation of HREE and particularly of yttrium into monazite is strongly temperature and only slightly pressure-dependent. Heinrich et al. (1997) showed this empirically on the basis of a suite of seven metapelites from the Variscan fold belt in NE Bavaria. Gratz and Heinrich (1997) then experimentally calibrated this thermometer within the binary system $CePO_4$-YPO_4 at 300-1000°C and pressures of 2, 5, 10, and 15 kbar:

$$X_Y^{monazite} = \frac{(1.459 + 0.0852P(kbar))e^{0.002274T(°C)}}{100} \tag{5.5}$$

This simple assumption that the binary system $CePO_4$-YPO_4 suffices as geothermobarometer leaves out any effect of other components (Ca, U, Si, and Th) especially at higher temperatures (Spear and Pyle 2002). Seydoux-Guillaume et al. (2002) examined the effect of $ThSiO_4$ substitution into monazite/xenotim and showed that the incorporation of Th narrows the miscibility gab. Calculations where carried out with the formula form Gratz and Heinrich (1997) (see Eq.5.5), whereas pressure from the Al-in-hornblende barometry were used. Furthermore Th correction after Seydoux-Guillaume et al. (2002) were calculated.

5.2. Results

For the hornblende-plagioclase geothermobarometer a set of only 8 measurements from sample TH1611B2 was used. Even though it is a small number of data, it should suffice for a first approximation of pressure, which is required for the monazite-xenotim thermometry. Temperatures range from 711-732°C (±35-40°C) by pressures at 5.7-6.7kbar (±0.6kbar) (see Appendix C tab.C.1).

Temperatures for monazite–xenotime thermometry are split into sample TH1612C2 and TH1608A1/A2. Both have a range from roughly 400-770°C with one exception. Whereas TH1612C2 shows two distinct plateaus, TH1608A1/A2 indicates only one with up- and downfalling ends (see fig.5.1). Another interesting approach is to arrange temperatures of single monazites from core to rim (see fig.5.2). In doing so it becomes clear that sample TH1608A1/A2 shows a retrograde zoning pattern, whereas TH1612C2 shows a prograde. Furthermore sample TH1612C2 shows low temperatures (∼550°C) in cores and high temperatures (∼740°C) at the rims, which correlates well with the temperatures plateaus from figure 5.1. In sample TH1608A1/A2 temperatures are generally lower at rims and higher at cores, but a distinctive bimodal distribution as in sample TH1612C2 is not visible.

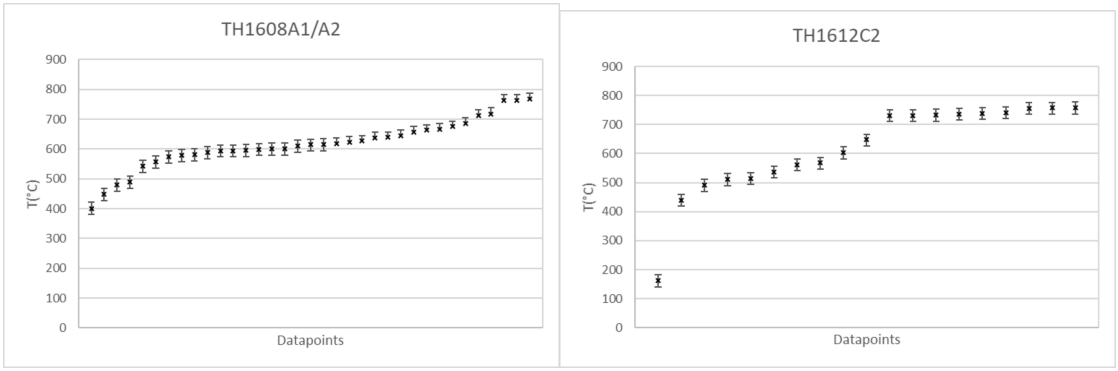

Figure 5.1.: Temperatures for monazites sorted in ascending order

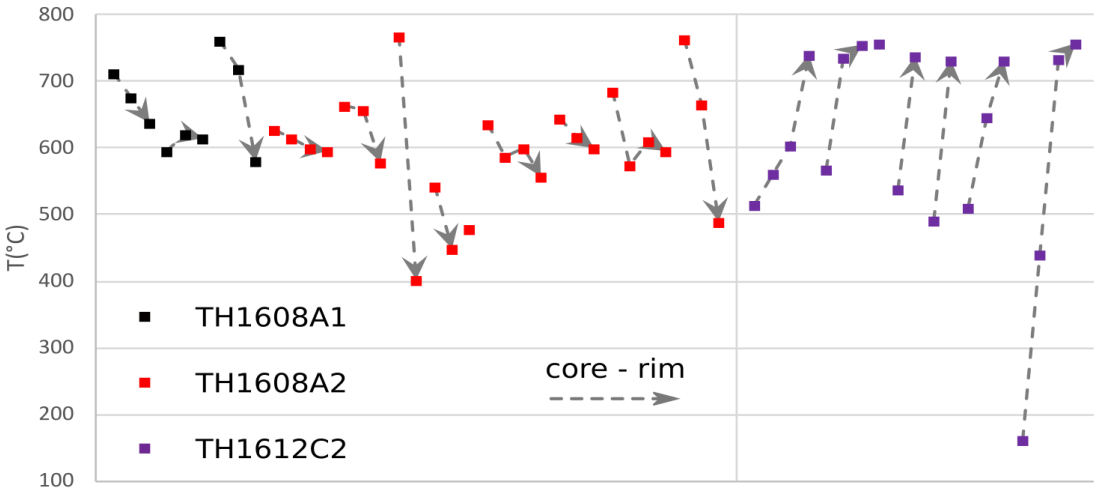

Figure 5.2.: Temperatures for monazites sorted after core-rim zonation; TH1608 shows a retrograde zoning pattern whereas TH1612 shows a prograde

6. Geochronology

6.1. Methods

6.1.1. Monazite-EMPA

Measurements were done as in situ single spot analyses on thin section from LTY-G (TH1608A2) and coarse-grained HNP-G (TH1612C1) using a Cameca SX 100 electron microprobe analyser (EMPA) at the State Geological Institute in Bratislava, Slovak Republic. An improved approach to monazite dating by electron microprobe that includes a 'monazite age reference correction' (MARC) was applied. The full standard operating procedure can be found in Konečný et al. (2018).

6.1.2. Zircon-SIMS

Zircon separation was done on three whole rock samples (TH1608, TH1611 TH1612), each 10-15 kg, using conventional methods (crushing, sieving, Wilfley table, magnetic and heavy liquid separation and hand picking). Zircons were mounted in epoxy and polished for cathodoluminescence (CS) imaging.

SIMS measurements of U, Th and Pb isotopes were carried at the same time, location and with the same procedure as in Burda et al. (2020, p.141-142):

> In situ SIMS measurements of U, Th and Pb isotopes were conducted using a Cameca IMS-1280 HR SIMS at the Institute of Geology and Geophysics, Chinese Academy of Sciences (Beijing, China) during two sessions. A hybrid dynamic multi-collector U-Pb dating technique was used and taking advantage of both the static multi-collector mode and peak-hopping mono-collector mode and using oxygen flooding. The instrument description and analytical procedure can be found in Liu et al. (2015), and only a brief summary is given here. Before data acquisition, each spot was pre-sputtered on an area ~30 × 25 μm in size for 120s to remove any surface contamination and to enhance the yield of secondary ions. Due to spatial restrictions in the internal zonation patterns of the zircons, the primary O_2^- ion beam spot was chosen to be ~7 × 5 μm in size. Positive secondary ions were extracted with a 10 kV potential. In the secondary ion beam optics, a 60 eV energy window was used, together with a mass resolution of ca. 5400 (at 10% peak height), to separate Pb^+ peaks from isobaric interferences. Each measurement consisted of 7 mass cycles. The total analytical time was ~14

min per spot.
Pb/U calibration was performed relative to Temora-2 (ID-TIMS $^{206}Pb/^{238}U$ age = 416.78 ± 0.33 Ma; Black et al. 2004). U and Th concentrations were calibrated against reference zircon 91500 (Th = 29 ppm, and U=81 ppm; Wiedenbeck et al. 1995). A long-term uncertainty of 1.5% (1sd) for $^{206}Pb/^{238}U$ measurements of the reference zircons was propagated to the unknowns, despite that the measured $^{206}Pb/^{238}U$ uncertainty in a specific session generally was ±1% (1sd; Liu et al. 2015). Thus, the reported analytical uncertainty of the U/Pb ratio includes the internal uncertainties from data acquisition and the propagation of the external uncertainty of the U/Pb fractionation calibration. An average Pb of the present-day crustal composition ($^{206}Pb/^{204}Pb$ = 18.703, $^{207}Pb/^{204}Pb$ = 15.629; Stacey and Kramers 1975) was used for the common Pb correction assuming that it is largely due to surface contamination introduced during sample preparation. The uncertainty propagation from the common Pb correction to the $^{207}Pb/^{206}Pb$ age measurement follows those described by Li et al. (2009). Corrections are sufficiently small to be insensitive to the choice of common Pb composition.

For concordia age calculation the program IsoplotR online from Pieter Vermeesch was used (Vermeesch 2018).

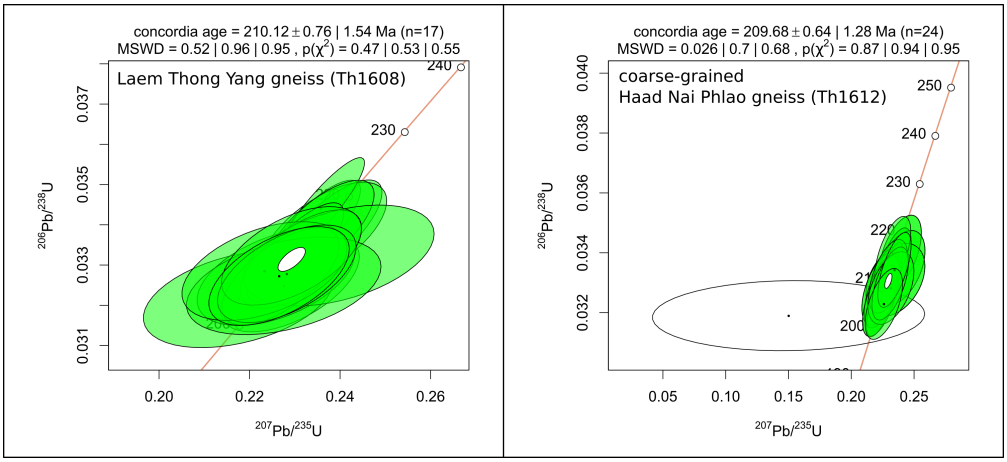

Figure 6.1.: Wetherill concordia plots of zircon $^{206}Pb/^{238}U$ analyses

6.2. Results

6.2.1. Laem Thong Yang gneiss (TH1608)

Zircons from the LTY-G are commonly euhedral and exhibit long prismatic habits (length ∼100-600µm in max. dimension) with aspect ratios around 3:1 to 5:1. Cathodoluminescence images reveal well marked zonation and oftentimes a bright zoned core surrounded by a dark layer, which is in turn surrounded by medium bright zonation (see fig.6.4). Th/U values are rather low and ranging from 0.002 to 0.02 with a mean of 0.012 ± 0.014 (2s). Zircon SIMS ages (n=18) yield Indosinian $^{206}Pb/^{238}U$ dates ranging from 218.1 ± 6.4 Ma to 204.0 ± 6.2 Ma with one exception, a core which gives a date at 323.9 ± 5.3 Ma. U-Pb analyses normally show discordance, whereas by ∼78% is the level of discordance ≤ 20%. Discordant ages are both normally and reversely discordant. The weighted mean of the Indosinian ages is 210.3 ± 6.3 Ma (MSWD = 1.52, n=17)(see fig.6.2). Concordia age calculations yield similar ages 210.1 ± 0.8 Ma (see fig.6.1).

Monazites are rather anhedral with more or less equant habits with grainsizes from ∼20µm up to ∼150µm. Zonation is recognizable but mostly not very well developed and shows core rim like or sometimes more patchy architecture (see fig.6.5). Th/U ratio range from 12.5 to 27.5 with a mean of 21.7 ± 8.0 (2s). Monazite U-Th-Pb analysis are distributed bimodal with mostly Cretaceous ages but also some Indosinian data points. The Cretaceous ages (n=15) spread from 66.9 ± 14.5 Ma to 94.8 ± 24.9 Ma with a mean of 81.2 ± 15.2 Ma. Two younger ages and one older were neglected due to low Th content. The Indosinian ages (n=3) have a range from 212.7 ± 12.1 Ma to 215.8 ± 17.3 Ma and a weighted average of 214.4 ± 16.1 Ma (MSWD = 0.055) and therefore overlap with the measured zircon ages from this sample (see fig.6.2). CHIME ages are shown in fig.6.3 and yield an Indosinian age of 209.1 ± 18.1 Ma and a Cretaceous age of 79.1 ± 6.9 Ma.

6.2.2. Coarse-grained Haad Nai Phlao gneiss (TH1612)

Zircons usually range in length between 100-300µm with commonly euhedral shape. They show aspect ratios between 1:1 and 4:1, whereas long prismatic shape is not as common as in the LTY-G. Zonation is well established, complex and often shows a bright zoned core with a dark rim and a medium bright outer zonation (see fig.6.4). Th/U values are also low with a range from 0.002-0.018 with a mean of 0.008 ± 0.010 (2s). $^{206}Pb/^{238}U$ dates of these zircons (n=18) yield dominantly Indosinian ages ranging from 199.2 ± 6.2 Ma to 215.5 ± 6.4 Ma and one very old age 1011.1 ± 28.3 Ma. The mean value of the Indosinian ages is 209.4 ± 6.2 (see fig.6.2). Most of the ages show some degree of discordance whereas by ∼83% is the level of discordance ≤ 20%. Discordant ages are more or less equally distributed between normally and reversely discordant. A Wetherill concordia diagram is shown in fig.6.1 and yields a concordia age of 209.7 ± 0.6 Ma.

Monazite crystals are approximately 20-150µm in size and show anhedral habit with

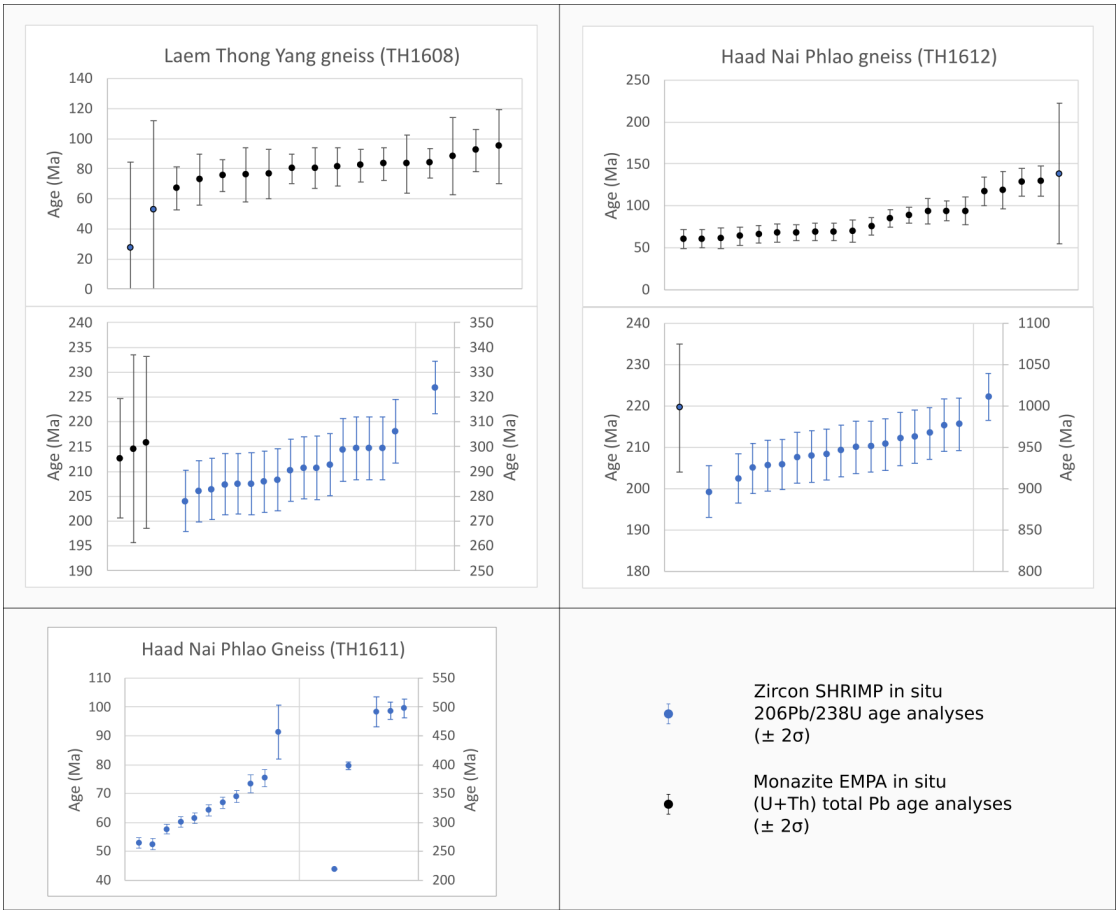

Figure 6.2.: Rank-order plots of zircon 206Pb/238U ages and monazite (U-Th) total Pb ages of this study

an aspect ratio of mostly 1:1 up to 1:2 in some cases. Core-rim zonation is recognizable but not very distinct (see fig.6.5). Th/U values vary from 6.0 - 50.2 with an average of 15.7 ± 22.5 (2s). U-Th-Pb analyses of monazite yield a wide range of ages from early Eocene (60.6 ± 11.1 Ma) till early Cretaceous (129.7 ± 17.7 Ma) and one Indosinian age (219.5 ± 15.4 Ma) (see fig.6.2). A CHIME age was created from selected analyses yielding an age of 94.4 ± 8.2 Ma (see fig.6.3).

6.2.3. Fine-grained Haad Nai Phlao gneiss (TH1611)

While this sample does contain zircons, no monazites could be found. Zircons are also rather small compared to the other samples, ranging in length from ~50-200µm with an aspect ratio of 1:1 or 1:2. Internal structures of these zircons varies. Sometimes a patchy core with a zoned rim could be observed. Smaller equant zircons tend to be rather patchy while prismatic zircons show more (strict) zonation (see fig.6.4).

Th/U values are low varying from 0.0004 to 0.046 with a average of 0.022 ± 0.031 (2s). $^{206}Pb/^{238}U$ ages (n=16) are wide spread and range from 497.3 ± 7.8 Ma to 52.5 ± 1.0 Ma. The degree of discordance from these analyses is rather high with only ~35% of the data points showing a discordance $\leq$ 20%. One cluster of three late Cambrian ages yield a weighted average age of 493.9 ± 18.7 Ma. Another more wide spread cluster (n=10) yields a mean age of 63.3 ± 2.1 Ma (see fig.6.2).

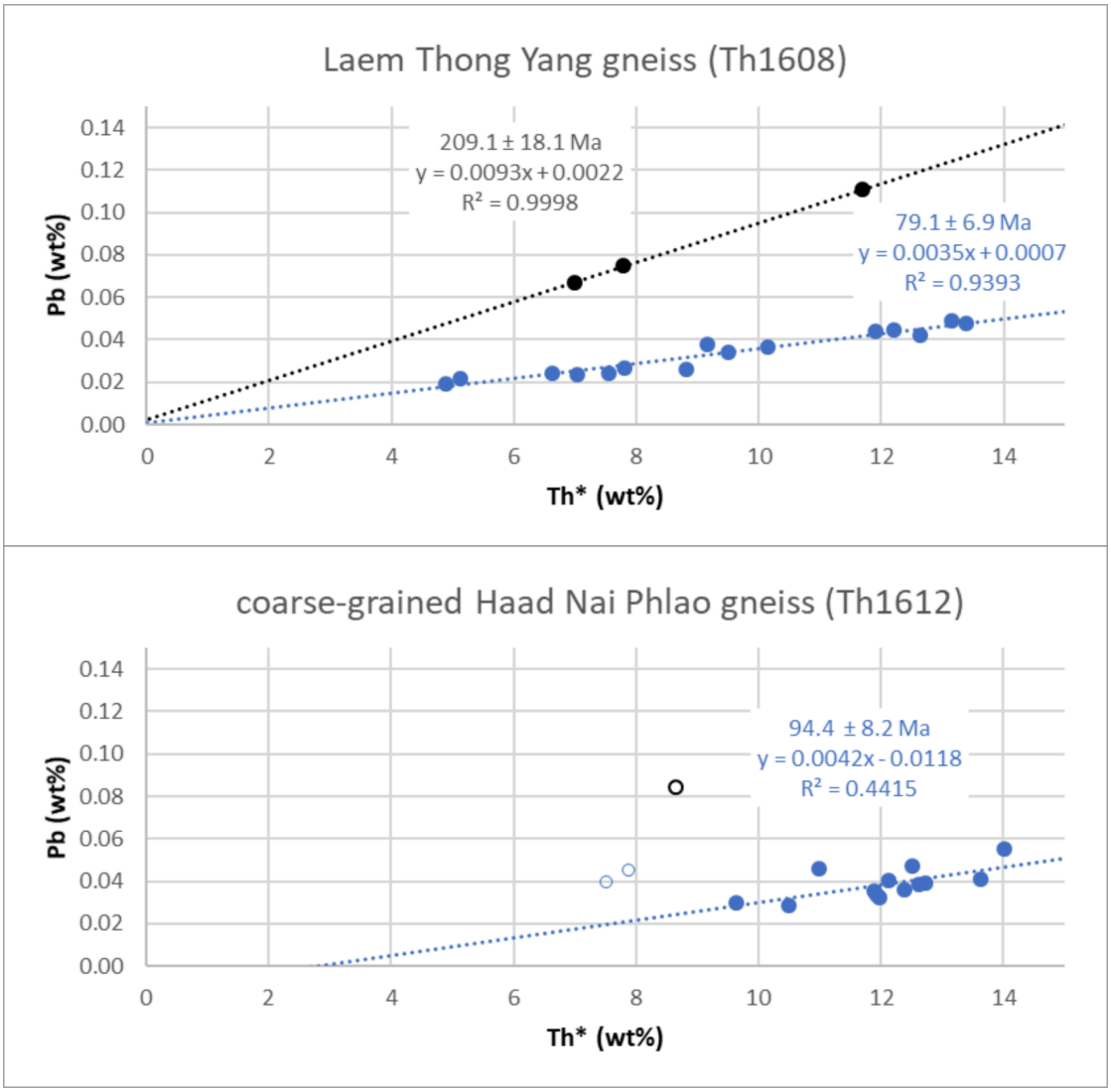

Figure 6.3.: Pb-Th* diagram showing the result of CHIME monazite dating

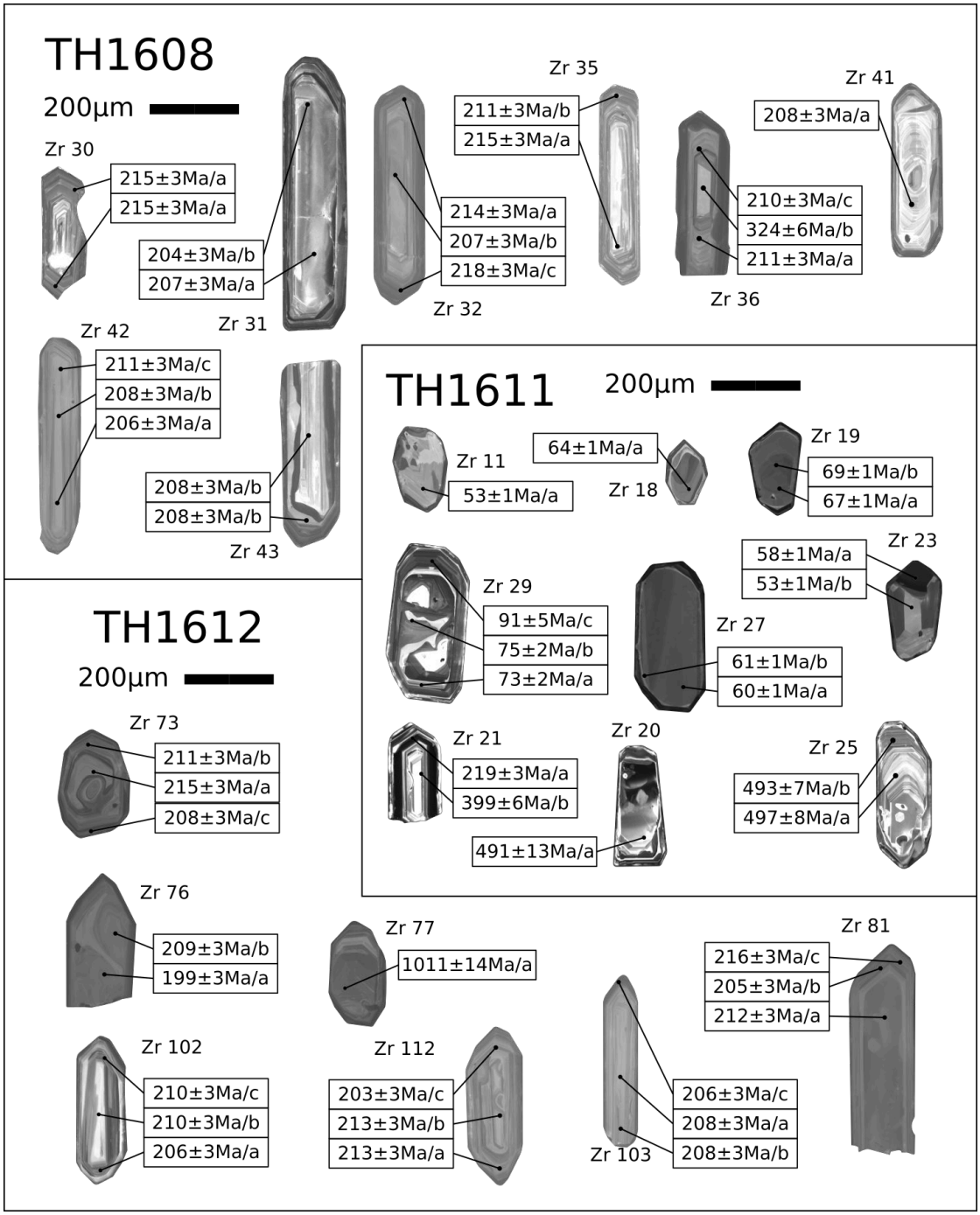

Figure 6.4.: Cathodoluminescence images of zircon from this study with $^{206}Pb/^{238}U$ dates (±1 σ)

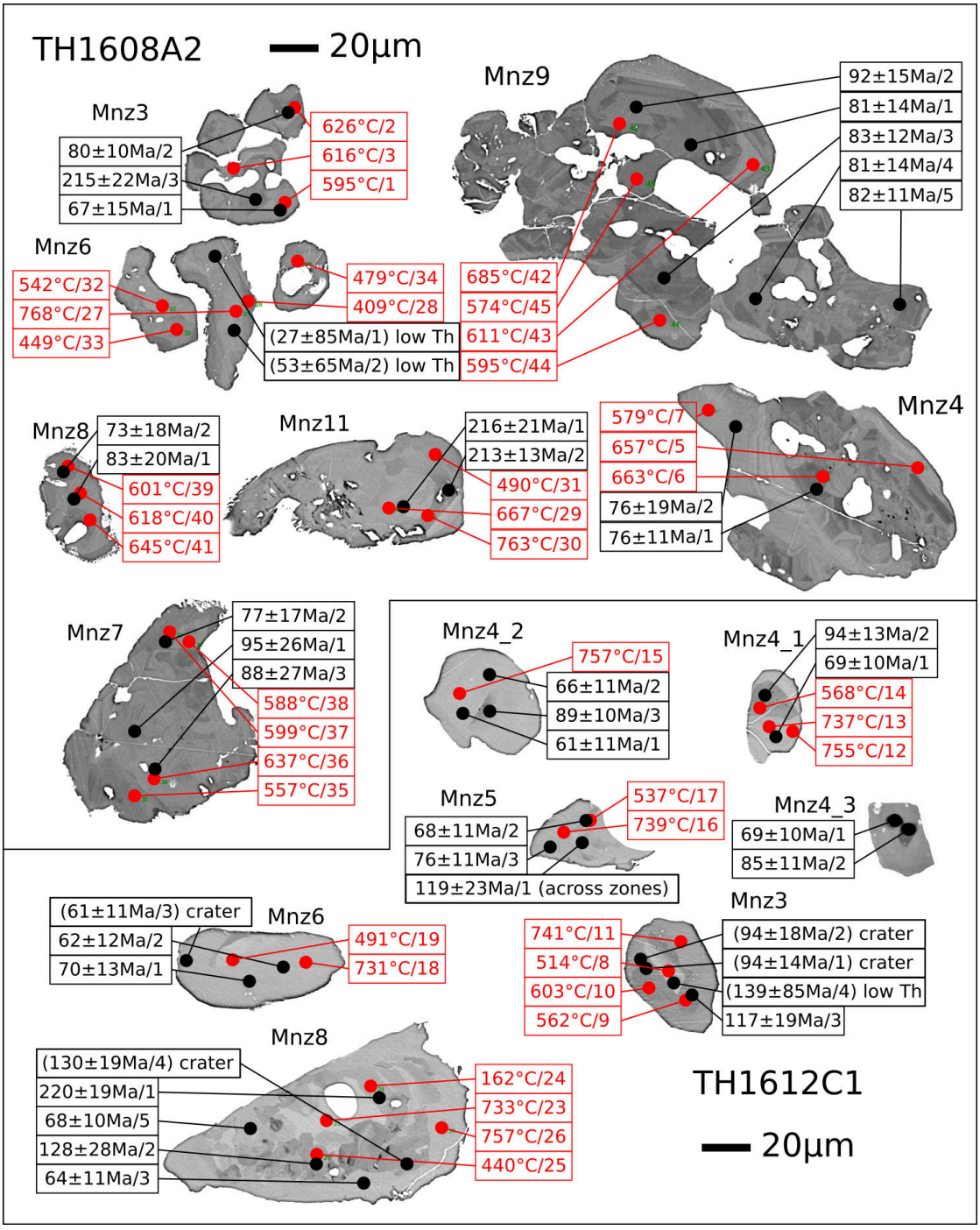

Figure 6.5.: Back-scattered electron images of monazites from this study, with (U+Th) total Pb ages (±2 σ) and Temperatures

7. Interpretation

7.1. Fieldwork

In fieldwork the approach was to follow the gneiss division after Kosuwan (1996) into the so called Haad Nai Phlao and Laem Thong Yang gneiss, which in some parts was quite challenging. Within the HNP-G layering could be observed, partly with intercalating calcsilicates, like it is described in Kosuwan (1996). However also attributes of a magmatic contact between the fine-grained and the coarse-grained HNP-G are visible, which may suggest to divide this two varieties of the HNP-G into different lithologies. Looking at the outcrops it is therefore difficult to make a statement as to whether the rocks are of magmatic or sedimentary origin (or both if they are separate lithologies), even though the parts where calcsilicates occure seem to be part of a paragneiss-sequence. This will be discussed further below in light of petrography and geochemistry. Although an attempt was made to find the transition between the HNP-G and the LTY-G, it still remains unclear. Albeit a more or less continuous outcrop from north to south on the coastline is present, no clear border could be observerd, which raises the question of whether or not the coarse grained HNP-G should be distinguished from the LTY-G, as petrographic and geochemical results from this study show several similarities.

On the basis of field investigation a relative age sequence of events can be reconstructed for the gneisses found on the eastern side of the Khanom complex near the coastline. The first step was the intrusion of the protolith from the HNP-G and the LTY-G into the older Khao Dat Fa gneiss. In a later stage the protolith from the L-G intruded in the LTY-G. Gneisses then got crosscut by pegmatite and aplite veins, whereas in the fine-grained HNP-G none of them were found. Afterwards all of whom were metamorphically overprinted, which is indicated by a structural overprint which extends over all lithologies (except the younger Khao Pret granite which is not described in this study). The Mylonite found in the south of the Khanom complex near the Sichon Fault, may reflect a vulcano-sedimentary sequence which was incorporated into the fault zone, and subsequently mylonitized.

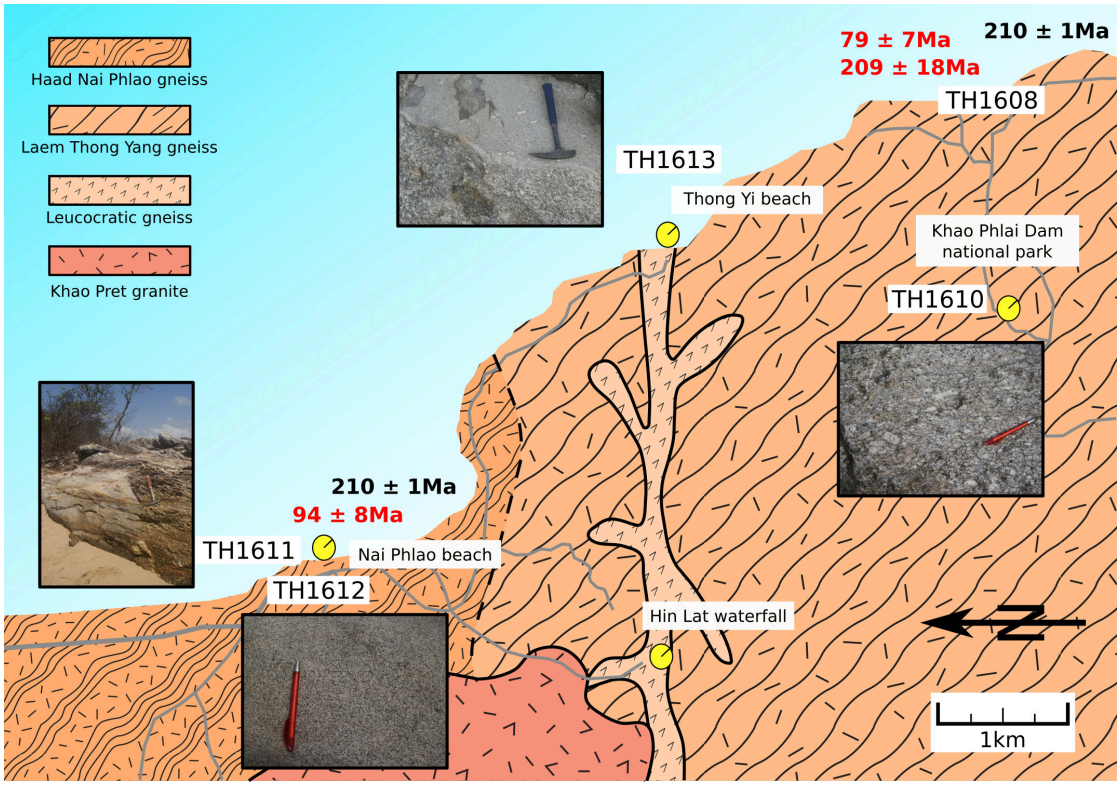

Figure 7.1.: Sketch of the relationship between rock units along the coastline from Haad Nai Phlao (N) to Laem Thong Yang (S), with relative locations of samples taken: TH1608 and TH1610 - LTY-G, TH1613 - L-G, TH1612 - coarse-grained HNP-G, TH1611 - fine-grained HNP-G, the contact between HNP-G and LTY-G remains questionable. The monazite and zircon ages refer to sample TH1612 and TH1608. Red numbers are monazite CHIME ages (see fig.6.3), black numbers are zircon U-Pb concordia ages (see fig.6.1)

7.2. Petrography

Thin sections of the two gneisses reveal magmatic features such as Karlsbader twins in feldspars, oscillatory zoning and perthitic exsolutions. Biotite inclusion in feldspar clasts exhibit the same pleochroism and habitus as biotites in the matrix, which indicates that both are of the same origin. The strongly altered K-feldspar "augen" and the kink bands in plagioclase are the product of dynamic recrystallisation, which is also present in quartz grains. It should also be mentioned that no garnet or sillimantite as described by Kosuwan (1996) were found in the HNP-G. However one sample from the fine-grained HNP-G (TH1611) shows amphiboles which are not described in any rocks described by Kosuwan (1996) and don't fit the description of the fine-grained HNP-G. The same sample also shows no muscovite or monazite. Only Hansen and

Wemmer (2011) and Hansen et al. (2014) mentioned a amphibole-bearing gneiss near Khao Phra Mountain.

Based on the mineral assemblage and microstructures mineral reactions can be derived. Spear et al. (1999) have done this for anatectic pelites in the NaKFMASH-system and constructed a petrogenetic grid, based on the assumption of a dry system, in which H2O is only introduced by dehydration reactions (see fig. 7.2). This model is used for a approximation of P-T condition. Although not found in samples of this study, sillimanite and garnet are described in the HNP-G (Kosuwan 1996) and will be implemented in mineral reactions. When going from low to high temperatures, the first important reaction encountered is the muscovite dehydration reaction:

muscovite + plagioclase + quartz = Al2SiO5 + K-feldspar + liquid (or H2O)

Since the formation of pronounced leucosomes in samples of this work cannot be identified, which would be evidence for pressures above invariant point 1 (IP1; see fig.7.2), pressures below IP1 are supported by the occurrence of abundant K-feldspar and only little muscovite. Nonetheless, it should be mentioned, that Kosuwan (1996) described partial melting as a process for the development of gneisses in the Khanom complex. Sautter et al. (2017) even described the HNP-G as a migmatite. The second important reaction would be the biotite dehydration reaction:

biotite + sillimanite = garnet + K-feldspar + quartz + liquid (or H2O)

With account of these reaction and the observation of this study suggestions can be made that pressures must be arround IP1 (4kbar) and since garnet is present in these rocks min. Temperatures of $\sim$700°C can be assumed.

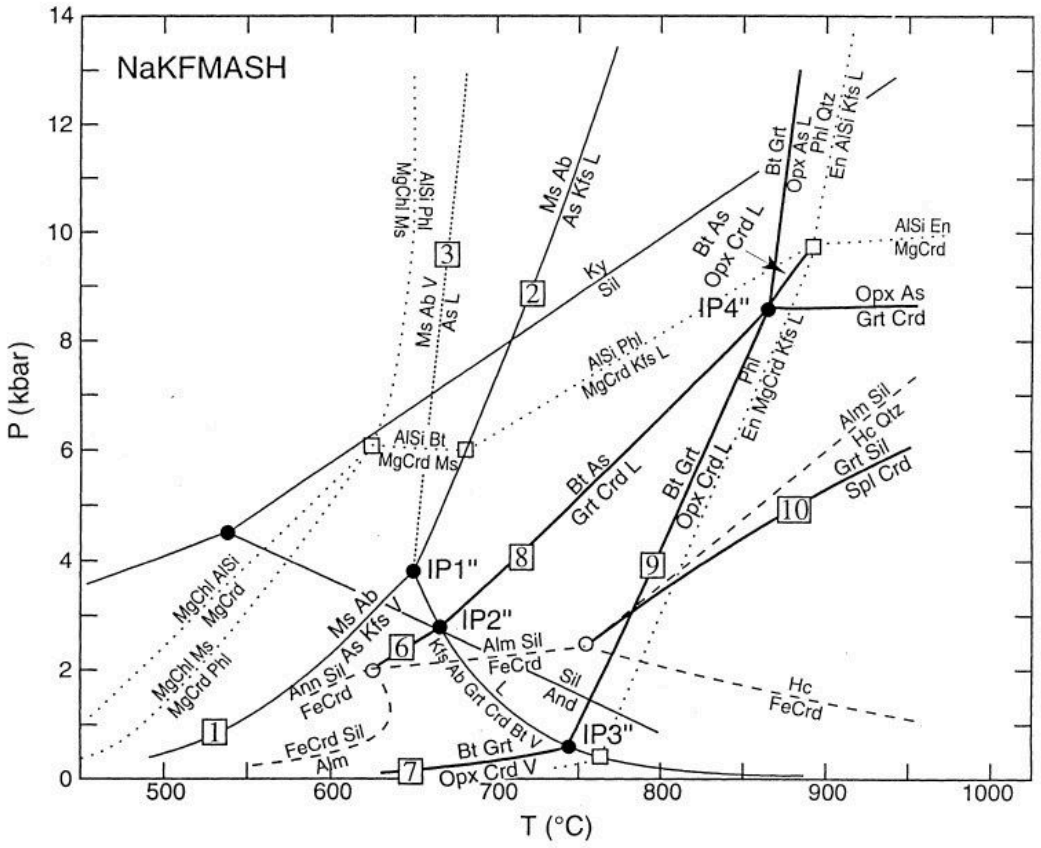

Figure 7.2.: Petrogenetic grid of NaKFMASH system after Spear et al. (1999) showing selected melting and dehydration reactions; dashed lines: KFASH system; dotted lines: KMASH system; finely dotted lines: pelite vapour-saturated melting reaction

7.3. Geochemistry

Geochemistry of major and trace elements of all samples, except one (the amphibole-bearing gneiss, TH1611), show peraluminous affinities that indicates convergent tectonics (see fig.4.10). The negative europium anomaly which appears in all samples, also less marked in the amphibole-bearing gneiss (TH1611), indicates that condition during emplacement of the protholith must have been such as to allow for plagioclase fractionation. Chappell and White (1974) first differentiate between S-type and I-type derived granite types. Further studies (White and Chappell 1983, Chappell and White 1992, Chappell and White 2001) supported this division and it is now well accepted. Application of this division shows that 4 out of 5 samples show S-type affinities with CIPW normative corundum content in range from 1.41-2.36% , an alumina saturation

index (A/CNK) around 1,1, high SiO2 and low CaO (see tab.B.2). In addition the presence of muscovite, monazite and ilmenite also suggest S-type affinities. These observations fit well with those of Kosuwan (1996) who assumed partial melting of metasedimentary source in a syn-collisional tectonic setting. However the amphibole-bearing gneiss shows I-type affinities. The alumina saturation index (0.96) suggest metaluminous affinities and it shows a very low CIPW normative corundum content (0.10%), low SiO2 and high CaO. It is also free of monazite, muscovite and ilmenite. Therefore a metaluminous I-type granite as protolith of the amphibole-bearing gneiss can be assumed. It should also be mentioned, that all samples are generally devoided in phases which are associated with S-type granites (e.g. garnet, cordierite, white mica) and show some typical magmatic textures (e.g. feldspar zonation). In addition Chappell et al. (2012) stated, that peraluminous I-type granites are not that uncommon. Therefore an I-type origin of the other gneisses of the Khanom complex (coarse-grained HNP-G, LTY-G and L-G) should be the object of further studies, as it can not yet be dismissed.

7.4. Geothermobarometry

Results from the Al-hornblende barometry and hornblende-plagioclase thermometry ($\sim$720 ± 35-40°C, $\sim$6.1 ± 0.6kbar) are in agreement with the observations of the petrographic study (at least for the temperature range), which show amphibolite facies conditions. In the petrogenetic grid of Spear et al. (1999) (see fig.7.2) higher pressures (above IP1) would support the formation of migmatites. However differences in composition can also shift P-T condition, especially Ti or F in biotite and Mn or Ca in garnet. In view of this, higher pressures of $\sim$6 kbar are possible.

Monazite-xenotime miscibility gap thermometry yield a wide range of temperatures ($\sim$400-770°C). This temperature range can be observed in single monazite grains. In some extend this can be expected as the gneisses of the Khanom complex are thought to be polymetamorph and monazite can grow in a wide range of P-T conditions. However all these temperatures where calculated with one pressure assumption (6.1 ± 0.6kbar) derived from the amphibole-bearing gneiss. Even though the rocks are close to each other, geochronological data suggest different histories. Therefore absolute values may vary to higher temperatures if lower pressures are assumed. Nonetheless, by comparing temperature zones with age zones in monazite grains, in order to understand the growth history of monazites, absolute values become less important. This was done for the measurements of a sample from the LTY-G (TH1608A2) and the coarse-grained HNP-G (TH1612C1), but no clear connections between temperature and age could be identified (see fig.6.5). This observation already made Cocherie et al. (1998), which implied in-situ recrystallisation involving only already existing material for this phenomena. By comparing temperature (see fig.5.1 and fig.5.2) and geochemistry data (see fig.4.17) from monazites of the HNP-G (TH1612C2), a bimodal distribution in both data sets is recognizable. Monazites show high temperatures ($\sim$740°C) in the rim region whereas cheralite-substitution is dominant and low tem-

peratures (∼550°C) at cores where huttonite-substitution is dominant. This is not visible for the LTY-G (TH1608A1/A2). Comparison between generation derived from zoning patterns of BSE-images and temperature points taken, show a prograde succession of generations for the HNP-G and a retrograde for the LTY-G (see fig.5.2). It should be mentioned, that monazites in all samples have very complex zoning pattern, which neither is oscillatory nor patchy but rather a mixture of both. Therefore, dividing different monazites into zones (generations) to select ideal points for measurements is quite challenging and a source for uncertainties. If this represents prograde/retrograde growth condition it is hard to imagine why these two samples, which show similarities in mineral composition and geochemistry, should show such differences in respect to monazite growth. This figure is therefore not interpreted to be of significance in a geological context. Other mechanisms, such as partial resetting of the geochemistry through later fluid activity for example, could be the cause for producing a falsified picture.

7.5. Zircon and monazite U-Th-Pb analyses

Zircon U-Pb analyses from the augengneiss (LTY-G; TH1608) reveal one dominant age spectrum ∼218-204 Ma, with a concordia age of 210.1 ± 0.8 Ma. Zircons of this Indosinian event predominantly show magmatic affinities with elongated prismatic habitus and oscillatory zoning (see fig.6.4). Th/U ratios >1 are associated with magmatic zircons, however all measured zircons show far lower values. One plausible explanation for this contradiction is the presence of monazite as Th-rich phase (Rubatto 2017). Monazites from the same sample also show these Indosinian ages, but they are by far not as dominant but rather overprinted by an Creteacouse event (∼95-67Ma), with a calculated CHIME age of 79.1 ± 6.9Ma. These monazites however show a anhedral habitus, indication of skeletal structure and patchy zoning features ascribed to metamorphic monazites and recrystallisation (Ayers et al. 1999). Zircon U-Pb analyses from the coarse-grained HNP-G (TH1612) compared with those of the LTY-G are very similar in size, appearance and TH/U ratios. They also show only one dominant age spectrum 199-215 Ma, with a concordia age of 209.7 ± 0.6 Ma. Monazite from this sample are comparable in size and appearance with those of the LTY-G, although indications of skeletal structure are not visible. Age data are way more scattered (130-61 Ma) and CHIME age calculation is not that reliable and yields a negative intercept. Nontheless, the data suggest a Cretaceous metamorphic event. Both gneisses (coarse-grained HNP-G and LTY-G) show one prae-Indosinian age in a zircon core, to which no geological meaning can be assigned. In summary it can be said, that two gneisses (LTY-G and coarse grained HNP-G) originate from the same protolith, which intruded at around 210 Ma. Furthermore a metamorphic event in the Cretaceous can be assumed.

A different story is told by the amphibole-bearing gneiss (fine-grained HNP-G; TH1611). While in the two gneisses discussed above the relatively small number of measurements suffice to get a clear picture, as they all are similar in appearance and

age, quite the opposite is true for this sample (see fig.6.4). Nonetheless some assumptions for the amphibole-bearing gneiss can be made. Zircon grains which yield early Eocene ages have a rather patchy pattern, are small in size and have low aspect ratios. Older zircon grains are more prismatic with higher aspect ratios and show oscillatory zonation, whereas a complex zoning pattern can occur in the cores. Also noticeable are three concordant Late Cambrian ages which are very close to each other and may represent an early Paleozoic event. As no clear succession of events can be derived from the amphibole-bearing gneiss from this study, it will be further discussed in comparison with the literature in the chapter 8 below.

Figure 7.3.: Lithostratigraphic table modified after Österle et al. (2019). CHIME monazite and SIMS zircon age data of this study (bold) are compared with other geo- and thermochronologic constraints from the Khanom metamorphic complex (Hansen and Wemmer 2011, Hansen et al. 2014, Kawakami et al. 2014, Sautter et al. 2019), the Mae Ping shear zone (MPSZ; Österle et al. 2019, Ahrendt et al. 1993, Pitsanupong et al. 2011, Lacassin et al. 1997, Meffre et al. 2007, Mickein 1997, Morley et al. 2007; Palin et al. 2013), the Mogok Metamorphic Belt (MMB; Barley et al. 2003, Gardiner et al. 2018, Searle et al. 2007), the Chiang Mai-Lincang Belt (CM-LB; Dunning et al. 1995; Gardiner et al. 2016b; Lan et al. 2007, Mickein 1997), the Three Pagodas (TPSZ; Lacassin et al. 1997, Nantasin et al. 2012), Klaeng (KSZ; Geard 2008, Kanjanapayont et al. 2013, Kawakami et al. 2014, Meffre et al. 2007), Ranong (RSZ; Watkinson et al. 2011) and Khlong Marui (KMSZ; Kanjanapayont et al. 2012; Watkinson et al. 2011) shear zones. Abbreviations: ZFT – zircon fission track, AFT - apatite fission track, mnz – monazite, zrc – zircon, TC - Thermochronology. Regional events are from Ridd et al. (2011) and Searle et al. (2007)

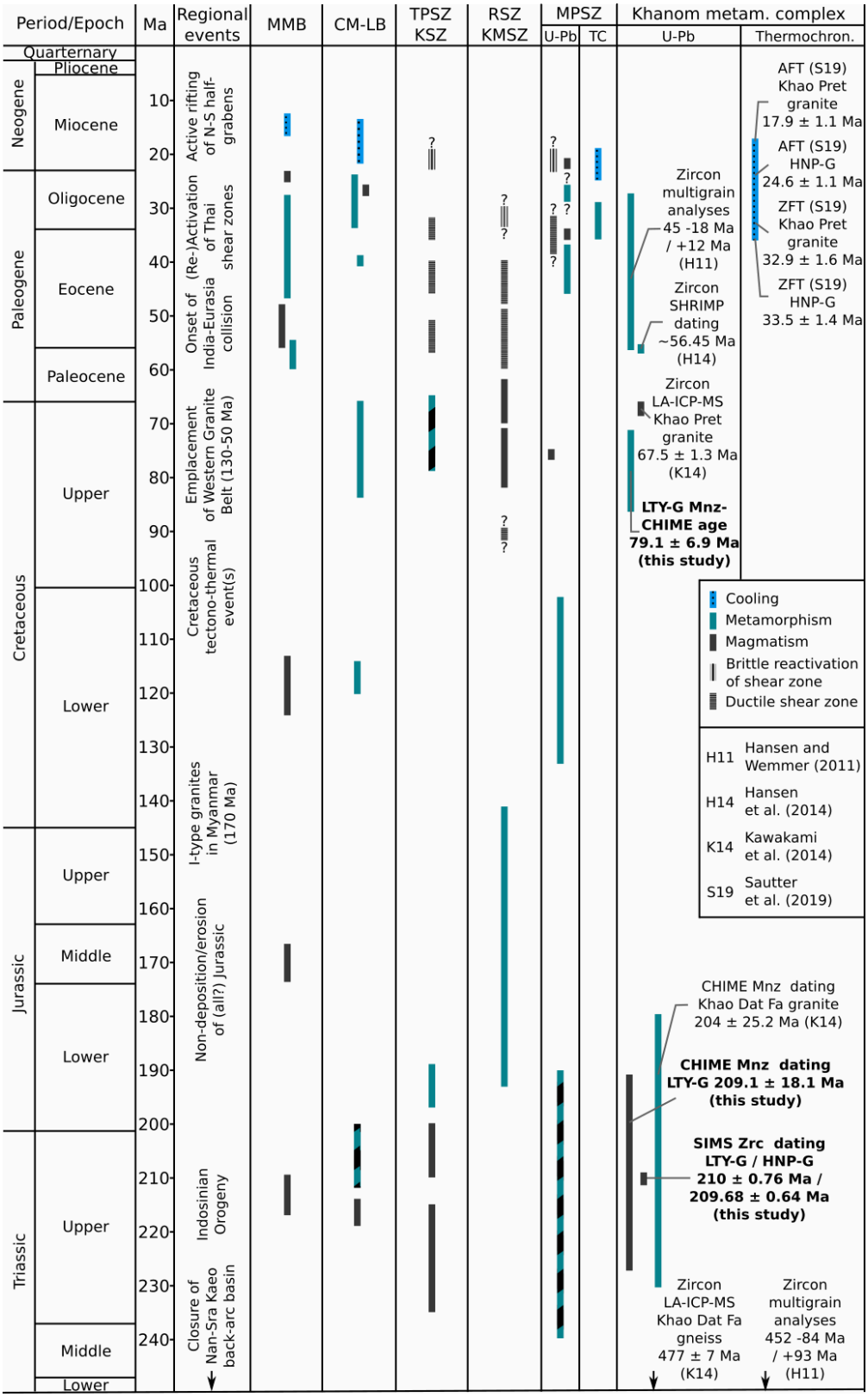
Period/Epoch
Ma
Regional events
MMB
CM-LB
TPSZ KSZ
RSZ KMSZ
MPSZ
U-Pb
TC
Khanom metam. complex
U-Pb
Thermochron.
Quarternary
Pliocene
Neogene
Miocene
Oligocene
Paleogene
Eocene
Paleocene
Upper
Cretaceous
Lower
Upper
Jurassic
Middle
Lower
Upper
Triassic
Middle
Lower
10
20
30
40
50
60
70
80
90
100
110
120
130
140
150
160
170
180
190
200
210
220
230
240
Active rifting of N-S half-grabens
(Re-)Activation of Thai shear zones
Onset of India-Eurasia collision
Emplacement of Western Granite Belt (130-50 Ma)
Cretaceous tectono-thermal event(s)
I-type granites in Myanmar (170 Ma)
Non-deposition/erosion of (all?) Jurassic
Indosinian Orogeny
Closure of Nan-Sra Kaeo back-arc basin
Zircon multigrain analyses 45 -18 Ma / +12 Ma (H11)
Zircon SHRIMP dating ~56.45 Ma (H14)
Zircon LA-ICP-MS Khao Pret granite 67.5 ± 1.3 Ma (K14)
LTY-G Mnz-CHIME age 79.1 ± 6.9 Ma (this study)
AFT (S19) Khao Pret granite 17.9 ± 1.1 Ma
AFT (S19) HNP-G 24.6 ± 1.1 Ma
ZFT (S19) Khao Pret granite 32.9 ± 1.6 Ma
ZFT (S19) HNP-G 33.5 ± 1.4 Ma
Cooling
Metamorphism
Magmatism
Brittle reactivation of shear zone
Ductile shear zone
H11 Hansen and Wemmer (2011)
H14 Hansen et al. (2014)
K14 Kawakami et al. (2014)
S19 Sautter et al. (2019)
CHIME Mnz dating Khao Dat Fa granite 204 ± 25.2 Ma (K14)
CHIME Mnz dating LTY-G 209.1 ± 18.1 Ma (this study)
SIMS Zrc dating LTY-G / HNP-G 210 ± 0.76 Ma / 209.68 ± 0.64 Ma (this study)
Zircon LA-ICP-MS Khao Dat Fa gneiss 477 ± 7 Ma (K14)
Zircon multigrain analyses 452 -84 Ma / +93 Ma (H11)

8. Discussion

Basement gneisses exposed in the Khanom complex reveal a long lasting history (see fig.7.3). In this study two major events could be recognised by dating zircons and monazite from the LTY-G and the coarse-grained HNP-G, one in the Late Triassic and one in the Late Cretaceous. Within the Khanom complex, comparable ages are only reported by Kawakami et al. (2014). CHIME monazite dating was done on samples from the HNP-G and LTY-G. CHIME ages however yielded negative intercepts, so they considered them as unreliable and suggested that apparent ages would be better age estimates (Kawakami et al. 2014). By comparing monazite apparent ages, their data also show a bimodal distribution and are slightly younger, but with a large uncertainty. The in-situ U-Pb dataset of zircons from this study, however, shows small uncertainties and very precise concordia ages from two samples (LTY-G TH1608 and HNP-G TH1612; see fig.6.1) in the Late Triassic. Therefore, zircons from the Khanom gneisses are interpreted to have crystallized at ∼210 Ma, which is also supported by magmatic affinities. Geochronologic studies done on similar granitic rocks belonging to the Sibumasu terrane (spread across Thailand and Malay Peninsular), show comparable ages ranging from Middle to Late Triassic (see fig.7.3; e.g. Ahrendt et al. 1993, Dunning et al. 1995, Gardiner et al. 2016a, Macdonald et al. 2010, Searle et al. 2012 Kawakami et al. 2014, Österle et al. 2019, Kanjanapayont et al. 2020). All these data suggest that the Indosinian orogeny was rather long lasting, consisting of many individual events and processes. Which processes are behind different events (e.g. U-Pb ages) is still a matter of debate. Some suggest protolith emplacement (Dunning et al. 1995, Gardiner et al. 2016a) others metamorphism (Ahrendt et al. 1993).Kanjanapayont et al. (2020) studied zircon generations across Thailand and developed a model for the crustal evolution of the Sibumasu terrane. The result is a two-step granitic magmatism, whereas the first may be related to anatexis melting during the Middle Triassic and the second due to cooling during the intrusion in the Late Triassic. Inherited cores suggest Neo-Proterozoic to Paleozoic precursors (Kanjanapayont et al. 2020). The application of this model to rocks of the Khanom complex shows no activity in the Middle Triassic, but only in the Late Triassic. It can be assumed that for the gneisses of the Khanom complex only one event around 210 Ma seems to be responsibly for their evolution during the late collisional stage of the Indosinian Orogeny. The process behind this event may be magmatic protolith emplacement, as zircons with magmatic affinities suggest. Two older inherited zircon cores (1011 ± 14 Ma, 324 ± 6 Ma) support the thesis that granitic magma was derived from Neo-Proterozoic to Paleozoic precursors (Kanjanapayont et al. 2020).

The Late Cretaceous ages observed in monazites in the gneisses of the Khanom complex show more scattering than the Late Triassic ones observed in zircons. Therefore

it is unclear if they represent one single event or rather a succession of two or more. What can be said is, that similar ages can be found in basement rocks all over Thailand and are often interpreted as a high temperature overprint, associated with I- and S-typ magmatism (Cobbing 2011, Palin et al. 2013, Kanjanapayont et al. 2012, Watkinson et al. 2011). For the gneisses examined in this study, the high thermal overprinting could have been caused by the intrusion of the L-G, which has not yet been dated. The intrusion of the Khao Pret granite (approx. 68 Ma, see Kawakami et al. 2014) could lead to a disruption of the isotopic system, which would rejuvenate the older monazite data from this study. This could explain the imprecise CHIME data from sample TH1612 (see fig.6.3) which is closer to the Khao Pret intrusion.
As can be seen from present findings, the sampled amphibole-bearing gneiss does not at all fit in with Kosuwan (1996)'s descriptions of the fine-grained HNP-G. Furthermore zircon U-Pb dating yield different ages than the rest of the gneisses in the Khanom area, which suggest a different origin for this amphibole-bearing gneiss. However Hansen and Wemmer (2011) and Hansen et al. (2014) described and dated a amphibole-gneiss in the Khanom complex. Conventional U-Pb zirccon ages yielded a lower intercept by 45 -18 Ma / +12 Ma and an upper intercept of 452 -84 Ma / +93 Ma (Hansen and Wemmer 2011). Their U/Pb-SHRIMP dating (Hansen et al. 2014) yielded a Paleocene age of 56.45 ± 0.72 Ma. They also mentioned three spots which reflect Indosinian ages and a few older concordant ages, the oldest beeing 612 ± 8 Ma. Kawakami et al. (2014) suggested that the amphibole-bearing gneiss dated by Hansen et al. (2014), could be derived from the Khao Dat Fa gneiss. Comparison between findings from this study and that from Hansen et al. (2014), show that ages doesn't fit that well. Nonetheless some similarities can be found. Both show young Paleocene ages, whereas that of Hansen et al. (2014) seems to be much more precise, some ages apparently reflecting the Indosinian Orogeny and a few older concordant ages are present. One interpretation for the history of the amphibole-bearing gneiss could be, that they derived from the Khao Dat Fa gneiss. Findings from this study may suggest that it was metamorphosed during the intrusion of the protolith from the LTY-G and the HNP-G in the Late Triassic and is represented as xenoliths at the contact to these gneisses. Afterwards they share the same history as the gneisses. It has to be mentioned that this interpretation is based on very little data and that its correctness has to be verified through further investigations.
The P-T condition during the events (Late Triassic, Late Cretaceous) have not been quantified for the Khanom complex. Results from the amphibole-plagioclase geothermobarometry yield high-temperature amphibolite-facies conditions (720 ± 35-40°C, 6.1 ± 0.6kbar). Whether these data represent the Late Triassic, Late Cretaceous or some other event can not be said as the formation and genesis of the amphibole-bearing gneiss in the Khanom complex is still a matter of debate. The temperatures derived from the Monazite-Xenotime miscibility gap thermometry (∼400-770°C) might rather reflect the Late Cretaceous event as most age data measured in the same monazite grains represents this period.

9. Conclusion

Petrological, chemical and geochronological methods were used to reconstruct the history of the gneisses from the Khanom complex. From the interpreted and discussed results above the following conclusions can be drawn:

- The contact between HNP-G and LTY-G is still questionable and it is unclear whether a direct contact exists at all. The similarities of the LTY-G and the coarse-grained HNP-G suggest that they may have the same origin. This and the fact that Kawakami et al. (2014) described a sillimanite-grad contact metamorphic aureole around the Khao Pret granite may suggest that the HNP-G is not a distinctive unit but rather the product of contact metamorphism in the Late Cretaceous.
- The protolith of the gneisses of the Khanom complex (LTY-G and coarse-grained HNP-G) intruded in the late stage of the Indosinian orogeny under syn-collisional conditions (∼210 Ma) and were thermally overprinted in the Late Cretaceous. Old zircon cores suggest a Neoproterozoic to Paleozoic precursor.
- The amphibole-bearing gneiss found in the Khanom complex shows a different history than the LTY-G and the HNP-G. It may be derived from the Khao Dat Fa gneiss as a result of contact metamorphism during the intrusion of the LTY-G and the HNP-G in the Late Triassic.
- Thermobarometry done on gneisses of the Khanom complex suggest maximum p-T condition of ∼720 ± 35-40°C and ∼6.1 ± 0.6kbar
- Comparison between this study and other literature shows similarities of the origin and tectonic evolution of basement rocks across Thailand and Malaya Peninsular, which leads to the conclusion that they share the same history and are part of the same entity. However the exact timing of different events and the mechanisms and processes behind them is still a matter of debate and will need further investigations.

Bibliography

Ahrendt, H., C. Chonglakmani, B. T. Hansen, and D. Helmcke (1993). "Geochronological cross section through northern Thailand". In: *Journal of Southeast Asian Earth Sciences* 8.1-4, pp. 207–217.

Anderson, J. L. and D. R. Smith (1995). "The effects of temperature and fO2 on the Al-in-hornblende barometer". In: *American Mineralogist* 80.5-6, pp. 549–559.

Ayers, J. C., C. Miller, B. Gorisch, and J. Milleman (1999). "Textural development of monazite during high-grade metamorphism: Hydrothermal growth kinetics, with implications for U,Th-Pb geochronology". In: *American Mineralogist* 84.11-12, pp. 1766–1780.

Barley, M. E., A. L. Pickard, K. Zaw, P. Rak, and M. G. Doyle (2003). "Jurassic to Miocene magmatism and metamorphism in the Mogok metamorphic belt and the India-Eurasia collision in Myanmar". In: *Tectonics* 22.3.

Black, L. P., S. L. Kamo, C. M. Allen, D. W. Davis, J. N. Aleinikoff, J. W. Valley, R. Mundil, I. H. Campbell, R. J. Korsch, I. S. Williams, and C. Foudoulis (2004). "Improved 206Pb/238U microprobe geochronology by the monitoring of a trace-element-related matrix effect; SHRIMP, ID-TIMS, ELA-ICP-MS and oxygen isotope documentation for a series of zircon standards". In: *Chemical Geology* 205.1-2, pp. 115–140.

Burda, J., U. Klötzli, B. Woskowicz-Ślezak, Q. L. Li, and Y. Liu (2020). "Inherited or not inherited: Complexities in dating the atypical 'cold' Chopok granite (Nízke Tatry Mountains, Slovakia)". In: *Gondwana Research* 87, pp. 138–161.

Chappell, B. W. and A. J. White (1974). "Two Contrasting Granite Types". In: *Pacific Geology* 8, pp. 173–174.

— (1992). "I- and S-type granites in the Lachlan Fold Belt". In: *Transactions of the Royal Society of Edinburgh: Earth Sciences* 83.1-2, pp. 1–26.

— (2001). "Two contrasting granite types: 25 years later". In: *Australian Journal of Earth Sciences* 48.4, pp. 489–499.

Chappell, B. W., C. J. Bryant, and D. Wyborn (2012). "Peraluminous I-type granites". In: *Lithos* 153, pp. 142–153.

Cobbing, E. J. (2011). "Granitic Rocks". In: *The Geology of Thailand*. Chap. 16, pp. 441–457.

Cocherie, A., O. Legendre, J. J. Peucat, and A. N. Kouamelan (1998). "Geochronology of polygenetic monazites constrained by in situ electron microprobe Th-U-total lead determination: Implications for lead behaviour in monazite". In: *Geochimica et Cosmochimica Acta* 62.14, pp. 2475–2497.

Dunning, G. R., A. S. Macdonald, and S. M. Barr (1995). "Zircon and monazite UPb dating of the Doi Inthanon core complex, northern Thailand: implications for extension within the Indosinian Orogen". In: *Tectonophysics* 251.1-4, pp. 197–213.

Gardiner, N. J., M. P. Searle, C. K. Morley, M. P. Whitehouse, C. J. Spencer, and L. J. Robb (2016a). "The closure of Palaeo-Tethys in Eastern Myanmar and Northern Thailand: New insights from zircon U–Pb and Hf isotope data". In: *Gondwana Research* 39, pp. 401–422.

Gardiner, N. J., N. M. W. Roberts, C. K. Morley, M. P. Searle, and M. J. Whitehouse (2016b). "Did Oligocene crustal thickening precede basin development in northern Thailand? A geochronological reassessment of Doi Inthanon and Doi Suthep". In: *Lithos* 240, pp. 69–83.

Gardiner, N. J., M. P. Searle, C. K. Morley, L. J. Robb, M. J. Whitehouse, N. M. W. Roberts, C. L. Kirkland, and C. J. Spencer (2018). "The crustal architecture of Myanmar imaged through zircon U-Pb, Lu-Hf and O isotopes: Tectonic and metallogenic implications". In: *Gondwana Research* 62, pp. 27–60.

Geard, A. (2008). "Geology of the Klaeng Region (southeast Thailand): lithology, structure and geochronology". In: *BSc Hons thesis, University of Tasmania, Hobart*.

Gratz, R. and W. Heinrich (1997). "Monazite-xenotime thermobarometry: Experimental calibration of the miscibility gap in the binary system CePO4-YPO4". In: *American Mineralogist* 82.7-8, pp. 772–780.

Hammarstrom, J. M. and E. Zen (1986). "Aluminum in hornblende: an empirical igneous geobarometer." In: *American Mineralogist* 71.11-12, pp. 1297–1313.

Hansen, B. and K. Wemmer (2011). "Age and evolution of the basement rocks in Thailand". In: *The Geology of Thailand*, pp. 19–31.

Hansen, B., K. Wemmer, P. Putthapiban, I. C. Kleinhanns, and F. Wilsky (2014). "Do U / Pb-SHRIMP Dating and Pb Stepwise Leaching (PbSL) Analyses Confirm the Lack of Precambrian Basement Outcrops in Thailand ?" In: *Open Journal of Geology* 4.October, pp. 505–517.

Hawthorne, F. C., R. Oberti, G. E. Harlow, W. V. Maresch, R. F. Martin, J. C. Schumacher, and M. D. Welch (2012). "Ima report: Nomenclature of the amphibole supergroup". In: *American Mineralogist* 97.11-12, pp. 2031–2048.

Heinrich, W., G. Andrehs, and G. Franz (1997). "Monazite – xenotime miscibility gap thermometry . I . An empirical calibration". In: *Journal of Metamorphic Geology* 15.I, pp. 3–16.

Holland, T. and J. Blundy (1994). "Non-ideal interactions in calcic amphiboles and their bearing on amphibole-plagioclase thermometry". In: *Contributions to Mineralogy and Petrology* 116.4, pp. 433–447.

Hutchison, C. S. (2014). "Tectonic evolution of Southeast Asia". In: *Bulletin of the Geological Society of Malaysia* 60.December, pp. 1–18.

Johnson, M. C. and M. J. Rutherford (1989). "Experimental calibration of the aluminum-in-hornblende geobarometer with application of Long Valley caldera (California) volcanic rocks". In: *Geology* 17.9, pp. 837–841.

Kanjanapayont, P., P. Kieduppatum, U. Klötzli, E. Klötzli, and P. Charusiri (2013). "Deformation history and U–Pb zircon geochronology of the high grade metamorphic rocks within the Klaeng fault zone, eastern Thailand". In: *Journal of Asian Earth Sciences* 77, pp. 224–233.

Kanjanapayont, P., U. Klötzli, and N. Frank (2020). "Dating multiple generation of zircons from granites and gneiss from Thailand: Implication for the crustal evolution of the Sibumasu terrane". In: *Journal of Asian Earth Sciences* 190, p. 104148.

Kanjanapayont, P., U. Klötzli, M. Thöni, B. Grasemann, and M. A. Edwards (2012). "Rb-Sr, Sm-Nd, and U-Pb geochronology of the rocks within the Khlong Marui shear zone, southern Thailand". In: *Journal of Asian Earth Sciences* 56, pp. 263–275.

Kawakami, T., N. Nakano, F. Higashino, T. Hokada, Y. Osanai, M. Yuhara, P. Charusiri, H. Kamikubo, K. Yonemura, and T. Hirata (2014). "U-Pb zircon and CHIME monazite dating of granitoids and high-grade metamorphic rocks from the Eastern and Peninsular Thailand - A new report of Early Paleozoic granite". In: *Lithos* 200-201.1, pp. 64–79.

Konečný, P., M. A. Kusiak, and D. J. Dunkley (2018). "Improving U-Th-Pb electron microprobe dating using monazite age references". In: *Chemical Geology* 484.2017, pp. 22–35.

Kosuwan, S. (1996). *Geology of the Khanom gneissic complexes, Amphoe Khanom, Changwat Nakhon Si Thammarat*.

Lacassin, R., H. Maluski, P. H. Leloup, P. Tapponnier, C. Hinthong, K. Siribhakdi, S. Chuaviroj, and A. Charoenrav (1997). "Tertiary diachronic extrusion and deformation of western Indochina: Structural and 4øAr/39Ar evidence from NW Thailand". In: *JOURNAL OF GEOPHYSICAL RESEARCtt* 102.96.

Lan, C. Y., T. Usuki, T. Y. Lee, T. Y. Yeh, and P. Charusiri (2007). "Geochronology for the Gneiss Complex from the Shan-Thai Block in Thailand". In: *Internation Association for Gondwana Research Conference Series 4. Japan*, pp. 102.

Li, X. H., Y. Liu, Q. L. Li, C. H. Guo, and K. R. Chamberlain (2009). "Precise determination of Phanerozoic zircon Pb/Pb age by multicollector SIMS without external standardization". In: *Geochemistry, Geophysics, Geosystems* 10.4, pp. 1–21.

Liu, Y., Q. L. Li, G. Q. Tang, X. H. Li, and Q. Z. Yin (2015). "Towards higher precision SIMS U-Pb zircon geochronology via dynamic multi-collector analysis". In: *Journal of Analytical Atomic Spectrometry* 30.4, pp. 979–985.

Locock, A. J. (2014). "An Excel spreadsheet to classify chemical analyses of amphiboles following the IMA 2012 recommendations". In: *Computers and Geosciences* 62, pp. 1–11.

Macdonald, A. S., S. M. Barr, B. V. Miller, P. H. Reynolds, B. P. Rhodes, and B. Yokart (2010). "P-T-t constraints on the development of the Doi Inthanon metamorphic core complex domain and implications for the evolution of the western gneiss belt, northern Thailand". In: *Journal of Asian Earth Sciences* 37.1, pp. 82–104.

Meffre, S., K. Zaw, S. Khositanont, and A. Harris (2007). "New LA ICP–MS zircon age of gneissic complexes in Thailand: Implications for SE Asian tectonics." In: *Asia Oceania Geoscience Society (AOGS)* 30.4th Meeting, Bangkok, Thailand.

Metcalfe, I. (2013). "Gondwana dispersion and Asian accretion: Tectonic and palaeogeographic evolution of eastern Tethys". In: *Journal of Asian Earth Sciences* 66, pp. 1–33.

Mickein, A. (1997). *U/Pb-, Rb/Sr-und K/Ar-Untersuchungen zur metamorphen Entwicklung und Altersstellung des" Präkambriums" in NW-Thailand*. Vol. 73. Im Selbstverlag der Geologischen Institute der Georg-August-Universität ...

Morley, C. K., M. Smith, A. Carter, P. Charusiri, and S. Chantraprasert (2007). "Evolution of deformation styles at a major restraining bend, constraints from cooling histories, Mae Ping fault zone, western Thailand". In: *Geological Society, London, Special Publications* 290.1, pp. 325–349.

Morley, C. K., P. Charusiri, and I. M. Watkinson (2011). "Structural geology of Thailand during the Cenozoic". In: *The Geology of Thailand*, pp. 273–334.

Nantasin, P., C. Hauzenberger, X. Liu, K. Krenn, Y. Dong, M. Thöni, and P. Wathanakul (2012). "Occurrence of the high grade Thabsila metamorphic complex within the low grade Three Pagodas shear zone, Kanchanaburi Province, western Thailand: Petrology and geochronology". In: *Journal of Asian Earth Sciences* 60, pp. 68–87.

O'Conner, J. T. (1965). "A Classification for quartz-rich igneous rocks based on feldspar ratios". In: *US Geological Survey* 525B, B79–B84.

Österle, J. E., U. Klötzli, D. F. Stockli, M. Palzer-Khomenko, and P. Kanjanapayont (2019). "New age constraints on the Lan Sang gneiss complex, Thailand, and the timing of activity of the Mae Ping shear zone from in-situ and depth-profile zircon and monazite U-Th-Pb geochronology". In: *Journal of Asian Earth Sciences* 181.June, p. 103886.

Palin, R. M., M. P. Searle, C. K. Morley, P. Charusiri, M. S. Horstwood, and N. M. Roberts (2013). "Timing of metamorphism of the Lansang gneiss and implications for left-lateral motion along the Mae Ping (Wang Chao) strike-slip fault, Thailand". In: *Journal of Asian Earth Sciences* 76, pp. 120–136.

Pearce, J. A., N. B. Harris, and A. G. Tindle (1984). "Trace element discrimination diagrams for the tectonic interpretation of granitic rocks". In: *Journal of Petrology* 25.4, pp. 956–983.

Pitsanupong, K., K. Urs, C. Punya, and K. Eva (2011). "LA-MC-ICP-MS U-Pb zircon geochronology of the Lan Sang and Nong Yai gneisses , Thailand". In: December, pp. 2–5.

Ridd, M. F., A. J. Barber, and M. J. Crow (2011). "Introduction to the geology of Thailand". In: *The Geology of Thailand*, pp. 1–17.

Rubatto, D. (2017). *Zircon: The Metamorphic Mineral*. Vol. 83. 1, pp. 261–295.

Sautter, B., M. Pubellier, P. Jousselin, P. Dattilo, Y. Kerdraon, C. M. Choong, and D. Menier (2017). "Late Paleogene rifting along the Malay Peninsula thickened crust". In: *Tectonophysics* 710-711, pp. 205–224.

Sautter, B., M. Pubellier, S. Králiková Schlögl, L. Matenco, P. Andriessen, and M. Mathew (2019). "Exhumation of west Sundaland: A record of the path of India?" In: *Earth-Science Reviews* 198.August, p. 102933.

Schmidt, M. W. (1992). "Amphibole composition in tonalite as a function of pressure: an experimental calibration of the Al-in-hornblende barometer". In: *Contributions to Mineralogy and Petrology* 110.2-3, pp. 304–310.

Searle, M. P., S. R. Noble, J. M. Cottle, D. J. Waters, A. H. G. Mitchell, T. Hlaing, and M. S. A. Horstwood (2007). "Tectonic evolution of the Mogok metamorphic belt, Burma (Myanmar) constrained by U-Th-Pb dating of metamorphic and magmatic rocks". In: *Tectonics* 26.3.

Searle, M. P., M. J. Whitehouse, L. J. Robb, A. A. Ghani, C. S. Hutchison, M. Sone, S. W.-. P. Ng, M. H. Roselee, S.-. L. Chung, and G. J. H. Oliver (2012). "Tectonic evolution of the Sibumasu-Indochina terrane collision zone in Thailand and Malaysia: constraints from new U-Pb zircon chronology of SE Asian tin granitoids". In: *Journal of the Geological Society* 169.4, pp. 489–500.

Searle, M. P. (2018). "Timing of subduction initiation, arc formation, ophiolite obduction and India–Asia collision in the Himalaya". In: *Geological Society, London, Special Publications*, SP483.8.

Searle, M. P. and C. K. Morley (2011). "Tectonic and thermal evolution of Thailand in the regional context of Southeast Asia". In: *The Geology of Thailand*. May, pp. 539–572.

Seydoux-Guillaume, A. M., R. Wirth, W. Heinrich, and J. M. Montel (2002). "Experimental determination of Thorium partitioning between monazite and xenotime using analytical electron microscopy and X-ray diffraction Rietveld analysis". In: *European Journal of Mineralogy* 14, pp. 869–878.

Shand, S. J. (1943). *The Eruptive Rocks*. 2nd. John Wiley, p. 444.

Spear, F. S. and J. M. Pyle (2002). "Apatite, Monazite, and Xenotime in Metamorphic Rocks". In: *Reviews in Mineralogy and Geochemistry* 48.1, pp. 293–335.

Spear, F. S., M. J. Kohn, and J. T. Cheney (1999). "P-T paths from anatectic pelites". In: *Contributions to Mineralogy and Petrology* 134.1, pp. 17–32.

Stacey, J. S. and J. D. Kramers (1975). "Approximation of terrestrial lead isotope evolution by a two-stage model". In: *Earth and Planetary Science Letters* 26.2, pp. 207–221.

Streckeisen, A. (1974). "Classification and nomenclature of plutonic rocks". In: *Geologishe Rundschau* 63.2, pp. 773–786.

Tapponnier, P., G. Peltzer, A. Y. Le Dain, R. Armijo, and P. Cobbold (1982). "Propagating extrusion tectonics in Asia: new insights from simple experiments with plasticine." In: *Geology* 10.12, pp. 611–616.

Vermeesch, P. (2018). "IsoplotR: A free and open toolbox for geochronology". In: *Geoscience Frontiers* 9.5, pp. 1479–1493.

Watkinson, I., C. Elders, G. Batt, F. Jourdan, R. Hall, and N. J. McNaughton (2011). "The timing of strike-slip shear along the Ranong and Khlong Marui faults, Thailand". In: *Journal of Geophysical Research: Solid Earth* 116.9, pp. 1–26.

White, A. J. and B. W. Chappell (1983). "Granitoid types and their distribution in the Lachlan Fold Belt, southeastern Australia". In: *Memoir of the Geological Society of America* 159.1, pp. 21–34.

Wiedenbeck, M., P. Allé, F. Corfu, W. L. Griffin, M. Meier, F. Oberli, A. von Quadt, J. C. Roddick, and W. Spiegel (1995). "Three Natural Zircon Standards for U-Th-Pb, Lu-Hf, Trace Element and Ree Analyses". In: *Geostandards Newsletter* 19.1, pp. 1–23.

Appendix A. Sample locations and measurements

Samplenumber	Lithology	Coordinates
TH1601	Calcsilicate	N 09°08.358′, E 99°52.591′
TH1602A	Calcsilicate	N 09°08.267′, E 99°52.639′
TH1602B	Calcsilicate	N 09°08.267′, E 99°52.639′
TH1602C	Calcsilicate	N 09°08.267′, E 99°52.639′
TH1603A	Leucocrate gneiss	N 09°06.860′, E 99°53.930′
TH1603B	Leucocrate gneiss	N 09°06.860′, E 99°53.930′
TH1604AR*	Conglomerate of blueshist and amphibolite facies units	N 09° 06.519, E 99°52.048
TH1604BR*	Conglomerate of blueshist and amphibolite facies units	N 09° 06.519, E 99°52.049
TH1605	Fine-grained biotite gneiss	N 09°06.468′, E 99°51.955′
TH1605R*	Calcsilicate	N 09°06.468′, E 99°51.955′
TH1606A	Leucocratic gneiss	N 09°06.734′, E 99°52.232′
TH1606BR*	Fine-grained biotite gneiss, dark variety	N 09°06.734′, E 99°52.232′
TH1607	Biotite gneiss, biotitecluster	N 09°06.465′, E 99°52.098′
TH1608A	Biotite augengneiss	N 09°05.330′, E 99°54.602′
TH1608B	Biotite augengneiss	N 09°05.330′, E 99°54.602′
Th1609A	Fine grained mylonite	N 09° 04.740′, E 99°53.315′
TH1610A	Biotite augengneiss	N 09°05.435′, E 99°53.635′
TH1610B	Biotite augengneiss	N 09°05.435′, E 99°53.635′
TH1611A	Fine-grained biotite gneiss	N 09°08.372′, E 99°52.557′
TH1611B	Fine-grained biotite gneiss	N 09°08.372′, E 99°52.557′
TH1612A	Coarse-grained biotite gneiss	N 09°08.352′, E 99°52.600′
TH1612B	Coarse-grained biotite gneiss	N 09°08.352′, E 99°52.600′
TH1612C	Coarse-grained biotite gneiss	N 09°08.352′, E 99°52.600′
TH1612D	Coarse-grained biotite gneiss	N 09°08.352′, E 99°52.600′
TH1613	Leucocrate gneiss	N 09°06.833′, E 99°53.918′
TH1614A	Fine-grained biotite gneiss	N 09°08.250′, E 99°50.861′
TH1614B	Fine-grained biotite gneiss	N 09°08.250′, E 99°50.861′

Table A.1.: Sample locations (* R not in-situ)

	S1		L1		S2	
	Strike	Dip	Plunge	Azimuth	Strike	Dip
Along coastline: Nai Phlao Beach - Thong Yi Beach			15	354	022	20
	082	40	11	338		
	057	51	14	350		
	055	60	12	345		
	068	58	06	340	018	18
	069	53	04	342		
	061	54	11	337		
Phlai Dam Beach	050	63				
	060	63				

Table A.2.: Foliation of gneisses in Khanom area: S1 Schistosity 1; L1 Lineation 1; S2 Schistosity 2

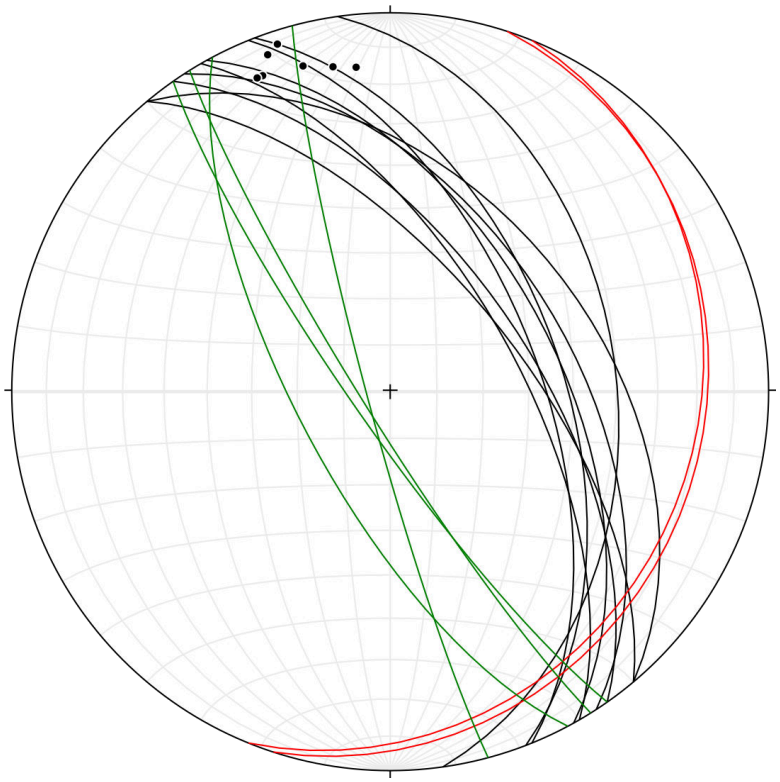

Figure A.1.: black planes represents S1, red planes S2, black dots L1, green planes represents mylonite layers

Appendix B. Petrology

B.1. Whole rock geochemistry

	TH1608A	TH1610	TH1611	TH1612	TH1613
Ba	888	729	978	639	62.8
Ce	89.5	74.9	104	70.8	6.5
Cr	140	30	20	30	20
Cs	25.5	35.6	3.94	15.7	4.33
Dy	5.93	6.04	5.5	6.25	1.28
Er	2.86	3.01	3.05	3.47	0.6
Eu	1.13	1.04	1.95	1.02	0.14
Ga	17.1	17.3	19.8	17.4	22.5
Gd	6.77	6.27	6.71	6.47	0.98
Hf	3.9	4.4	6.4	4.8	0.8
Ho	1.14	1.09	1.18	1.23	0.23
La	43.9	37.7	57	35.4	3.3
Lu	0.39	0.42	0.44	0.46	0.1
Nb	10.2	11.4	12.3	14.1	6.3
Nd	38.3	33.1	43	31.1	2.8
Pr	10.5	9.12	12	8.61	0.78
Rb	346	406	154	293	340
Sm	8.11	7.06	8.04	6.63	1.02
Sn	6	12	3	7	5
Sr	86.1	76.7	784	67.1	12.3
Ta	0.7	1.2	0.6	1.4	0.2
Tb	1.04	0.98	1.01	1.04	0.22
Th	27.7	23.8	14.3	21.4	2.56
Tm	0.4	0.37	0.39	0.44	0.08
U	4.14	9.71	3.49	4.75	3.1
V	22	32	103	39	6
W	40	77	25	79	79
Y	28.9	28.9	31.1	33.9	7
Yb	2.38	2.68	2.79	3.21	0.73
Zr	139	162	277	179	28
SiO_2	73.2	74.6	60.5	74.4	75.2
Al_2O_3	14.1	13.8	16.65	13.2	14.1
Fe_2O_3	1.77	2.25	5.4	2.59	0.42

	TH1608A	TH1610	TH1611	TH1612	TH1613
CaO	1.16	1.22	4.25	1.38	0.5
MgO	0.41	0.51	1.96	0.64	0.15
Na2O	2.83	3.31	3.16	3.29	3.66
K2O	5.65	4.21	4.15	3.56	5.03
Cr2O3	0.019	0.003	0.002	0.003	0.002
TiO2	0.27	0.33	0.6	0.39	0.04
MnO	0.02	0.04	0.1	0.04	0.01
P2O5	0.11	0.13	0.43	0.15	0.26
SrO	<0.01	<0.01	0.08	<0.01	<0.01
BaO	0.11	0.09	0.11	0.08	0.01
LOI	0.81	0.91	0.94	0.68	0.83
Total	100.46	101.4	98.33	100.4	100.21

Table B.1.: Whole Rock Data, elements in ppm and oxides in wt%

	TH1608A	TH1610	TH1611	TH1612	TH1613
Quartz	31.33	34.73	12.44	36.80	34.06
Plagioclase	29.17	33.14	46.72	33.90	31.96
(Albite)	24.08	27.93	27.60	27.98	31.17
(Anorthite)	5.09	5.21	19.12	5.92	0.79
Orthoclase	33.93	25.10	25.72	21.41	29.94
Corundum	1.41	1.82	0.10	1.74	2.36
Hypersthene	3.01	3.83	11.76	4.55	0.90
Ilmenite	0.52	0.62	1.18	0.74	0.08
Magnetite	0.31	0.39	0.97	0.45	0.07
Apatite	0.26	0.31	1.05	0.36	0.62
Zircon	0.03	0.03	0.06	0.04	0.01
Chromite	0.03	0.01	0.00	0.01	0.00
Total	100.00	100.00	100.00	100.00	100.00

Table B.2.: CIPW-Norm after Kurt Hollocher, Geology Department, Union College, Schenectady, NY

B.2. Mineral geochemistry

Na2O	SiO2	MgO	Al2O3	K2O	CaO	TiO2	FeO	MnO	BaO	Total	Sample	DataSet/Point
9.202	66.621	0.004	21.634	0.135	2.906	0	0.096	0.01	0	100.608	TH1608A1	11 / 1 .
9.935	65.911	0.064	21.583	0.178	2.087	0	0.197	0.001	0.04	99.996	TH1608A1	12 / 1 .
8.92	62.993	0	23.876	0.255	4.481	0.009	0.183	0.009	0.021	100.747	TH1608A1	13 / 1 .
8.966	62.654	0	23.62	0.146	4.53	0	0	0.01	0.025	99.952	TH1608A1	17 / 1 .
8.795	62.921	0	23.69	0.163	4.771	0.005	0.016	0.001	0.025	100.386	TH1608A1	18 / 1 .
8.887	62.823	0	23.739	0.149	4.664	0	0	0	0.003	100.266	TH1608A1	19 / 1 .
11.343	67.844	0	20.13	0.135	0.437	0.026	0.004	0.005	0	99.924	TH1608A1	21 / 1 .
9.158	63.665	0.014	23.248	0.146	4.107	0	0	0.004	0.005	100.346	TH1608A1	24 / 1 .
9.472	64.232	0.002	22.854	0.19	3.561	0	0.016	0.01	0.029	100.366	TH1608A1	25 / 1 .
9.165	63.56	0.022	23.296	0.174	4.041	0.009	0.095	0.003	0	100.365	TH1608A1	26 / 1 .
8.681	62.393	0.002	23.823	0.285	4.842	0	0.054	0	0	100.081	TH1608A1	28 / 1 .
9.065	63.6	0	23.411	0.246	4.298	0.023	0.148	0.002	0.031	100.824	TH1608A1	29 / 1 .
9.119	63.185	0	23.377	0.194	4.085	0.014	0.027	0.004	0.023	100.03	TH1608A1	40 / 1 .
8.967	62.349	0	23.815	0.198	4.634	0	0.026	0.008	0	99.998	TH1608A1	41 / 1 .
8.844	62.241	0	23.642	0.215	4.567	0	0.029	0	0	99.539	TH1608A1	42 / 1 .
9.077	62.877	0.001	23.473	0.182	4.302	0	0.171	0.015	0.014	100.112	TH1608A1	43 / 1 .
9.066	63.37	0	23.518	0.205	4.233	0.007	0.369	0	0.012	100.78	TH1608A1	44 / 1 .
9.155	62.881	0	23.461	0.215	4.369	0	0.31	0.001	0.023	100.416	TH1608A1	45 / 1 .
8.795	62.436	0	23.761	0.231	4.761	0	0.065	0	0	100.05	TH1608A2	101 / 1 .
8.913	62.529	0	23.548	0.129	4.603	0.011	0.034	0.006	0.01	99.782	TH1608A2	102 / 1 .
11.352	68.367	0	20.113	0.136	0.25	0.018	0.017	0.004	0.036	100.292	TH1608A2	114 / 1 .
10.964	67.297	0.017	20.634	0.112	0.966	0	0	0.01	0	100	TH1608A2	115 / 1 .
9	62.606	0.017	23.766	0.141	4.621	0	0.016	0	0	100.167	TH1608A2	135 / 1 .
8.957	62.863	0.009	23.638	0.21	4.617	0.037	0.013	0	0	100.346	TH1608A2	139 / 1 .
8.792	62.776	0	23.751	0.229	4.661	0	0.05	0.017	0.06	100.336	TH1608A2	140 / 1 .
8.863	62.728	0	23.718	0.175	4.624	0.015	0.027	0.006	0.006	100.161	TH1608A2	141 / 1 .
8.825	62.545	0	23.621	0.198	4.67	0	0.104	0.006	0	99.97	TH1608A2	142 / 1 .

Na2O	SiO2	MgO	Al2O3	K2O	CaO	TiO2	FeO	MnO	BaO	Total	Sample	DataSet/Point
8.638	62.137	0.007	23.791	0.208	4.822	0.024	0.001	0	0	99.628	TH1608A2	153 / 1 .
8.66	62.309	0	23.8	0.194	4.876	0.005	0.024	0.009	0.003	99.88	TH1608A2	154 / 1 .
8.606	62.141	0.001	23.91	0.298	4.905	0	0.02	0	0.008	99.89	TH1608A2	155 / 1 .
10.421	66.037	0.018	21.437	0.123	1.729	0	0.432	0.018	0	100.215	TH1611B2	10 / 1 .
7.316	59.231	0.01	25.9	0.173	7.339	0.015	0.354	0.002	0	100.34	TH1611B2	13 / 1 .
7.727	60.286	0	25.396	0.204	6.454	0	0.231	0	0.011	100.31	TH1611B2	27 / 1 .
7.403	59.738	0.008	25.799	0.193	7.034	0.021	0.3	0.01	0	100.506	TH1611B2	28 / 1 .
7.388	59.338	0.012	25.754	0.155	6.988	0.015	0.063	0.001	0	99.714	TH1611B2	29 / 1 .
7.342	59.479	0.007	25.916	0.177	7.239	0	0.165	0	0.02	100.344	TH1611B2	40 / 1 .
7.112	59.161	0	26.119	0.172	7.665	0	0.231	0	0.035	100.494	TH1611B2	45 / 1 .
7.333	59	0	26.177	0.131	7.683	0.003	0.107	0	0.017	100.451	TH1611B2	46 / 1 .
7.735	60.22	0.011	25.287	0.176	6.544	0.016	0.131	0	0.013	100.133	TH1611B2	47 / 1 .
7.555	60.136	0	25.69	0.224	6.89	0.005	0.131	0	0	100.63	TH1611B2	48 / 1 .
7.61	59.578	0.003	25.614	0.125	6.805	0	0.105	0	0	99.839	TH1611B2	49 / 1 .
7.323	59.074	0.006	26.002	0.196	7.381	0.024	0.178	0.011	0	100.193	TH1611B2	50 / 1 .
7.194	59.165	0.016	26.032	0.195	7.221	0	0.338	0.002	0	100.162	TH1611B2	59 / 1 .
8.006	61.048	0.019	24.987	0.18	5.923	0.018	0.4	0.009	0	100.591	TH1611B2	60 / 1 .
7.308	59.382	0.003	26.027	0.098	7.133	0.006	0.22	0	0	100.177	TH1611B2	9 / 1 .
8.969	62.8	0	23.721	0.233	4.406	0	0.081	0.003	0.032	100.244	TH1612C1	67 / 1 .
9	63.634	0.009	23.366	0.247	4.247	0.004	0.034	0	0.018	100.559	TH1612C1	68 / 1 .
9.229	63.65	0	23.338	0.226	4.023	0.033	0.287	0.008	0	100.794	TH1612C1	69 / 1 .
9.273	64.067	0	22.953	0.23	3.7	0	0.234	0	0	100.456	TH1612C1	70 / 1 .
8.767	62.739	0	23.613	0.302	4.426	0.026	0.038	0	0.026	99.937	TH1612C1	75 / 1 .
8.816	62.548	0	23.551	0.298	4.497	0.028	0.013	0.012	0	99.762	TH1612C1	76 / 1 .
8.947	63.138	0	23.243	0.287	4.505	0	0.057	0	0.027	100.204	TH1612C1	77 / 1 .
8.946	63.24	0	23.41	0.236	4.354	0.003	0.043	0.015	0	100.247	TH1612C1	78 / 1 .
9.055	63.024	0.006	23.327	0.206	4.198	0	0.039	0.011	0.021	99.887	TH1612C1	95 / 1 .
9.001	63.55	0	23.318	0.175	4.191	0	0.034	0.002	0	100.271	TH1612C1	96 / 1 .
8.979	63.044	0.006	23.463	0.281	4.268	0.019	0.05	0.006	0	100.116	TH1612C1	97 / 1 .

Na2O	SiO2	MgO	Al2O3	K2O	CaO	TiO2	FeO	MnO	BaO	Total	Sample	DataSet/Point
9.022	62.954	0.009	23.282	0.221	4.36	0.01	0.01	0	0	99.867	TH1612C1	98 / 1 .
11.261	68.016	0.008	20.108	0.097	0.371	0.021	0	0	0	99.883	TH1612C2	105 / 1 .
8.825	62.939	0.023	23.599	0.296	4.302	0.002	0	0	0.031	100.017	TH1612C2	106 / 1 .
8.957	62.666	0.028	23.62	0.195	4.363	0	0.002	0.01	0.01	99.851	TH1612C2	107 / 1 .
9.716	64.904	0.002	22.407	0.707	1.942	0.026	0.028	0.01	0.014	99.757	TH1612C2	108 / 1 .
10.753	67.071	0.017	20.823	0.086	1.228	0.003	0.019	0	0	100	TH1612C2	109 / 1 .
10.152	64.835	0.018	22.06	0.151	2.532	0	0.023	0	0	99.771	TH1612C2	110 / 1 .
8.868	62.986	0.002	23.504	0.31	4.313	0	0.076	0	0.009	100.068	TH1612C2	57 / 1 .
9.086	63.159	0	23.322	0.199	4.274	0.025	0.023	0	0	100.089	TH1612C2	58 / 1 .
8.875	63.178	0	23.372	0.257	4.176	0.02	0.068	0.005	0.013	99.963	TH1612C2	59 / 1 .
9.082	63.23	0	23.307	0.187	4.13	0	0.334	0.009	0	100.28	TH1612C2	60 / 1 .
9.055	63.078	0.009	23.393	0.228	4.065	0	0.282	0.024	0.024	100.159	TH1612C2	61 / 1 .
8.942	62.992	0	23.608	0.266	4.321	0.015	0.174	0	0.018	100.337	TH1612C2	62 / 1 .
8.964	62.902	0	23.456	0.263	4.388	0	0.053	0.005	0.021	100.052	TH1612C2	71 / 1 .
9.089	63.474	0.013	23.198	0.249	4.124	0.001	0.097	0.001	0.008	100.255	TH1612C2	72 / 1 .
9.231	63.477	0	23.324	0.133	4.071	0	0.184	0.006	0	100.425	TH1612C2	73 / 1 .
9.188	63.544	0	23.264	0.169	4.16	0.009	0.072	0	0	100.407	TH1612C2	74 / 1 .
9.023	63.473	0	23.115	0.224	4.061	0.008	0.21	0	0	100.114	TH1612C2	75 / 1 .
9.035	62.852	0.007	23.482	0.209	4.296	0.004	0.189	0.003	0.02	100.096	TH1612C2	76 / 1 .
8.898	62.812	0.008	23.358	0.239	4.255	0.016	0.051	0.008	0.015	99.661	TH1612C2	77 / 1 .
8.781	62.865	0	23.568	0.334	4.412	0	0.012	0.002	0.009	99.982	TH1612C2	81 / 1 .
9.091	63.196	0	23.354	0.197	4.127	0.02	0.143	0	0.008	100.137	TH1612C2	82 / 1 .
9.064	63.123	0	23.161	0.299	4.101	0.006	0.036	0	0.024	99.815	TH1612C2	83 / 1 .
8.914	63.037	0.015	23.566	0.242	4.405	0	0.006	0	0	100.184	TH1612C2	84 / 1 .
8.899	62.652	0	23.623	0.222	4.42	0.016	0.057	0.002	0.015	99.905	TH1612C2	88 / 1 .
8.751	62.634	0.002	23.681	0.256	4.683	0.03	0.012	0	0.017	100.066	TH1612C2	89 / 1 .

Table B.3.: EMPA measurements of plagioclase

Na2O	SiO2	MgO	Al2O3	K2O	CaO	TiO2	FeO	MnO	BaO	Total	Sample	DataSet/Point
0.6	64.326	0	18.717	15.881	0	0.038	0.364	0	0.307	100.234	TH1608A1	10 / 1 .
0.815	64.539	0.007	18.743	15.483	0.024	0.019	0	0	0.289	99.919	TH1608A1	14 / 1 .
0.921	64.844	0.012	18.756	15.403	0.023	0.002	0.013	0.002	0.228	100.204	TH1608A1	15 / 1 .
0.762	64.645	0.02	18.627	15.673	0.012	0	0.005	0	0.215	99.96	TH1608A1	16 / 1 .
0.771	64.334	0.007	18.819	15.696	0	0.014	0.024	0.006	0.205	99.877	TH1608A1	20 / 1 .
0.959	64.185	0	18.776	15.272	0.014	0.017	0.006	0	0.304	99.534	TH1608A1	22 / 1 .
0.889	64.25	0	18.8	15.422	0.022	0	0.006	0.001	0.254	99.644	TH1608A1	23 / 1 .
0.846	64.445	0	18.877	15.588	0.013	0	0.058	0.012	0.345	100.183	TH1608A1	27 / 1 .
0.751	64.239	0	18.715	15.476	0.067	0.008	0.036	0	0.488	99.782	TH1608A1	36 / 1 .
1.131	64.125	0	18.747	15.016	0.107	0	0.014	0.002	0.306	99.448	TH1608A1	37 / 1 .
1.065	64.404	0	18.788	15.233	0.023	0.021	0.081	0	0.29	99.906	TH1608A1	38 / 1 .
0.938	64.178	0	18.735	15.281	0.013	0.027	0.363	0.012	0.344	99.892	TH1608A1	39 / 1 .
0.867	64.608	0.018	18.831	15.484	0.011	0.007	0.178	0	0.249	100.253	TH1608A1	6 / 1 .
0.759	64.414	0.003	18.803	15.685	0.003	0.03	0.281	0	0.312	100.292	TH1608A1	7 / 1 .
0.526	64.355	0	18.71	16.045	0.023	0	0.115	0	0.317	100.092	TH1608A1	8 / 1 .
0.698	64.827	0	18.841	15.859	0	0.048	0.213	0.001	0.298	100.787	TH1608A1	9 / 1 .
1.106	64.203	0.003	18.868	15.289	0.007	0	0.022	0.002	0.335	99.836	TH1608A2	100 / 1 .
1.083	64.069	0.003	18.845	15.179	0.029	0.003	0.118	0	0.293	99.622	TH1608A2	110 / 1 .
1.16	64.498	0.015	18.87	15.103	0.014	0	0.008	0	0.201	99.869	TH1608A2	111 / 1 .
0.599	64.322	0.019	18.784	15.977	0	0.021	0	0.005	0.31	100.036	TH1608A2	112 / 1 .
0.921	64.597	0.007	18.826	15.485	0	0.016	0.012	0.001	0.273	100.137	TH1608A2	113 / 1 .
1.282	64.314	0	18.865	14.936	0.052	0	0.046	0	0.287	99.781	TH1608A2	116 / 1 .
1.401	64.36	0.009	18.878	14.846	0.029	0.014	0.019	0	0.275	99.832	TH1608A2	117 / 1 .
1.203	64.379	0.003	18.871	14.988	0.012	0.011	0.06	0.014	0.319	99.861	TH1608A2	118 / 1 .
0.922	64.237	0.007	18.771	15.498	0	0.025	0.185	0	0.298	99.941	TH1608A2	119 / 1 .
0.209	64.485	0.002	18.465	16.278	0	0	0.216	0.009	0.2	99.865	TH1608A2	120 / 1 .
0.149	63.976	0.003	18.544	16.278	0	0.029	0.289	0	0.313	99.58	TH1608A2	121 / 1 .
1.581	64.363	0.001	18.935	14.436	0	0.024	0.013	0.006	0.263	99.623	TH1608A2	132 / 1 .
1.375	64.694	0.003	18.85	14.977	0	0.015	0	0.007	0.195	100.116	TH1608A2	133 / 1 .
1.219	64.495	0	18.823	15.047	0.019	0.001	0.008	0	0.252	99.863	TH1608A2	134 / 1 .

Na2O	SiO2	MgO	Al2O3	K2O	CaO	TiO2	FeO	MnO	BaO	Total	Sample	DataSet/Point
1.164	64.138	0.007	18.73	15.231	0.007	0	0.002	0.003	0.308	99.591	TH1608A2	136 / 1 .
1.152	64.466	0	18.753	15.102	0.022	0	0.007	0	0.216	99.718	TH1608A2	137 / 1 .
1.083	64.679	0.024	18.822	15.199	0.013	0.01	0.017	0	0.211	100.06	TH1608A2	138 / 1 .
0.745	63.893	0.016	18.737	15.623	0.002	0.035	0.111	0.003	0.35	99.515	TH1608A2	156 / 1 .
0.97	64.263	0	18.768	15.315	0	0.01	0.048	0	0.233	99.607	TH1608A2	157 / 1 .
0.328	63.814	0	18.61	16.259	0	0.033	0.118	0	0.343	99.505	TH1608A2	158 / 1 .
1.141	64.336	0	18.868	15.047	0.028	0	0.078	0	0.208	99.706	TH1608A2	99 / 1 .
0.82	63.957	0.011	18.91	15.576	0	0.005	0.019	0.001	0.611	99.91	TH1611B2	22 / 1 .
0.401	63.978	0	18.78	16.142	0	0	0.019	0	0.517	99.838	TH1611B2	23 / 1 .
0.505	63.803	0.005	18.744	15.931	0	0.002	0.172	0.012	0.656	99.831	TH1611B2	34 / 1 .
0.394	64.153	0.012	18.928	16.111	0	0.025	0.104	0	0.667	100.393	TH1611B2	35 / 1 .
0.292	63.704	0.006	18.768	16.118	0.099	0	0.351	0.006	0.559	99.904	TH1611B2	56 / 1 .
0.734	63.829	0	18.865	15.566	0.028	0	0.242	0	0.516	99.78	TH1611B2	57 / 1 .
0.358	63.506	0	18.769	16.131	0.038	0.019	0.22	0.003	0.706	99.75	TH1611B2	58 / 1 .
0.517	64.172	0	18.787	15.967	0	0.01	0.419	0.006	0.593	100.472	TH1611B2	m1 / 1 .
0.925	64.25	0	18.816	15.376	0.005	0.005	0.104	0	0.53	100.01	TH1612C1	71 / 1 .
0.938	63.837	0.012	18.907	15.132	0.031	0	0.067	0	0.855	99.779	TH1612C1	72 / 1 .
0.818	63.912	0.01	18.894	15.49	0.01	0	0.16	0.003	0.495	99.793	TH1612C1	73 / 1 .
0.878	64.323	0	18.993	15.539	0.007	0	0.382	0	0.39	100.513	TH1612C1	74 / 1 .
1.353	64.451	0	19.083	14.81	0.038	0	0.006	0	0.396	100.137	TH1612C1	79 / 1 .
1.387	64.654	0	18.985	14.819	0.035	0	0.029	0	0.389	100.298	TH1612C1	80 / 1 .
1.37	64.46	0	19.063	14.504	0.028	0.007	0.014	0	0.36	99.807	TH1612C1	81 / 1 .
1.29	64.379	0	18.994	14.835	0.036	0	0	0.007	0.314	99.855	TH1612C1	82 / 1 .
1.304	64.159	0	19	14.806	0.029	0.002	0.217	0.002	0.355	99.874	TH1612C1	91 / 1 .
1.113	64.466	0	18.862	15.203	0.001	0.002	0.056	0	0.371	100.076	TH1612C1	92 / 1 .
1.259	64.591	0	18.908	14.94	0.019	0.017	0.091	0	0.315	100.139	TH1612C1	93 / 1 .
0.907	64.364	0.008	18.822	15.231	0.006	0.028	0.299	0	0.455	100.119	TH1612C1	94 / 1 .
1.552	64.621	0	18.938	14.485	0.048	0.023	0.025	0.016	0.373	100.079	TH1612C2	100 / 1 .
0.912	64.293	0	18.905	15.454	0.049	0.011	0.03	0	0.245	99.899	TH1612C2	101 / 1 .
1.033	64.126	0.004	18.861	15.337	0.004	0.016	0.018	0	0.306	99.704	TH1612C2	102 / 1 .

Na2O	SiO2	MgO	Al2O3	K2O	CaO	TiO2	FeO	MnO	BaO	Total	Sample	DataSet/Point
1.546	64.236	0.019	18.976	14.406	0.042	0	0.02	0.004	0.352	99.601	TH1612C2	103 / 1 .
0.855	64.017	0	18.849	15.447	0.025	0.006	0.003	0.006	0.246	99.453	TH1612C2	104 / 1 .
1.268	64.189	0.017	18.924	14.84	0.032	0.007	0.017	0.001	0.46	99.755	TH1612C2	78 / 1 .
1.112	64.056	0	18.819	15.124	0.009	0	0.052	0	0.281	99.453	TH1612C2	79 / 1 .
0.762	64.065	0.043	18.796	15.498	0.011	0.024	0.476	0	0.488	100.162	TH1612C2	80 / 1 .
1.179	63.879	0.001	18.883	15.122	0.001	0	0.396	0	0.394	99.853	TH1612C2	85 / 1 .
1.078	63.835	0.002	18.947	15.135	0.019	0	0.118	0.005	0.463	99.602	TH1612C2	86 / 1 .
0.976	64.307	0.01	18.758	15.189	0.004	0.019	0.04	0	0.438	99.741	TH1612C2	87 / 1 .

Table B.4.: EMPA measurements of K-feldspar

Na2O	SiO2	MgO	Al2O3	K2O	CaO	TiO2	FeO	Cl	MnO	Total	Sample	DataSet/Point
0.046	35.624	5.961	16.784	9.131	0.079	2.578	23.439	0.087	0.302	94.031	TH1608A1	1 / 1 .
0.033	35.472	5.925	16.704	8.966	0.079	2.486	24.037	0.078	0.282	94.063	TH1608A1	2 / 1 .
0.065	35.38	5.988	16.945	8.876	0.119	2.512	23.396	0.082	0.327	93.689	TH1608A1	3 / 1 .
0.077	35.336	6.174	17.805	9.203	0.062	2.534	22.551	0.082	0.256	94.08	TH1608A1	30 / 1 .
0.076	34.937	6.34	18.177	9.488	0.03	2.318	23.426	0.078	0.243	95.112	TH1608A1	31 / 1 .
0.081	34.798	5.841	18.082	9.239	0.06	2.51	23.106	0.077	0.274	94.067	TH1608A1	32 / 1 .
0.066	35.333	6.024	17.677	9.407	0.043	2.576	23.062	0.074	0.279	94.542	TH1608A1	33 / 1 .
0.07	35.314	6.158	17.511	9.213	0.061	2.817	22.393	0.07	0.279	93.887	TH1608A1	34 / 1 .
0.055	35.811	5.934	17.026	9.177	0.089	2.521	23.344	0.088	0.304	94.35	TH1608A1	4 / 1 .
0.073	34.975	5.523	17.746	9.464	0.05	3.015	23.179	0.068	0.303	94.397	TH1608A1	46 / 1 .
0.088	35.038	5.999	17.74	9.468	0.048	2.684	23.603	0.085	0.294	95.045	TH1608A1	47 / 1 .
0.06	35.048	5.931	18.408	9.565	0.014	3.177	23.035	0.079	0.285	95.603	TH1608A1	48 / 1 .
0.072	34.704	5.839	18.24	9.509	0.022	2.784	23.446	0.077	0.297	94.989	TH1608A1	49 / 1 .
0.061	35.241	5.721	17.116	9.003	0.129	2.53	23.518	0.088	0.347	93.752	TH1608A1	5 / 1 .
0.051	34.962	6.119	17.891	9.62	0.019	2.922	23.269	0.076	0.325	95.254	TH1608A1	50 / 1 .
0.067	35.441	6.08	17.617	9.262	0.067	2.636	22.942	0.083	0.263	94.457	TH1608A2	103 / 1 .
0.068	35.108	5.965	18.298	9.756	0	2.793	22.977	0.08	0.283	95.329	TH1608A2	104 / 1 .

Na2O	SiO2	MgO	Al2O3	K2O	CaO	TiO2	FeO	Cl	MnO	Total	Sample	DataSet/Point
0.072	35.546	5.77	17.507	9.251	0.085	2.462	23.554	0.088	0.22	94.554	TH1608A2	108 / 1 .
0.045	35.69	5.846	17.943	8.98	0.023	2.752	22.383	0.075	0.266	94.002	TH1608A2	109 / 1 .
0.094	35.275	5.871	18.048	9.614	0	3.035	23.527	0.082	0.35	95.896	TH1608A2	122 / 1 .
0.088	35.22	5.841	18.108	9.479	0.003	2.942	23.836	0.087	0.34	95.944	TH1608A2	123 / 1 .
0.084	35.199	5.744	17.998	9.508	0.024	3.003	23.553	0.1	0.373	95.585	TH1608A2	126 / 1 .
0.101	35.039	5.748	18.29	9.571	0	3.078	22.952	0.061	0.364	95.205	TH1608A2	127 / 1 .
0.095	34.845	5.714	18.229	9.615	0.009	3.183	23.273	0.073	0.336	95.373	TH1608A2	128 / 1 .
0.092	34.952	5.901	18.278	9.456	0.001	3.157	23.111	0.076	0.344	95.369	TH1608A2	129 / 1 .
0.074	35.282	5.622	18.462	9.695	0.006	3.235	22.568	0.079	0.324	95.346	TH1608A2	130 / 1 .
0.084	35.348	5.615	18.432	9.569	0	3.135	23.044	0.068	0.296	95.591	TH1608A2	131 / 1 .
0.053	35.681	6.256	16.85	9.14	0.045	2.305	23.08	0.082	0.262	93.754	TH1608A2	143 / 1 .
0.054	35.513	5.912	17.495	9.089	0.046	2.797	22.365	0.074	0.261	93.606	TH1608A2	144 / 1 .
0.056	34.903	5.922	17.241	9.398	0	2.493	24.434	0.099	0.307	94.854	TH1608A2	145 / 1 .
0.031	34.531	5.923	17.575	9.541	0.004	2.472	24.363	0.076	0.334	94.851	TH1608A2	146 / 1 .
0.038	35.504	6.351	17.206	9.07	0.077	1.206	23.667	0.105	0.291	93.515	TH1608A2	147 / 1 .
0.036	35.448	6.201	17.476	9.606	0.003	2.978	23.252	0.08	0.331	95.412	TH1608A2	148 / 1 .
0.082	35.162	5.385	18.057	9.588	0.001	3.618	23.199	0.078	0.308	95.478	TH1608A2	149 / 1 .
0.068	36.12	9.706	16.279	9.722	0.027	2.164	20.706	0.026	0.403	95.221	TH1611B2	1 / 1 .
0.042	36.161	10.393	16.055	9.851	0.075	1.557	20.242		0.381	94.793	TH1611B2	11 / 1 .
0.083	35.397	9.309	15.776	9.583	0.029	2.524	21.548	0.033	0.414	94.697	TH1611B2	14 / 1 .
0.079	35.93	9.687	15.267	9.416	0.019	2.642	21.252	0.028	0.428	94.749	TH1611B2	15 / 1 .
0.08	36.748	9.332	16	9.506	0.041	2.489	20.847	0.036	0.41	95.488	TH1611B2	16 / 1 .
0.083	35.846	9.619	15.338	9.567	0.015	2.348	20.986	0.035	0.383	94.219	TH1611B2	17 / 1 .
0.09	36.539	9.812	15.995	9.619	0.027	2.641	20.077	0.024	0.383	95.206	TH1611B2	21 / 1 .
0.097	35.695	9.181	15.167	9.459	0.033	2.751	22.331	0.02	0.451	95.184	TH1611B2	24 / 1 .
0.09	35.961	10.237	16.253	9.591	0.031	1.718	20.442	0.035	0.384	94.742	TH1611B2	3 / 1 .
0.063	35.993	10.174	16.118	9.697	0.021	1.107	20.892	0.032	0.397	94.494	TH1611B2	39 / 1 .
0.05	36.264	10.11	16.064	9.615	0.018	1.483	20.444	0.026	0.404	94.476	TH1611B2	4 / 1 .
0.085	35.741	9.85	15.806	9.503	0.047	1.505	21.316	0.031	0.449	94.332	TH1611B2	41 / 1 .
0.065	35.809	9.616	16.195	9.577	0.029	2.214	20.433	0.036	0.407	94.382	TH1611B2	5 / 1 .

Na2O	SiO2	MgO	Al2O3	K2O	CaO	TiO2	FeO	Cl	MnO	Total	Sample	DataSet/Point
0.059	35.82	9.415	15.713	9.693	0.01	2.4	22.028	0.026	0.39	95.554	TH1611B2	53 / 1 .
0.054	35.596	9.31	15.494	9.554	0.066	2.217	21.562	0.023	0.392	94.269	TH1611B2	54 / 1 .
0.059	35.482	9.57	15.896	9.677	0.019	1.739	21.556	0.027	0.368	94.393	TH1611B2	55 / 1 .
0.086	36.11	9.948	15.806	9.593	0.07	2.296	20.682	0.032	0.395	95.018	TH1611B2	7 / 1 .
0.112	34.421	5.986	18.476	9.566	0	3.449	22.7	0.096	0.321	95.126	TH1612C1	63 / 1 .
0.08	34.971	6.688	18.128	9.657	0.015	2.284	23.249	0.085	0.345	95.502	TH1612C1	64 / 1 .
0.063	34.788	6.149	18.088	9.485	0	3.317	23.419	0.111	0.356	95.777	TH1612C1	65 / 1 .
0.102	34.732	6.164	18.805	9.531	0.015	3.202	22.279	0.082	0.306	95.218	TH1612C1	66 / 1 .
0.125	34.497	5.743	18.403	9.448	0.016	3.387	22.82	0.088	0.511	95.039	TH1612C1	83 / 1 .
0.181	34.779	5.932	18.561	9.38	0.015	3.442	21.878	0.095	0.388	94.651	TH1612C1	84 / 1 .
0.185	34.701	6.222	18.622	9.29	0.03	3.014	21.864	0.089	0.355	94.373	TH1612C1	85 / 1 .
0.144	34.535	6.429	17.315	9.407	0.059	3.314	23.449	0.083	0.356	95.09	TH1612C1	86 / 1 .
0.126	35.147	6.442	19.662	9.298	0.038	2.157	21.117	0.087	0.367	94.442	TH1612C1	87 / 1 .
0.063	35.169	6.797	18.65	9.617	0	2.47	22.194	0.081	0.392	95.433	TH1612C1	88 / 1 .
0.053	34.789	6.672	17.971	9.555	0.004	2.122	23.83	0.102	0.398	95.496	TH1612C1	89 / 1 .
0.093	34.868	6.394	18.525	9.55	0.014	2.11	23.004	0.105	0.408	95.072	TH1612C1	90 / 1 .
0.117	34.188	6.23	18.001	9.478	0.004	3.043	23.492	0.102	0.368	95.023	TH1612C2	51 / 1 .
0.119	34.33	6.569	17.845	9.418	0.003	2.509	23.765	0.101	0.389	95.047	TH1612C2	52 / 1 .
0.097	34.505	6.738	17.516	9.568	0.081	2.471	23.664	0.103	0.403	95.146	TH1612C2	53 / 1 .
0.088	34.496	6.42	18.074	9.499	0.008	2.595	23.632	0.095	0.37	95.278	TH1612C2	54 / 1 .
0.107	34.503	6.392	18.528	9.597	0.011	2.74	22.807	0.082	0.386	95.154	TH1612C2	55 / 1 .
0.114	34.769	6.581	17.999	9.465	0	2.768	23.547	0.1	0.413	95.755	TH1612C2	56 / 1 .
0.131	34.378	6.04	18.339	9.371	0.025	3.319	22.737	0.116	0.375	94.83	TH1612C2	64 / 1 .
0.085	34.378	5.864	18.543	9.392	0.031	3.222	22.871	0.101	0.388	94.875	TH1612C2	65 / 1 .
0.112	34.555	6.016	17.937	9.428	0	2.59	24.11	0.092	0.436	95.276	TH1612C2	66 / 1 .
0.125	34.325	7.125	17.86	9.323	0.028	1.545	23.163	0.101	0.41	94.005	TH1612C2	67 / 1 .
0.104	34.675	5.82	18.753	9.521	0.016	3.508	22.123	0.103	0.361	94.982	TH1612C2	68 / 1 .
0.126	34.63	6.324	18.531	9.519	0.017	3.046	22.288	0.09	0.32	94.893	TH1612C2	69 / 1 .
0.093	34.921	6.232	18.649	9.596	0	3.228	21.97	0.089	0.381	95.16	TH1612C2	70 / 1 .
0.105	34.658	6.146	18.476	9.573	0	3.03	22.877	0.102	0.42	95.387	TH1612C2	90 / 1 .

Na2O	SiO2	MgO	Al2O3	K2O	CaO	TiO2	FeO	Cl	MnO	Total	Sample	DataSet/Point
0.086	34.822	5.752	17.901	9.582	0.014	3.611	23.429	0.102	0.391	95.691	TH1612C2	91 / 1 .
0.098	34.698	5.711	18.526	9.464	0.013	3.672	22.891	0.097	0.402	95.574	TH1612C2	92 / 1 .
0.095	34.341	5.85	18.308	9.548	0.016	3.445	23.197	0.107	0.404	95.312	TH1612C2	93 / 1 .
0.113	34.515	5.829	18.701	9.439	0.01	3.176	22.449	0.097	0.405	94.734	TH1612C2	94 / 1 .
0.123	36.512	7.544	18.169	6.878	0.049	0.128	20.592	0	0.193	90.189	TH1612C2	97 / 1 .

Table B.5.: EMPA measurements of biotite

Na2O	SiO2	MgO	Al2O3	K2O	CaO	TiO2	FeO	Cl	MnO	Total	Sample	DataSet/Point
0.381	45.796	1.001	33.839	10.883	0.022	0.663	2.014	0.003	0.041	94.644	TH1608A1	35 / 1 .
0.141	48.17	0.276	34.723	10.081	0.029	0.112	1.452	0.03	0.008	95.021	TH1608A1	m4 / 1 .
0.17	46.586	1.34	31.611	10.26	0.031	1.574	2.762	0.002	0.047	94.383	TH1608A2	105 / 1 .
0.184	46.896	1.487	31.119	10.493	0.021	1.363	2.95	0.003	0.072	94.588	TH1608A2	106 / 1 .
0.216	46.525	1.033	33.101	8.121	0.025	0.752	2.423	0.001	0.041	92.239	TH1608A2	107 / 1 .
0.286	46.19	1.267	31.973	10.355	0.034	1.514	2.378	0.009	0	94.006	TH1608A2	150 / 1 .
0.297	46.286	1.235	32.277	10.863	0.004	1.289	2.426	0.001	0.017	94.694	TH1608A2	151 / 1 .
0.3	46.112	1.11	33.373	10.421	0.024	0.988	2.143	0.005	0.039	94.514	TH1608A2	152 / 1 .
0.33	46.138	1.102	33.719	10.869	0.012	0.066	2.229	0.004	0.015	94.485	TH1608A2	159 / 1 .
0.373	45.781	0.774	34.228	10.712	0	1.058	1.876	0	0.011	94.813	TH1612C2	63 / 1 .
0.47	45.601	0.781	34.602	10.723	0.004	1.086	1.915	0	0	95.184	TH1612C2	95 / 1 .
0.319	45.938	0.737	34.804	10.798	0.013	0.889	1.621	0.007	0.03	95.157	TH1612C2	96 / 1 .
0.478	45.798	0.835	34.86	10.786	0	0.632	1.639	0	0.04	95.069	TH1612C2	98 / 1 .
0.453	45.828	0.709	34.844	10.668	0	0.863	1.556	0.001	0.001	94.921	TH1612C2	99 / 1 .

Table B.6.: EMPA measurements of white mica

Na2O	SiO2	MgO	Al2O3	K2O	CaO	TiO2	FeO	Cl	MnO	Cr2O3	Total	Sample	DataSet/Point
1.301	41.099	7.671	11.186	1.366	11.657	0.99	21.409	0.027	0.61		97.316	TH1611B2	18 / 1 .
1.26	40.992	7.521	11.688	1.445	11.774	0.797	21.523	0.029	0.614		97.644	TH1611B2	19 / 1 .

Na2O	SiO2	MgO	Al2O3	K2O	CaO	TiO2	FeO	Cl	MnO	Cr2O3	Total	Sample	DataSet/Point
1.178	41.283	7.783	11.272	1.367	11.781	0.75	21.191	0.027	0.63	0	97.264	TH1611B2	30 / 1 .
1.159	40.684	7.155	11.897	1.42	11.771	0.517	21.64	0.037	0.631	0.007	96.915	TH1611B2	31 / 1 .
1.213	41.651	7.888	11.38	1.276	11.801	0.575	21.271	0.025	0.602	0.009	97.689	TH1611B2	32 / 1 .
1.213	41.206	7.747	11.425	1.375	11.833	0.73	20.829	0.033	0.624	0.015	97.029	TH1611B2	33 / 1 .
1.213	41.188	7.594	11.619	1.328	11.748	0.61	21.334	0.031	0.628	0.001	97.294	TH1611B2	37 / 1 .
1.141	41.814	7.471	11.36	1.081	11.797	0.189	21.823	0.03	0.635	0.02	97.36	TH1611B2	38 / 1 .

Table B.7.: EMPA measurements of amphibole

Na2O	SiO2	MgO	Al2O3	K2O	CaO	TiO2	FeO	MnO	Cr2O3	Total	Sample	DataSet/Point
0.007	37.213	0	23.324	0.005	23.449	0.038	12.47	0.201		96.724	TH1611B2	12 / 1 .
0.006	37.532	0.026	23.484		23.158	0.204	11.806	0.336	0.009	96.56	TH1611B2	36 / 1 .
0	37.549	0.016	23.19	0	23.364	0.12	12.418	0.198	0.003	96.858	TH1611B2	51 / 1 .
0.004	37.51	0.01	23.62	0	23.594	0.095	12.147	0.18	0.007	97.168	TH1611B2	61 / 1 .
0.005	37.186	0.01	23.32	0	23.373	0.092	12.205	0.257	0.011	96.468	TH1611B2	62 / 1 .

Table B.8.: EMPA measurements of clinozoisite

Na2O	SiO2	MgO	Al2O3	K2O	CaO	TiO2	FeO	Cl	MnO	Total	Sample	DataSet/Point
0.156	34.723	13.053	17.331	0.731	0.205	0.12	19.214	0.014	0.088	85.635	TH1608A1	m1 / 1 .
0.176	32.605	12.229	18.204	0.997	0.296	0.206	19.576	0.012	0.123	84.424	TH1608A1	m2 / 1 .
0.14	32.217	10.156	18.893	2.534	0.069	0.085	22.264	0.005	0.201	86.565	TH1608A2	124 / 1 .
0.127	33.136	8.404	18.329	3.908	0.083	0.203	23.008	0.02	0.229	87.447	TH1608A2	125 / 1 .
0	26.396	14.374	19.121	0.025	0.051	0.1	26.465	0.004	0.659	87.197	TH1611B2	2 / 1 .
0	26.275	14.025	18.919	0.179	0.109	0.235	26.811	0.002	0.79	87.346	TH1611B2	20 / 1 .
0.018	26.153	14.072	19.475	0.121	0.084	0.043	26.707	0.001	0.753	87.426	TH1611B2	25 / 1 .
0.017	25.64	13.875	19.802	0.048	0.045	0.109	26.779	0.001	0.725	87.04	TH1611B2	26 / 1 .
0.012	25.568	13.35	19.891	0.026	0.056	0.068	27.695	0.006	0.687	87.358	TH1611B2	52 / 1 .
0.009	25.849	13.38	20.399	0.13	0.023	0.093	26.533	0.002	0.823	87.241	TH1611B2	6 / 1 .

Na2O	SiO2	MgO	Al2O3	K2O	CaO	TiO2	FeO	Cl	MnO	Total	Sample	DataSet/Point
0.012	26.401	14.298	19.324	0.027	0.042	0.08	26.739	0.008	0.781	87.712	TH1611B2	8 / 1 .

Table B.9.: EMPA measurements of chlorite

Na2O	SiO2	MgO	Al2O3	CaO	TiO2	FeO	MnO	Cr2O3	NiO	Total	Sample	DataSet/Point
0	30.149	0.022	1.902	28.464	36.617	1.311	0.108	0.021	0.029	98.622	TH1611B2	42 / 1 .
0.004	30.237	0	2.062	28.677	36.131	1.524	0.108	0.019	0.023	98.785	TH1611B2	43 / 1 .

Table B.10.: EMPA measurements of titanite

Na2O	SiO2	MgO	Al2O3	K2O	CaO	TiO2	FeO	MnO	Cr2O3	Total	Sample	DataSet/Point
0	0.233	0	0.008		56.436	0.024	0.342	0.058	0.002	57.102	TH1611B2	44 / 1 .

Table B.11.: EMPA measurements of calcite

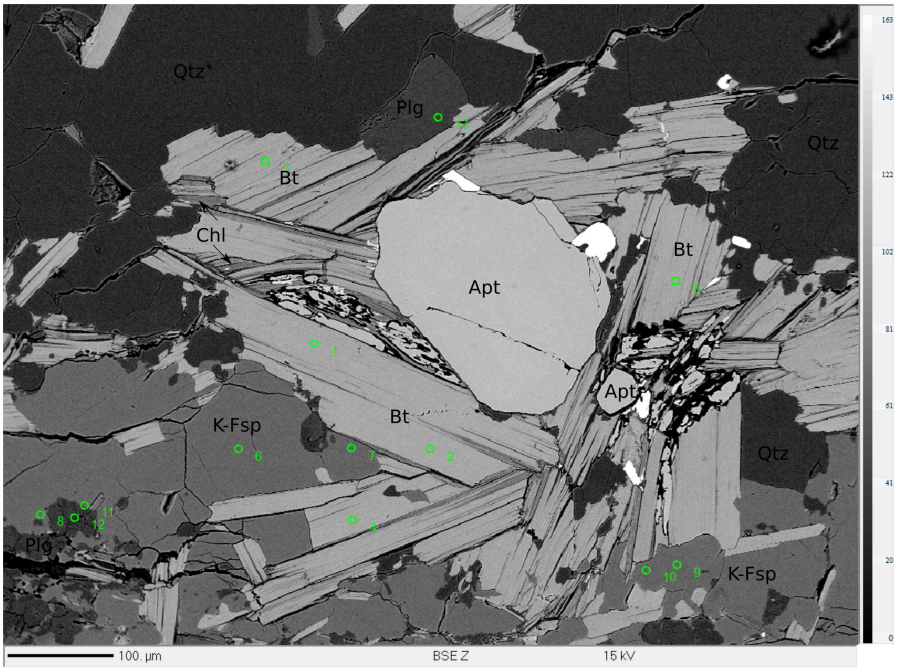

Figure B.1.: TH1608A1 A1

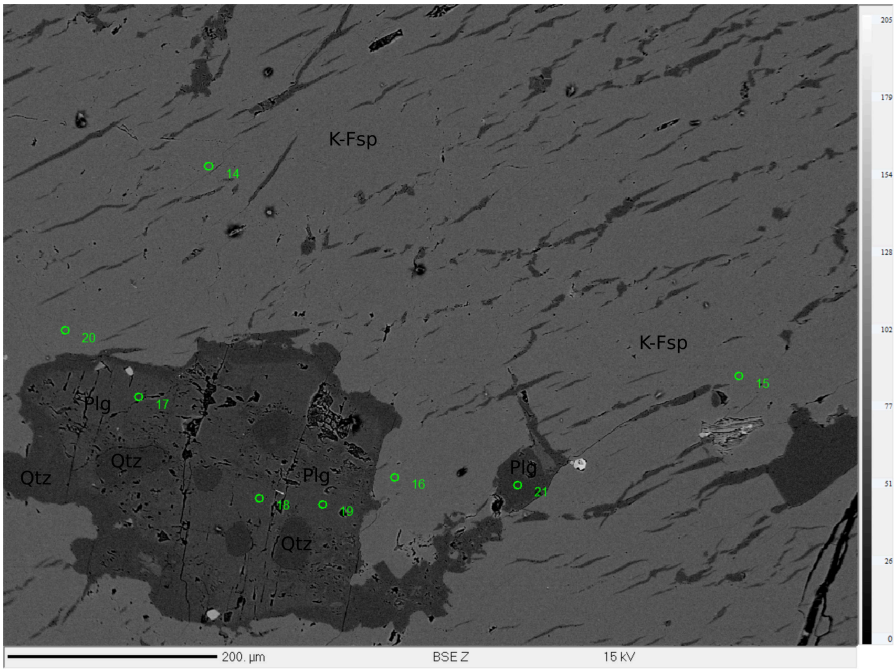

Figure B.2.: TH1608A1 A2

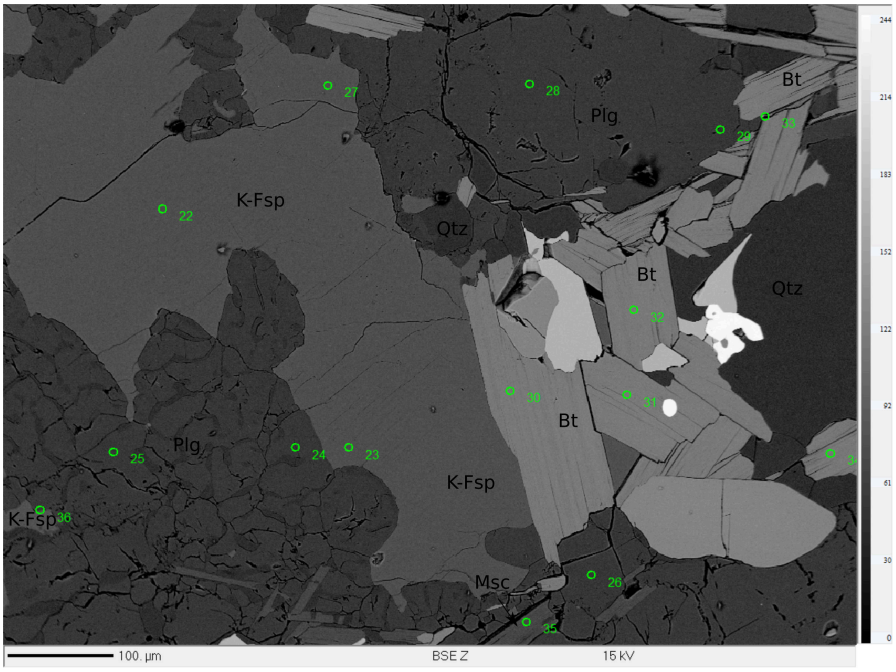

Figure B.3.: TH1608A1 A3

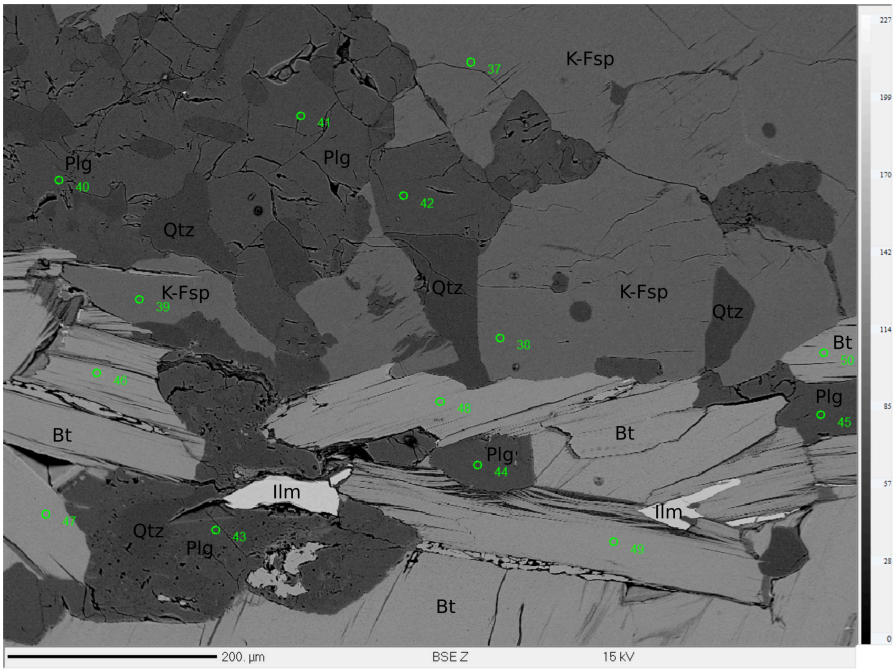

Figure B.4.: TH1608A1 A4

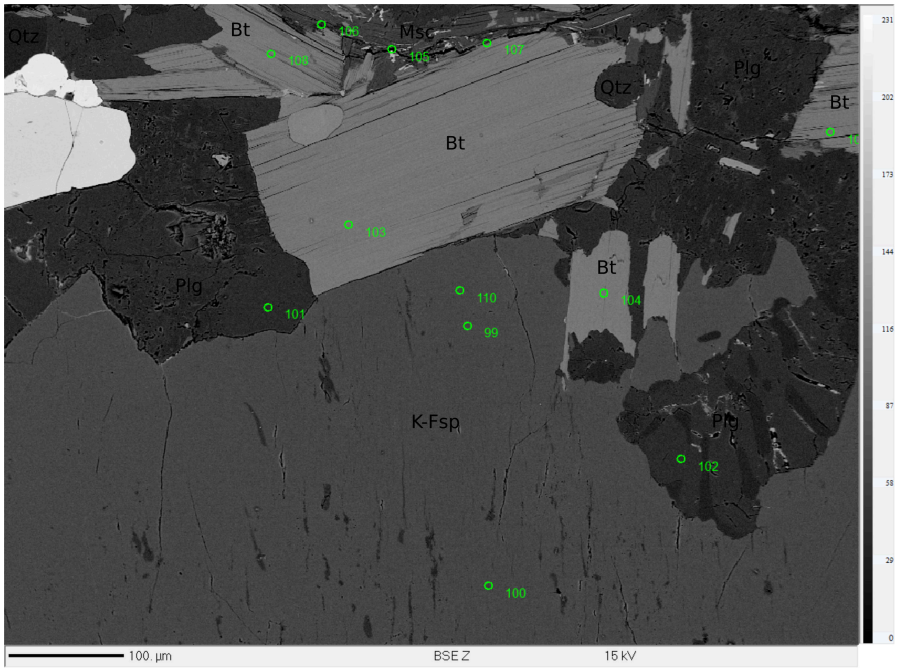

Figure B.5.: TH1608A2 A1

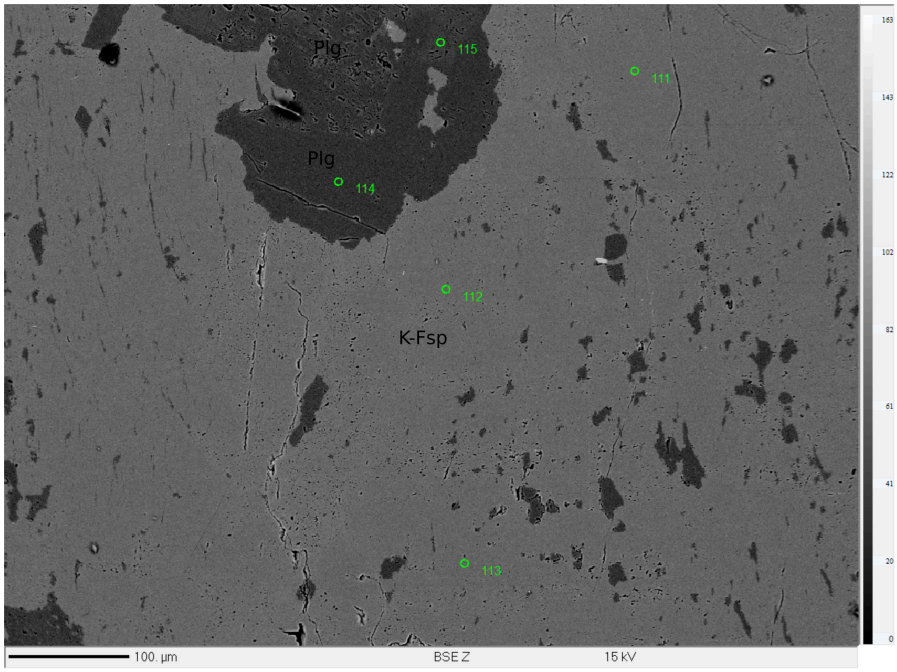

Figure B.6.: TH1608A2 A2

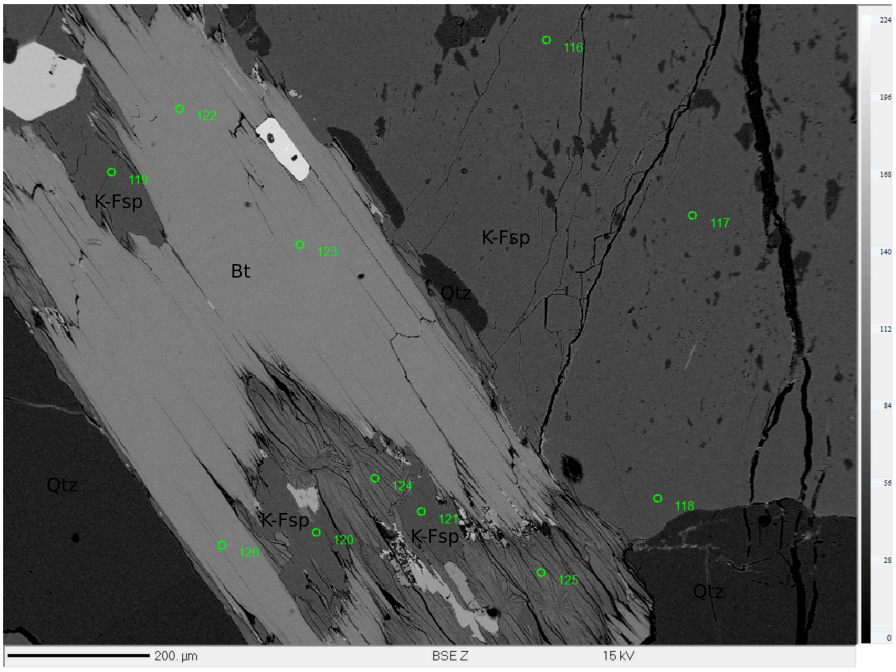

Figure B.7.: TH1608A2 A3

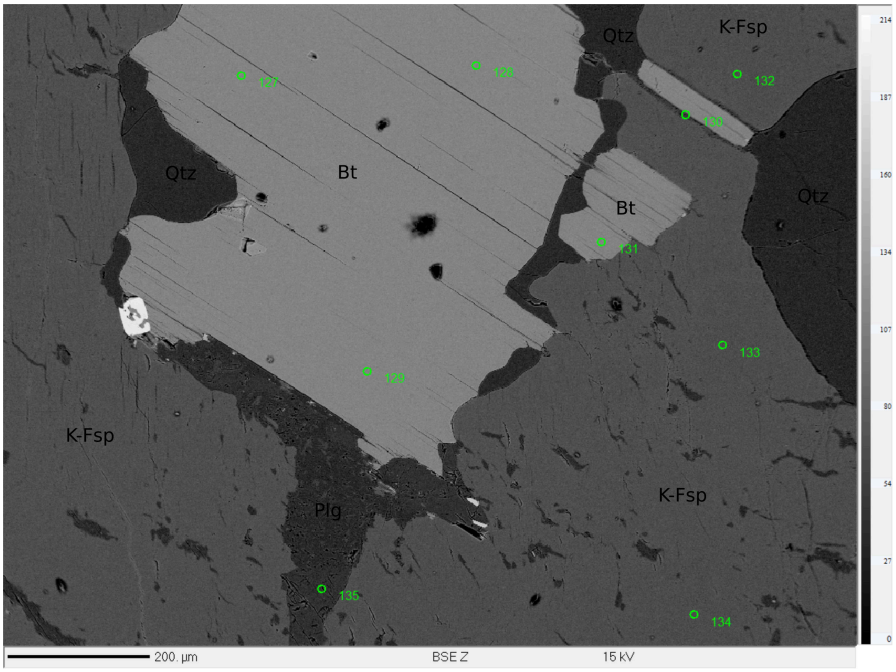

Figure B.8.: TH1608A2 A4

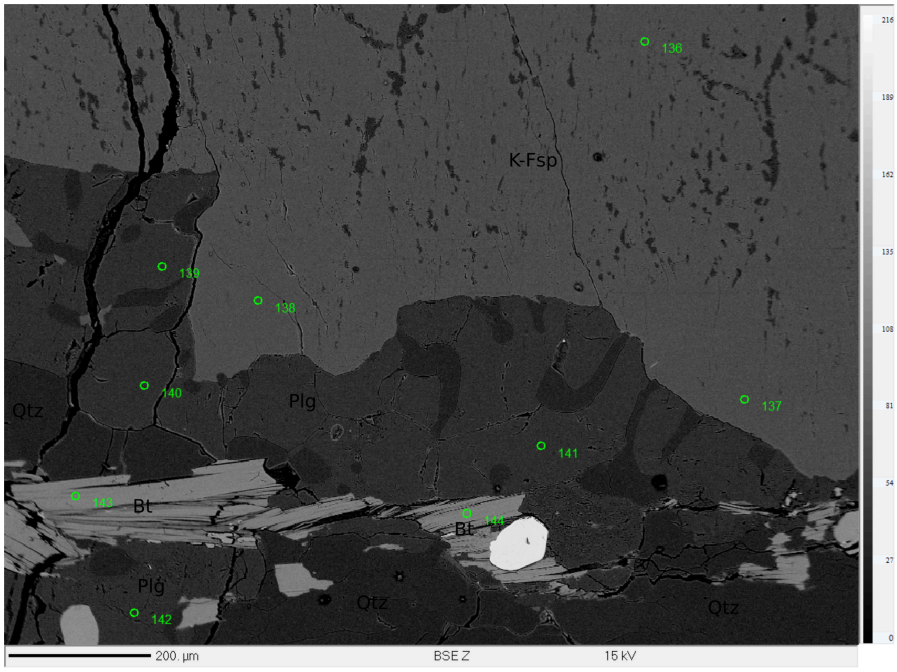

Figure B.9.: TH1608A2 A5

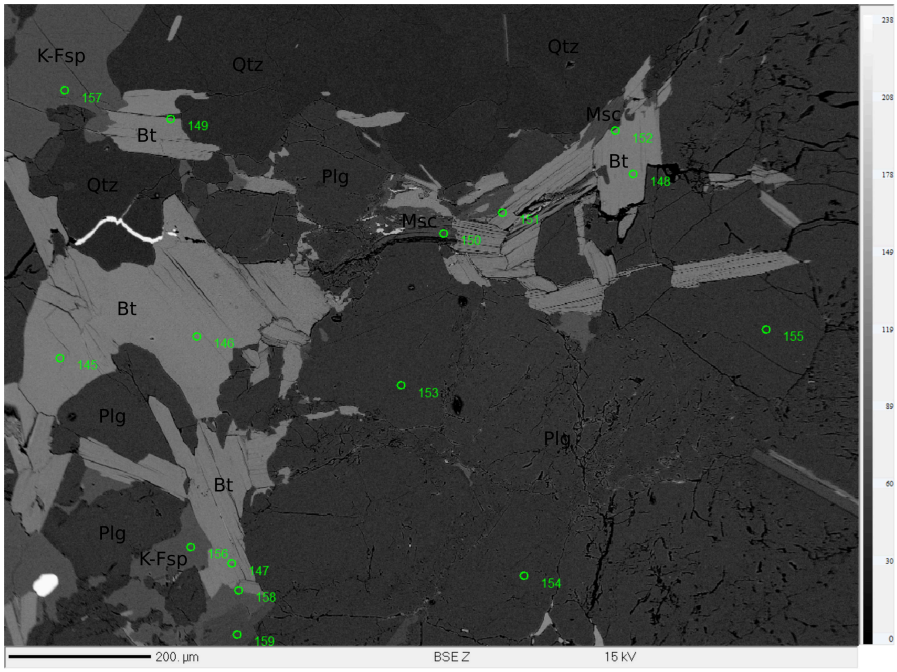

Figure B.10.: TH1608A2 A6

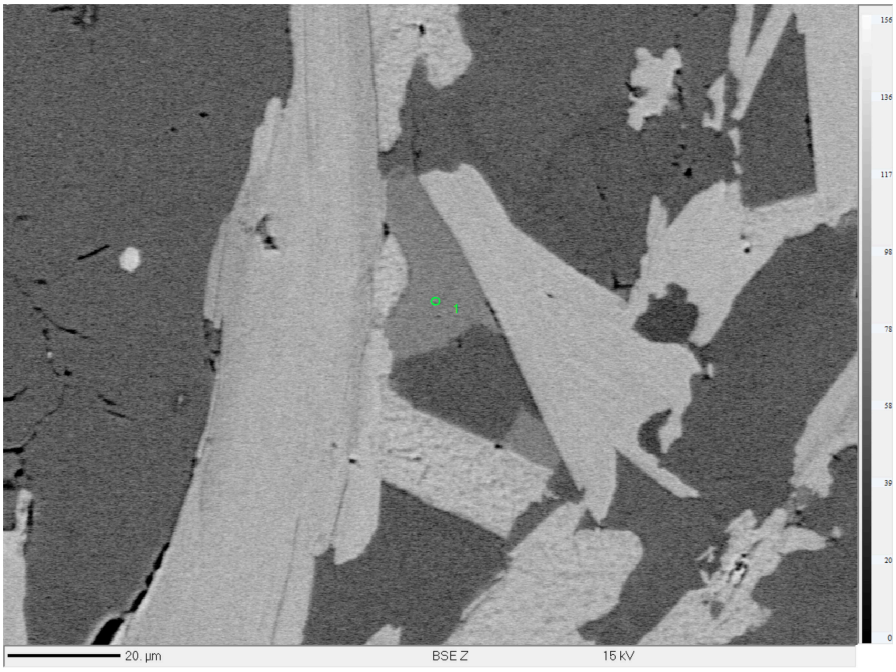

Figure B.11.: TH1611B2 A1

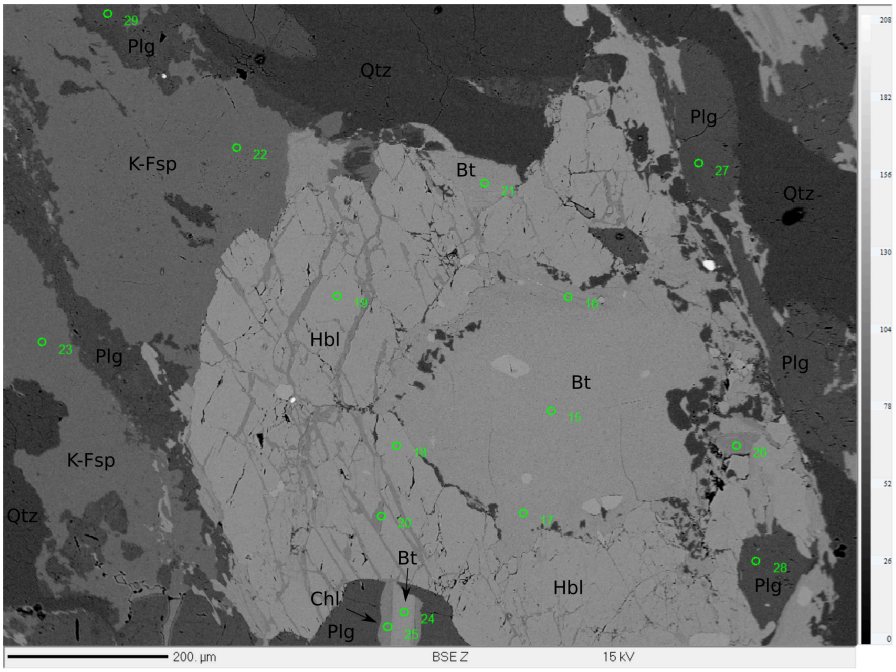

Figure B.12.: TH1611B2 A2

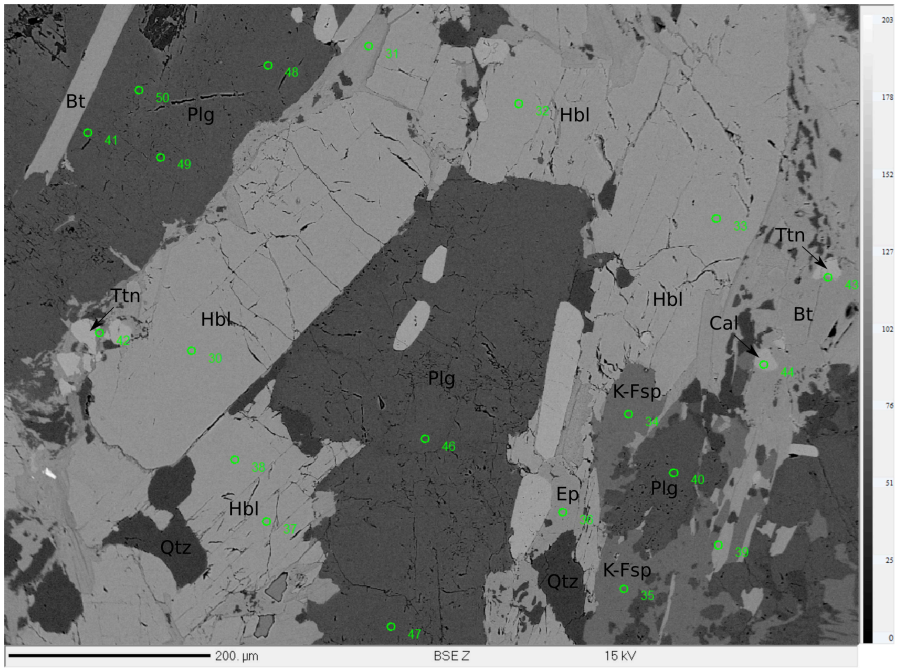

Figure B.13.: TH1611B2 A3

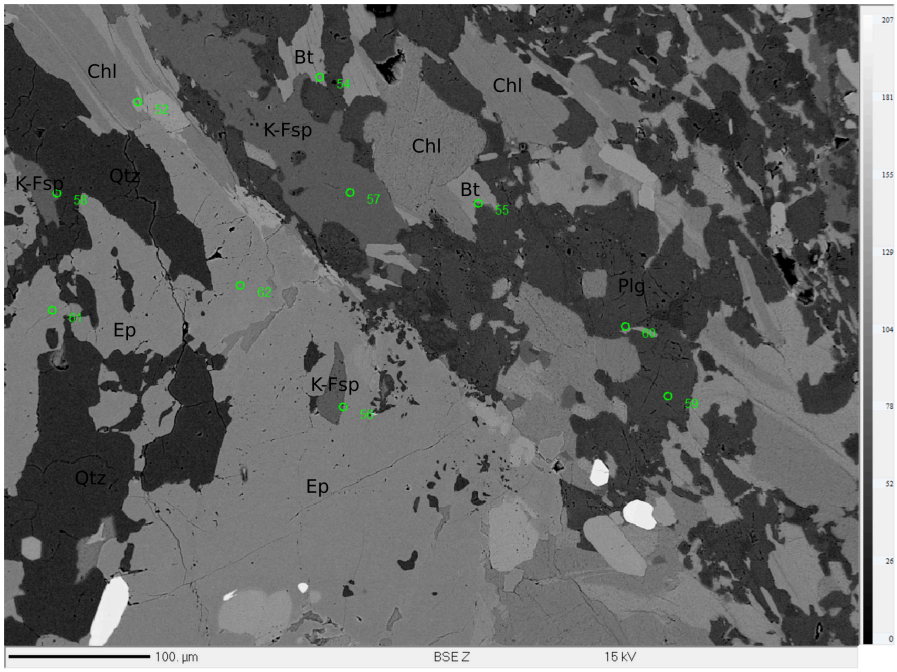

Figure B.14.: TH1611B2 A4

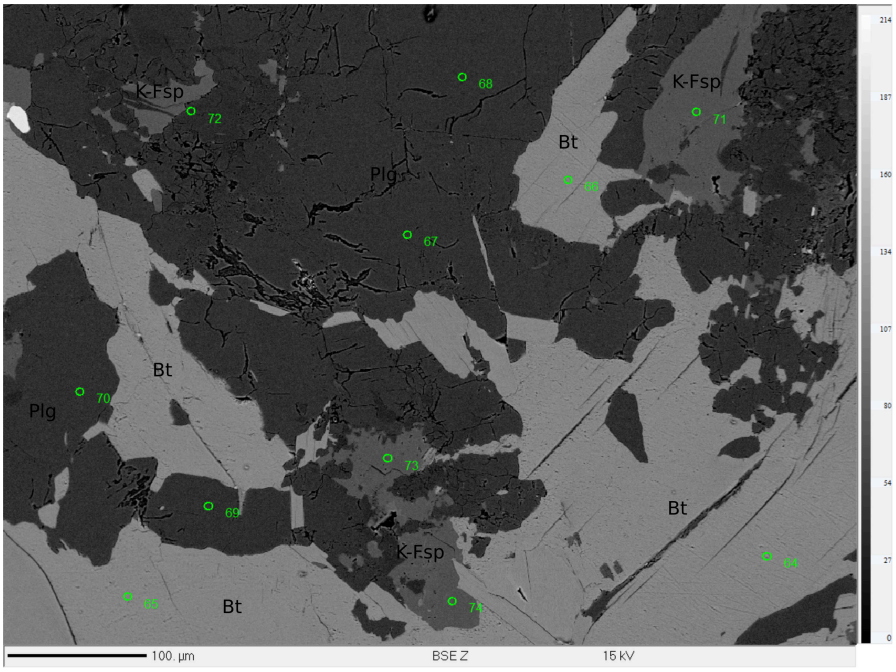

Figure B.15.: TH1612C1 A1

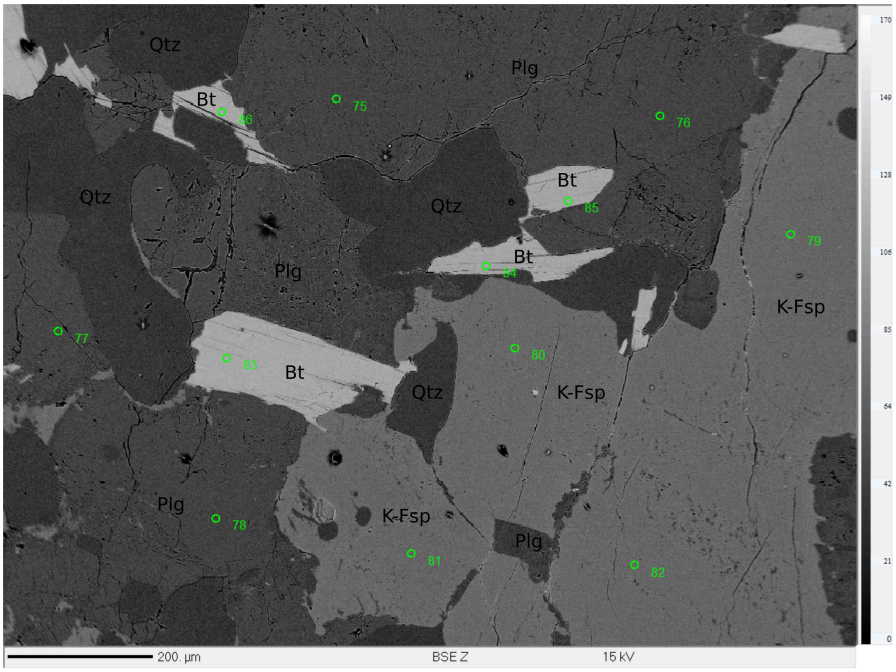

Figure B.16.: TH1612C1 A2

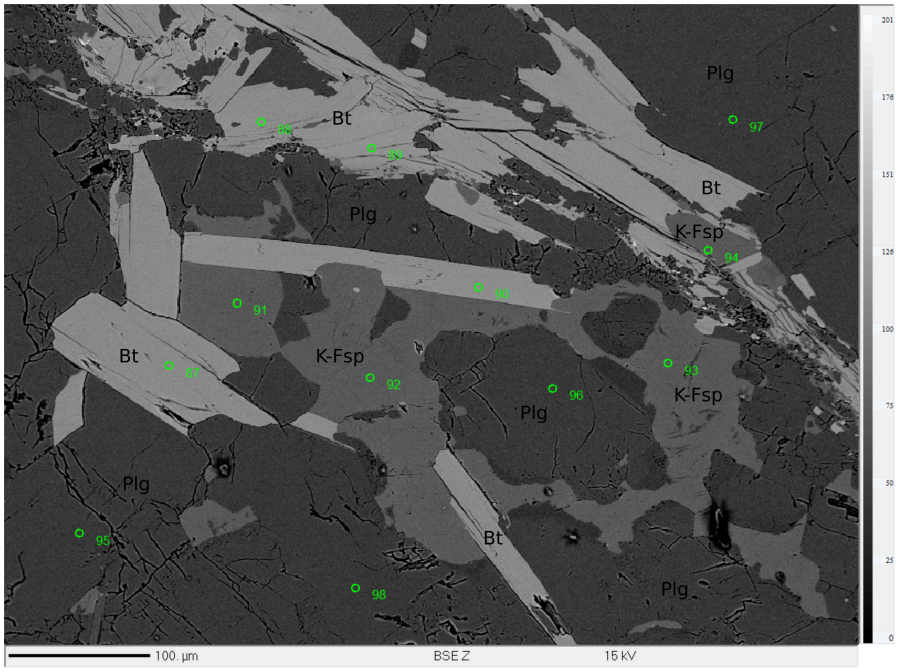

Figure B.17.: TH1612C1 A3

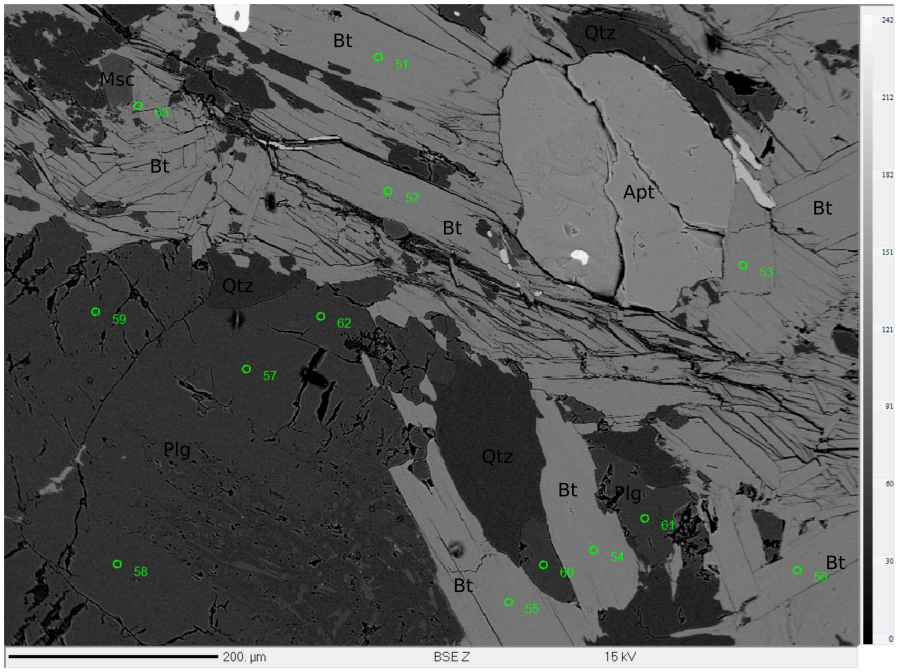

Figure B.18.: TH1612C2 A1

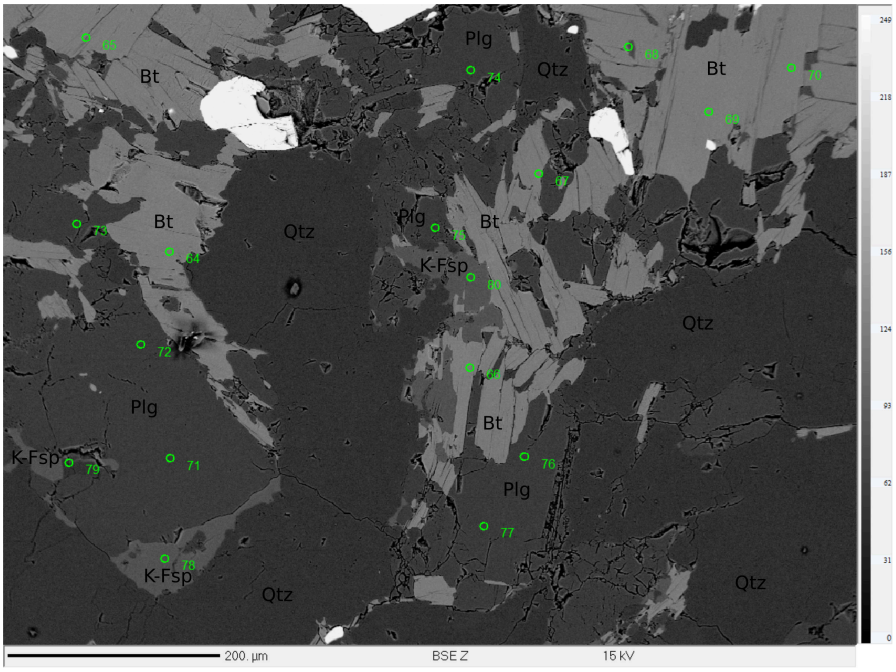

Figure B.19.: TH1612C2 A2

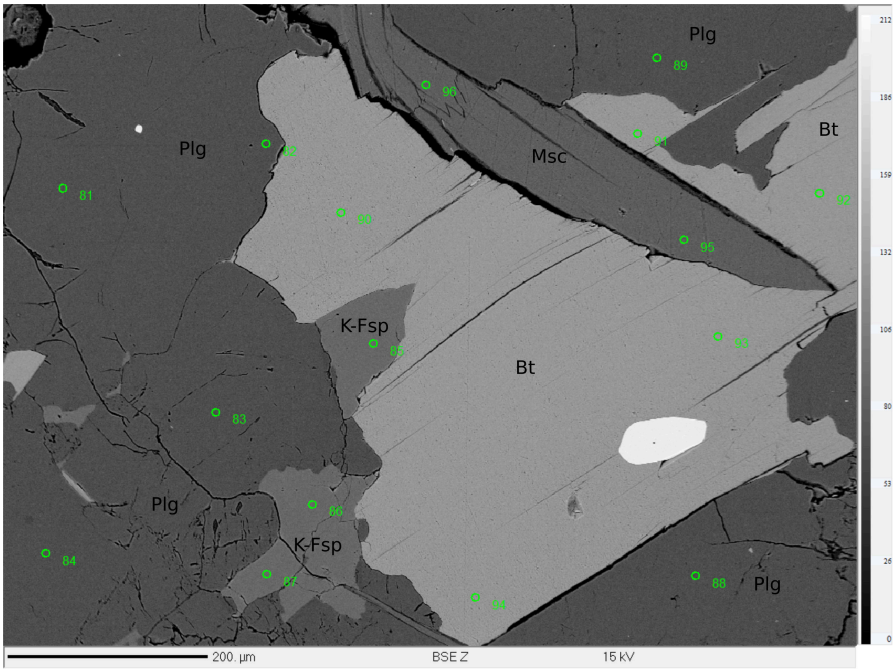

Figure B.20.: TH1612C2 A3

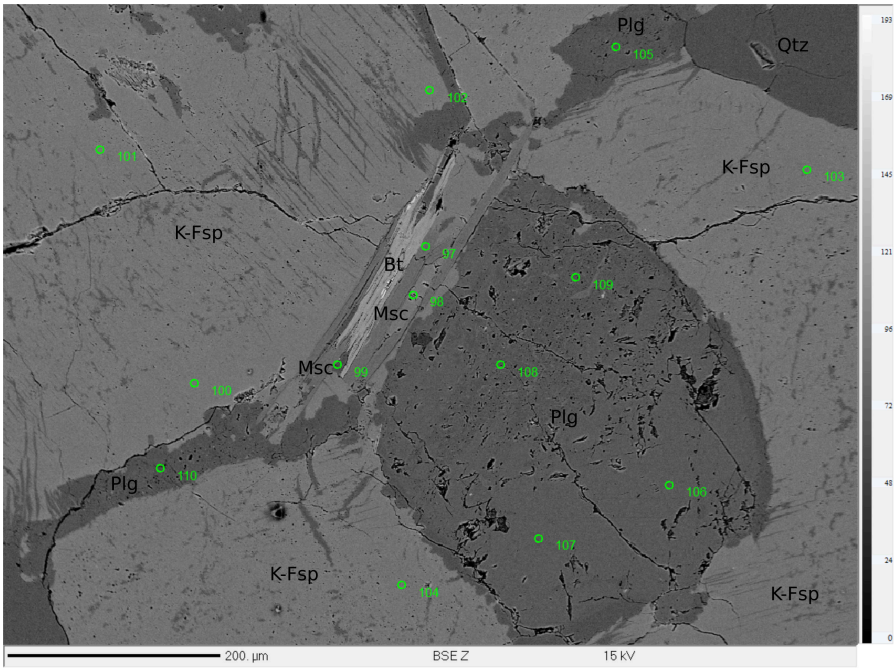

Figure B.21.: TH1612C2 A4

P2O5	CaO	La2O3	Ce2O3	Pr2O3	Nd2O3	Eu2O3	Sm2O3	Gd2O3	Comment	DataSet/Point
25.9511	1.1619	10.8373	23.6531	2.6417	9.6054	0.0051	1.768	1.3418	TH1608A1_mon1	46 / 1 .
25.4793	0.9104	10.3498	23.4351	2.6706	9.9257	0.0156	1.9024	1.464	TH1608A1_mon1	47 / 1 .
27.795	1.1467	11.4791	25.801	2.8844	10.9279	0.0263	2.0834	1.5117	TH1608A1_mon1	48 / 1 .
27.9674	1.2398	11.5606	26.0911	2.8342	10.4969	0.0446	1.9761	1.4146	TH1608A1_mon2	49 / 1 .
26.0507	0.8762	11.2709	24.8872	2.8015	10.4609	0.0373	1.8439	1.2739	TH1608A1_mon2	50 / 1 .
27.281	1.0629	12.4072	25.8158	2.961	10.6009	0.0018	2.021	1.4512	TH1608A1_mon2	51 / 1 .
28.9695	0.6125	13.0249	28.0198	3.1034	11.5279	0.016	2.2392	1.5834	TH1608A1_mon2	52 / 1 .
28.8063	0.5949	12.7888	28.0323	3.1444	11.6298	-0.0035	2.3029	1.656	TH1608A1_mon2	53 / 1 .
28.3296	0.9745	12.1761	27.2882	2.848	10.7509	0.0384	2.0468	1.4263	TH1608A1_mon2	54 / 1 .
28.3518	0.6956	12.6749	28.108	3.1312	11.2877	-0.0258	1.8891	1.3795	TH1608A2_mon11	29 / 1 .
27.6121	0.8745	11.5735	26.0864	2.8315	10.646	0.0071	1.9444	1.4582	TH1608A2_mon11	30 / 1 .
28.013	0.6533	13.1117	27.7596	3.0302	11.2885	0.0542	2.1238	1.4958	TH1608A2_mon11	31 / 1 .
28.8795	1.2494	12.4076	26.9458	2.8492	11.0406	0.0712	2.0402	1.7425	TH1608A2_mon3	01 / 1 .
26.4036	1.0706	10.7675	24.1767	2.6274	10.4427	0.0655	1.945	1.7337	TH1608A2_mon3	02 / 1 .
29.0686	0.6394	13.268	28.7105	3.0589	11.7549	0.0387	2.06	1.7885	TH1608A2_mon3	03 / 1 .
28.2936	1.2462	12.6896	27.0492	2.9569	10.8629	0.0197	2.0421	1.4487	TH1608A2_mon3_near pt1	04 / 1 .
28.7044	0.5242	12.9924	28.3823	3.147	11.766	0.0175	2.2011	1.5978	TH1608A2_mon4	05 / 1 .
25.9755	0.8955	11.1302	24.244	2.7518	10.0676	0.0249	1.9534	1.4318	TH1608A2_mon4	06 / 1 .
29.1059	0.5391	13.7886	28.7856	3.0728	11.2802	0.0284	2.0484	1.4101	TH1608A2_mon4	07 / 1 .
29.9297	0.3798	13.1054	29.7452	3.2917	12.4439	0.0382	2.4808	1.86	TH1608A2_mon6	27 / 1 .
28.4581	0.3691	13.5688	29.1042	3.2376	12.5916	0.011	2.2198	1.4235	TH1608A2_mon6	28 / 1 .
29.5371	0.308	13.9124	30.5561	3.3383	12.3332	0.0107	2.3842	1.6607	TH1608A2_mon6	32 / 1 .
28.8619	0.2843	14.0113	30.4253	3.2869	12.1738	0.0181	2.0521	1.3463	TH1608A2_mon6	33 / 1 .
28.6565	0.2444	13.7922	29.6047	3.2893	12.6804	0.012	2.2751	1.673	TH1608A2_mon6	34 / 1 .
28.5613	0.5974	12.9346	28.3655	3.0697	11.3823	0.0091	2.0647	1.4561	TH1608A2_mon7	35 / 1 .
29.4527	0.5674	13.6143	28.8238	3.0786	11.6013	0.0338	2.1652	1.5695	TH1608A2_mon7	36 / 1 .
28.846	0.9725	12.6779	27.0392	3.0205	11.1596	0.0263	2.132	1.4898	TH1608A2_mon7	37 / 1 .
28.9393	0.5638	13.4134	29.1528	3.1014	11.4045	0.0285	2.0547	1.4642	TH1608A2_mon7	38 / 1 .
28.1987	0.7289	12.842	28.0933	3.0709	11.3608	0.0204	2.131	1.473	TH1608A2_mon8	39 / 1 .

P2O5	CaO	La2O3	Ce2O3	Pr2O3	Nd2O3	Eu2O3	Sm2O3	Gd2O3	Comment	DataSet/Point
28.644	0.621	13.2909	28.3352	3.1465	11.8546	-0.001	2.2226	1.5774	TH1608A2_mon8	40 / 1 .
27.8238	0.9213	12.6952	27.254	2.9598	10.7769	0.0144	1.865	1.3781	TH1608A2_mon8	41 / 1 .
28.0359	0.7766	12.677	27.3221	2.9441	10.7894	0.0463	1.7673	1.3497	TH1608A2_mon8	42 / 1 .
28.4956	0.5737	13.8105	28.5654	3.0693	11.1727	0.0235	2.0001	1.3826	TH1608A2_mon8	43 / 1 .
28.0765	0.5957	13.091	28.0354	3.0502	11.1173	-0.0019	1.9429	1.4236	TH1608A2_mon8	44 / 1 .
27.3859	0.9015	12.3596	26.8683	2.9762	10.7933	-0.0007	1.9632	1.3577	TH1608A2_mon8	45 / 1 .
29.6636	0.2755	14.5261	30.3336	3.4085	12.7385	0.0363	2.3038	1.6542	TH1612C2_mon3	08 / 1 .
28.4193	0.7258	12.6741	27.5044	3.1369	11.7931	0.0572	2.2853	1.6707	TH1612C2_mon3	09 / 1 .
28.6281	1.7175	12.292	25.473	2.7654	10.3196	0.0603	1.9403	1.4051	TH1612C2_mon3	10 / 1 .
29.7223	1.81	12.1438	25.4379	2.8182	10.5147	0.032	2.0424	1.5512	TH1612C2_mon3	11 / 1 .
29.9089	2.0145	11.5542	24.7876	2.7618	10.3129	0.0214	2.0186	1.5926	TH1612C2_mon4	12 / 1 .
29.6863	2.2341	11.3047	23.9105	2.7103	10.1026	0.0413	2.0008	1.5553	TH1612C2_mon4	13 / 1 .
27.2072	0.8532	11.9771	25.5677	2.8935	10.7321	0.0695	2.0575	1.5484	TH1612C2_mon4	14 / 1 .
29.9438	2.0013	11.7375	24.9014	2.7825	10.4299	0.0182	1.9929	1.5699	TH1612C2_mon4_2	15 / 1 .
29.3899	1.9324	11.8575	25.1854	2.7295	10.6555	0.0401	2.0211	1.5551	TH1612C2_mon5	16 / 1 .
27.971	0.8679	12.8934	27.4	3.0052	11.3232	0.0397	2.1385	1.4807	TH1612C2_mon5	17 / 1 .
29.9433	1.7953	12.0035	25.5374	2.8645	10.61	0.0301	1.9886	1.5792	TH1612C2_mon6	18 / 1 .
29.4909	0.3242	14.1435	29.9338	3.3118	12.4678	0.0422	2.2699	1.5885	TH1612C2_mon6	19 / 1 .
28.4756	1.8597	11.3441	24.0082	2.6742	10.1532	0.0344	1.9474	1.4917	TH1612C2_mon7	20 / 1 .
29.0516	0.3735	13.7456	29.3069	3.2822	12.5278	0.0515	2.3791	1.6658	TH1612C2_mon7	21 / 1 .
29.8108	2.1562	11.5069	24.4416	2.6492	10.2098	0.0462	1.9142	1.5356	TH1612C2_mon7	22 / 1 .
29.3986	1.3564	12.1684	26.4449	3.0647	12.3954	0.014	2.0995	1.646	TH1612C2_mon8	23 / 1 .
29.2918	1.5373	12.7214	27.4761	3.0989	11.4742	0.0092	2.0473	1.2634	TH1612C2_mon8	24 / 1 .
28.2133	0.6196	12.496	28.0067	3.1571	12.0515	0.0095	2.378	1.8046	TH1612C2_mon8	25 / 1 .
29.4462	2.0479	11.5719	24.7204	2.7919	10.4418	0.0262	1.9681	1.583	TH1612C2_mon8	26 / 1 .

Table B.12.: EMPA measurements of monazite

Dy2O3	Er2O3	Y2O3	Lu2O3	ThO2	UO2	V2O3	SiO2	Total	Comment	DataSet/Point
0.6797	0.1735	2.379	0.0043	16.7548	0.7781		2.4219	100.1567	TH1608A1_mon1	46 / 1 .

Dy2O3	Er2O3	Y2O3	Lu2O3	ThO2	UO2	V2O3	SiO2	Total	Comment	DataSet/Point
0.6837	0.157	2.1831	0.005	17.5878	0.6539		2.8994	100.3227	TH1608A1_mon1	47 / 1 .
0.6306	0.136	1.9075	-0.0115	11.3077	0.3008		1.4165	99.3432	TH1608A1_mon1	48 / 1 .
0.6237	0.1281	1.8088	-0.024	11.7627	0.3842		1.3247	99.6336	TH1608A1_mon2	49 / 1 .
0.5827	0.1595	1.7737	-0.0116	15.371	0.4332		2.3713	100.1822	TH1608A1_mon2	50 / 1 .
0.6278	0.1242	1.8263	-0.0092	11.5499	0.3904		1.3522	99.4645	TH1608A1_mon2	51 / 1 .
0.7789	0.1789	2.6475	-0.016	5.9468	0.2184		0.7082	99.5592	TH1608A1_mon2	52 / 1 .
0.7041	0.1908	2.376	-0.0285	6.4176	0.2282		0.7737	99.6138	TH1608A1_mon2	53 / 1 .
0.5611	0.1308	1.7034	-0.0283	10.1716	0.263		1.2182	99.8986	TH1608A1_mon2	54 / 1 .
0.566	0.1578	2.1316	-0.0278	7.953	0.2816		1.0166	99.5708	TH1608A2_mon11	29 / 1 .
0.6579	0.1635	2.7175	-0.0007	10.9946	0.4947		1.6199	99.681	TH1608A2_mon11	30 / 1 .
0.5254	0.089	1.3545	-0.0359	8.5874	0.2142		1.2667	99.5314	TH1608A2_mon11	31 / 1 .
0.5043	0.164	1.7183	-0.015	9.4367	0.3114	-0.0039	1.0646	100.4066	TH1608A2_mon3	01 / 1 .
0.5521	0.1836	1.8802	-0.0161	15.6563	0.4675	-0.0017	2.4206	100.375	TH1608A2_mon3	02 / 1 .
0.4924	0.1683	1.8505	-0.0188	5.6003	0.2379	-0.0025	0.7634	99.4792	TH1608A2_mon3	03 / 1 .
0.5737	0.1039	1.7638	-0.0195	9.709	0.3233		1.168	100.231	TH1608A2_mon3_near pt1	04 / 1 .
0.6444	0.1262	2.0544	-0.0221	6.3156	0.2993		0.8677	99.6183	TH1608A2_mon4	05 / 1 .
0.6166	0.1839	2.1271	-0.0217	16.4327	0.53		2.7038	101.047	TH1608A2_mon4	06 / 1 .
0.5797	0.1165	1.7067	-0.0379	6.4527	0.2653		0.8841	100.0262	TH1608A2_mon4	07 / 1 .
0.7952	0.172	2.691	-0.0234	1.9306	0.1321		0.2289	99.2013	TH1608A2_mon6	27 / 1 .
0.4282	0.0749	1.1043	-0.0464	4.9598	0.224		1.1605	98.8891	TH1608A2_mon6	28 / 1 .
0.6283	0.0762	1.5718	-0.0288	2.2997	0.1751		0.3038	99.0668	TH1608A2_mon6	32 / 1 .
0.4723	0.0554	1.2622	-0.037	3.3503	0.1147		0.5298	98.2076	TH1608A2_mon6	33 / 1 .
0.5725	0.1041	1.3259	-0.0387	3.5167	0.1584		0.5681	98.4345	TH1608A2_mon6	34 / 1 .
0.5644	0.1159	1.6217	-0.0297	7.5918	0.2311		1.1267	99.6626	TH1608A2_mon7	35 / 1 .
0.6407	0.117	1.9433	-0.0293	5.2979	0.1877		0.6014	99.6654	TH1608A2_mon7	36 / 1 .
0.6171	0.1218	1.7347	-0.0239	8.893	0.2995		1.0405	100.0467	TH1608A2_mon7	37 / 1 .
0.5673	0.1144	1.7496	-0.0161	5.7238	0.2129		0.7004	99.1748	TH1608A2_mon7	38 / 1 .
0.6068	0.1124	1.7938	-0.023	7.7826	0.3011		1.05	99.5428	TH1608A2_mon8	39 / 1 .
0.6214	0.1173	1.8543	-0.0388	6.4468	0.2279		0.8362	99.7563	TH1608A2_mon8	40 / 1 .

Dy2O3	Er2O3	Y2O3	Lu2O3	ThO2	UO2	V2O3	SiO2	Total	Comment	DataSet/Point
0.6	0.1296	2.0082	-0.0163	9.8158	0.3083		1.2789	99.8129	TH1608A2_mon8	41 / 1 .
0.624	0.1596	2.2391	-0.013	9.7226	0.3125		1.3234	100.0767	TH1608A2_mon8	42 / 1 .
0.5717	0.0995	1.8398	-0.0401	6.4651	0.2385		0.8845	99.1523	TH1608A2_mon8	43 / 1 .
0.5484	0.1228	1.7831	-0.0254	8.1534	0.2898		1.266	99.4689	TH1608A2_mon8	44 / 1 .
0.5595	0.1205	1.6876	-0.0175	11.2978	0.2261		1.6264	100.1055	TH1608A2_mon8	45 / 1 .
0.5533	0.0628	1.4579	-0.0406	2.4083	0.2085		0.3057	99.8961	TH1612C2_mon3	08 / 1 .
0.597	0.0587	1.5957	-0.0136	8.26	0.2293		1.0612	100.0551	TH1612C2_mon3	09 / 1 .
0.5572	0.1036	1.68	-0.0249	11.7102	0.5655		0.7998	99.9926	TH1612C2_mon3	10 / 1 .
0.6879	0.1515	2.3052	-0.0149	9.06	1.3425		0.3006	99.9053	TH1612C2_mon3	11 / 1 .
0.7052	0.1241	2.3725	-0.0042	10.3719	1.3527		0.3667	100.2613	TH1612C2_mon4	12 / 1 .
0.7189	0.1571	2.2228	-0.0116	12.1109	1.0925		0.4289	100.2653	TH1612C2_mon4	13 / 1 .
0.5959	0.0972	1.6134	-0.0229	12.7277	0.3099		1.8965	100.124	TH1612C2_mon4	14 / 1 .
0.6769	0.1834	2.3796	-0.0131	10.0154	1.4051		0.298	100.3227	TH1612C2_mon4_2	15 / 1 .
0.7111	0.141	2.2858	-0.0071	9.6374	1.3175		0.3243	99.7765	TH1612C2_mon5	16 / 1 .
0.5541	0.0658	1.4995	-0.0147	8.5965	0.3433		1.0686	99.2326	TH1612C2_mon5	17 / 1 .
0.6796	0.1584	2.2518	-0.0191	9.0485	1.2572		0.3	100.0282	TH1612C2_mon6	18 / 1 .
0.5513	0.0714	1.3744	-0.0309	3.3915	0.1439		0.4493	99.5234	TH1612C2_mon6	19 / 1 .
0.6148	0.1107	1.8477	-0.012	14.2078	0.5605		1.1514	100.4694	TH1612C2_mon7	20 / 1 .
0.5889	0.0653	1.4255	-0.0291	4.1116	0.1671		0.5581	99.2715	TH1612C2_mon7	21 / 1 .
0.7122	0.1431	2.2223	-0.0102	11.5097	1.2104		0.3921	100.45	TH1612C2_mon7	22 / 1 .
0.6232	0.1058	2.3179	-0.0213	7.7023	0.2177		0.367	99.9004	TH1612C2_mon8	23 / 1 .
0.2771	0.0344	0.5853	-0.0165	9.355	0.3293		0.4961	99.9803	TH1612C2_mon8	24 / 1 .
0.5437	0.0775	1.1937	-0.0184	8.2527	0.1128		1.1147	100.0128	TH1612C2_mon8	25 / 1 .
0.716	0.1529	2.3749	-0.0139	10.418	1.4007		0.3311	99.9769	TH1612C2_mon8	26 / 1 .

Table B.13.: EMPA measurements of monazite

Appendix C. Thermobarometry

Table C.1.: Results hornblende-plagioclase thermometry and Al-in barometry

Amph	31 / 1 .	38 / 1 .	37 / 1 .	33 / 1 .	30 / 1 .	19 / 1 .	32 / 1 .	18 / 1 .
Plag	48 / 1.	46 / 1.	47 / 1.	46 / 1.	49 / 1.	27 / 1.	46 / 1.	27 / 1.
T (±35-40°C)	710.56	712.40	713.72	720.92	721.52	721.67	729.96	732.22
P(±0.6kbar)	6.70	6.13	6.35	6.09	5.93	6.25	5.80	5.67

Table C.2.: Results monazite-xenotime thermometry

DataSet/Point	T(°C)	Sample	Monazite
46 / 1 .	713,11	TH1608A1	Mnz1
47 / 1 .	675,30	TH1608A1	Mnz1
48 / 1 .	638,71	TH1608A1	Mnz1
50 / 1 .	596,10	TH1608A1	Mnz2
51 / 1 .	621,92	TH1608A1	Mnz2
49 / 1 .	614,31	TH1608A1	Mnz2
52 / 1 .	762,18	TH1608A1	Mnz4
53 / 1 .	718,31	TH1608A1	Mnz4
54 / 1 .	581,71	TH1608A1	Mnz4
02 / 1 .	626,45	TH1608A2	Mnz3
03 / 1 .	615,62	TH1608A2	Mnz3
04 / 1 .	600,68	TH1608A2	Mnz3
01 / 1 .	594,74	TH1608A2	Mnz3
06 / 1 .	662,94	TH1608A2	Mnz4
05 / 1 .	656,80	TH1608A2	Mnz4
07 / 1 .	578,70	TH1608A2	Mnz4
27 / 1 .	767,91	TH1608A2	Mnz6-1
28 / 1 .	401,38	TH1608A2	Mnz6-1
32 / 1 .	542,14	TH1608A2	Mnz6-2
33 / 1 .	448,93	TH1608A2	Mnz6-2
34 / 1 .	479,14	TH1608A2	Mnz6-3
36 / 1 .	636,61	TH1608A2	Mnz-7
38 / 1 .	587,99	TH1608A2	Mnz-7
37 / 1 .	599,16	TH1608A2	Mnz-7
35 / 1 .	557,40	TH1608A2	Mnz-7
41 / 1 .	645,11	TH1608A2	Mnz8

40 / 1 .	617,72	TH1608A2	Mnz8
39 / 1 .	600,56	TH1608A2	Mnz8
42 / 1 .	685,14	TH1608A2	Mnz9
45 / 1 .	574,47	TH1608A2	Mnz9
43 / 1 .	610,62	TH1608A2	Mnz9
44 / 1 .	594,86	TH1608A2	Mnz9
30 / 1 .	763,43	TH1608A2	Mnz11
29 / 1 .	666,67	TH1608A2	Mnz11
31 / 1 .	490,21	TH1608A2	Mnz11
08 / 1 .	514,34	TH1612C2	Mnz3
09 / 1 .	561,85	TH1612C2	Mnz3
10 / 1 .	603,07	TH1612C2	Mnz3
11 / 1 .	740,85	TH1612C2	Mnz3
14 / 1 .	567,61	TH1612C2	Mnz4-1
13 / 1 .	736,72	TH1612C2	Mnz4-1
12 / 1 .	755,37	TH1612C2	Mnz4-1
15 / 1 .	757,26	TH1612C2	Mnz4-2
17 / 1 .	537,42	TH1612C2	Mnz5
16 / 1 .	738,65	TH1612C2	Mnz5
19 / 1 .	491,24	TH1612C2	Mnz6
18 / 1 .	730,74	TH1612C2	Mnz6
21 / 1 .	511,08	TH1612C2	Mnz7
20 / 1 .	647,46	TH1612C2	Mnz7
22 / 1 .	731,49	TH1612C2	Mnz7
24 / 1 .	162,17	TH1612C2	Mnz8
25 / 1 .	439,73	TH1612C2	Mnz8
23 / 1 .	732,59	TH1612C2	Mnz8
26 / 1 .	756,81	TH1612C2	Mnz8

Appendix D. Geochronology

D.1. Monazite-EMPA data

Th	U	Pb	Y	intPb(Th)	intPb(Y)	intU(Th)	intU(-B)	Sample	Commnets
6.9759	0.3239	0.0997	1.7984	0.0102	0.0113	0.0748	0.0001	TH1608A1-2_mnz11/1	
10.0012	0.6355	0.1422	2.0786	0.0146	0.0131	0.1084	0.0003	TH1608A1-2_mnz11/2	
7.9430	0.3587	0.0479	1.3435	0.0116	0.0084	0.0855	0.0001	TH1608A1-2_mnz3/1	
12.2582	0.4872	0.0764	1.5009	0.0179	0.0094	0.1339	0.0002	TH1608A1-2_mnz3/2	
6.2493	0.2944	0.0893	1.6540	0.0091	0.0104	0.0669	0.0001	TH1608A1-2_mnz3/3	
11.7623	0.5592	0.0796	1.7672	0.0171	0.0111	0.1283	0.0002	TH1608A-2_mnz3/3	
11.4935	0.4803	0.0723	1.7165	0.0168	0.0108	0.1252	0.0002	TH1608A-2_mnz4/1	
6.3508	0.2820	0.0447	1.4784	0.0093	0.0093	0.0679	0.0001	TH1608A-2_mnz4/2	
1.2276	0.0933	0.0102	0.8901	0.0018	0.0055	0.0129	0.0000	TH1608A-2_mnz6/1	low Th
1.5921	0.1277	0.0227	1.8095	0.0023	0.0114	0.0168	0.0001	TH1608A-2_mnz6/2	low Th
4.5502	0.2278	0.0399	1.4481	0.0067	0.0091	0.0484	0.0001	TH1608A-2_mnz7/1	
7.1636	0.2773	0.0467	1.2938	0.0105	0.0081	0.0769	0.0001	TH1608A-2_mnz7/2	
4.3511	0.2140	0.0385	1.5730	0.0064	0.0099	0.0462	0.0001	TH1608A-2_mnz7/3	
5.8863	0.2907	0.0443	1.4290	0.0086	0.0090	0.0629	0.0001	TH1608A-2_mnz8/1	
6.7847	0.3076	0.0454	1.4301	0.0099	0.0090	0.0727	0.0001	TH1608A-2_mnz8/2	
8.7502	0.3253	0.0593	1.6096	0.0128	0.0101	0.0944	0.0001	TH1608A-2_mnz9/1	
8.3164	0.3514	0.0634	1.7097	0.0121	0.0107	0.0896	0.0001	TH1608A-2_mnz9/2	
10.9983	0.3998	0.0668	1.0740	0.0160	0.0067	0.1197	0.0001	TH1608A-2_mnz9/3	
9.3014	0.3624	0.0623	1.5740	0.0136	0.0099	0.1006	0.0001	TH1608A-2_mnz9/4	
11.0538	0.4775	0.0724	1.5614	0.0161	0.0098	0.1203	0.0002	TH1608A-2_mnz9/5	

Th	U	Pb	Y	intPb(Th)	intPb(Y)	intU(Th)	intU(-B)	Sample	Commnets
7.3463	0.4636	0.0562	1.3073	0.0107	0.0082	0.0789	0.0002	TH1612C-1_mnz3/1	crater
7.1627	0.2689	0.0512	1.1548	0.0105	0.0072	0.0769	0.0001	TH1612C-1_mnz3/2	crater
6.9576	0.2506	0.0585	1.2462	0.0102	0.0078	0.0746	0.0001	TH1612C-1_mnz3/3	
1.1198	0.1314	0.0188	1.0251	0.0017	0.0064	0.0118	0.0001	TH1612C-1_mnz3/4	low Th
8.6569	1.3208	0.0659	1.8670	0.0126	0.0118	0.0935	0.0006	TH1612C-1_mnz4-1	
10.2660	0.3340	0.0695	1.2501	0.0150	0.0078	0.1114	0.0001	TH1612C-1_mnz4-1	
8.3757	1.2058	0.0581	1.7455	0.0122	0.0110	0.0904	0.0006	TH1612C-1_mnz4-2	
8.9554	1.1584	0.0631	1.7676	0.0130	0.0112	0.0968	0.0005	TH1612C-1_mnz4-2	
12.5344	0.5987	0.0834	1.4228	0.0183	0.0089	0.1370	0.0002	TH1612C-1_mnz4-2	
9.0687	1.2316	0.0648	1.6561	0.0132	0.0105	0.0981	0.0006	TH1612C-1_mnz4-3	
11.5878	0.4159	0.0739	1.3537	0.0169	0.0085	0.1263	0.0001	TH1612C-1_mnz4-3	
4.9756	0.3222	0.0467	1.1524	0.0073	0.0073	0.0530	0.0001	TH1612C-1_mnz5/1	across zones
8.2191	1.2293	0.0616	1.7867	0.0120	0.0112	0.0886	0.0006	TH1612C-1_mnz5/2	
8.4719	1.2254	0.0679	1.8738	0.0124	0.0119	0.0914	0.0006	TH1612C-1_mnz5/3	
7.5592	0.7227	0.0519	1.4544	0.0110	0.0092	0.0813	0.0003	TH1612C-1_mnz6/1	
7.4927	1.0102	0.0535	1.7419	0.0109	0.0110	0.0806	0.0005	TH1612C-1_mnz6/2	
7.6542	1.2837	0.0571	1.8743	0.0112	0.0119	0.0823	0.0006	TH1612C-1_mnz6/3	crater
7.7711	0.3536	0.0972	0.4878	0.0113	0.0031	0.0837	0.0001	TH1612C-1_mnz7/1	
7.6695	0.1517	0.0634	1.0525	0.0112	0.0066	0.0824	0.0000	TH1612C-1_mnz7/2	
8.0575	1.2879	0.0601	1.8421	0.0118	0.0117	0.0868	0.0006	TH1612C-1_mnz7/3	
6.5131	0.3357	0.0596	1.0916	0.0095	0.0068	0.0697	0.0001	TH1612C-1_mnz7/4	crater
9.7306	1.3170	0.0705	1.9089	0.0142	0.0121	0.1055	0.0006	TH1612C-1_mnz7/5	

Table D.1.: Monazite-EMPA data

intPb(-B)	Lin-Exp	Ucorr	Pbcorr	Th2sigma	U2sigma	Pb2sigma	Sample	Commnets
0.0002	0.0076	0.2491	0.0748	0.0672	0.0128	0.0060	TH1608A1-2_mnz11/1	
0.0003	0.0078	0.5271	0.1108	0.0912	0.0141	0.0063	TH1608A1-2_mnz11/2	
0.0001	0.0076	0.2732	0.0262	0.0748	0.0129	0.0057	TH1608A1-2_mnz3/1	

intPb(-B)	Lin-Exp	Ucorr	Pbcorr	Th2sigma	U2sigma	Pb2sigma	Sample	Commnets
0.0001	0.0078	0.3533	0.0476	0.1091	0.0136	0.0058	TH1608A1-2_mnz3/2	
0.0002	0.0075	0.2276	0.0668	0.0614	0.0126	0.0059	TH1608A1-2_mnz3/3	
0.0001	0.0078	0.4309	0.0488	0.1049	0.0137	0.0058	TH1608A-2_mnz3/3	
0.0001	0.0078	0.3551	0.0423	0.1031	0.0136	0.0059	TH1608A-2_mnz4/1	
0.0001	0.0076	0.2141	0.0237	0.0622	0.0126	0.0057	TH1608A-2_mnz4/2	
0.0000	0.0073	0.0804	0.0018	0.0219	0.0117	0.0056	TH1608A-2_mnz6/1	low Th
0.0000	0.0074	0.1110	0.0045	0.0249	0.0119	0.0056	TH1608A-2_mnz6/2	low Th
0.0001	0.0075	0.1794	0.0216	0.0480	0.0124	0.0057	TH1608A-2_mnz7/1	
0.0001	0.0076	0.2004	0.0265	0.0687	0.0126	0.0057	TH1608A-2_mnz7/2	
0.0001	0.0075	0.1678	0.0192	0.0464	0.0122	0.0056	TH1608A-2_mnz7/3	
0.0001	0.0076	0.2278	0.0244	0.0586	0.0127	0.0057	TH1608A-2_mnz8/1	
0.0001	0.0076	0.2349	0.0244	0.0657	0.0127	0.0057	TH1608A-2_mnz8/2	
0.0001	0.0077	0.2309	0.0339	0.0813	0.0129	0.0057	TH1608A-2_mnz9/1	
0.0001	0.0076	0.2618	0.0375	0.0778	0.0129	0.0057	TH1608A-2_mnz9/2	
0.0001	0.0078	0.2801	0.0439	0.0991	0.0131	0.0058	TH1608A-2_mnz9/3	
0.0001	0.0077	0.2619	0.0366	0.0856	0.0130	0.0058	TH1608A-2_mnz9/4	
0.0001	0.0078	0.3572	0.0446	0.0995	0.0135	0.0059	TH1608A-2_mnz9/5	
0.0001	0.0076	0.3847	0.0357	0.0700	0.0132	0.0057	TH1612C-1_mnz3/1	crater
0.0001	0.0076	0.1920	0.0325	0.0685	0.0125	0.0057	TH1612C-1_mnz3/2	crater
0.0001	0.0076	0.1760	0.0391	0.0671	0.0125	0.0057	TH1612C-1_mnz3/3	
0.0000	0.0074	0.1196	0.0092	0.0211	0.0119	0.0056	TH1612C-1_mnz3/4	low Th
0.0001	0.0076	1.2273	0.0384	0.0805	0.0168	0.0057	TH1612C-1_mnz4-1	
0.0001	0.0077	0.2226	0.0458	0.0933	0.0127	0.0058	TH1612C-1_mnz4-1	
0.0001	0.0076	1.1155	0.0321	0.0783	0.0164	0.0057	TH1612C-1_mnz4-2	
0.0001	0.0076	1.0616	0.0361	0.0829	0.0161	0.0057	TH1612C-1_mnz4-2	
0.0001	0.0079	0.4617	0.0551	0.1113	0.0139	0.0059	TH1612C-1_mnz4-2	
0.0001	0.0076	1.1335	0.0388	0.0838	0.0165	0.0057	TH1612C-1_mnz4-3	
0.0001	0.0077	0.2896	0.0474	0.1038	0.0132	0.0058	TH1612C-1_mnz4-3	
0.0001	0.0075	0.2692	0.0308	0.0514	0.0128	0.0057	TH1612C-1_mnz5/1	across zones
0.0001	0.0076	1.1408	0.0355	0.0770	0.0164	0.0057	TH1612C-1_mnz5/2	

intPb(-B)	Lin-Exp	Ucorr	Pbcorr	Th2sigma	U2sigma	Pb2sigma	Sample	Commnets
0.0001	0.0076	1.1340	0.0405	0.0791	0.0165	0.0057	TH1612C-1_mnz5/3	
0.0001	0.0076	0.6414	0.0297	0.0718	0.0144	0.0057	TH1612C-1_mnz6/1	
0.0001	0.0076	0.9297	0.0286	0.0713	0.0155	0.0057	TH1612C-1_mnz6/2	
0.0001	0.0076	1.2014	0.0308	0.0723	0.0164	0.0057	TH1612C-1_mnz6/3	crater
0.0002	0.0076	0.2700	0.0845	0.0735	0.0129	0.0059	TH1612C-1_mnz7/1	
0.0001	0.0077	0.0693	0.0450	0.0727	0.0122	0.0058	TH1612C-1_mnz7/2	
0.0001	0.0076	1.2011	0.0336	0.0757	0.0167	0.0057	TH1612C-1_mnz7/3	
0.0001	0.0076	0.2660	0.0425	0.0635	0.0127	0.0058	TH1612C-1_mnz7/4	crater
0.0001	0.0076	1.2115	0.0411	0.0891	0.0169	0.0058	TH1612C-1_mnz7/5	

Table D.2.: Monazite-EMPA data

D.2. Zircon-SIMS data

					conventional concordia columns (Pbc corr.)					
Sample/ spot #	[U] ppm	[Th] ppm	[Pb] ppm	Th/U meas	207Pb 235U	±s %	206Pb 238U	±s %	r	Disc. % conv.
Th1608/036a	409	6	[14]	0.014	0.23973	3.59	0.0332	1.54	0.42962	-30
Th1608/031a	581	14	[19]	0.023	0.22891	2.74	0.0325	1.51	0.55157	-15
Th1608/042a	287	4	10	0.015	0.22756	3.86	0.0325	1.52	0.39497	-11
Th1608/030b	3024	9	[107]	0.003	0.23760	2.01	0.0339	1.51	0.75050	-9
Th1608/032a	1277	20	[45]	0.016	0.23645	2.40	0.0338	1.51	0.62864	-6
Th1608/036c	740	6	[25]	0.008	0.23134	2.36	0.0331	1.51	0.63835	-6
Th1608/043a	885	5	[30]	0.005	0.22823	2.74	0.0328	1.51	0.55109	-5
Th1608/041	771	12	27	0.015	0.22684	2.33	0.0327	1.51	0.64748	0
Th1608/035a	1257	9	[44]	0.007	0.23544	2.10	0.0339	1.50	0.71710	0
Th1608/043b	574	10	[19]	0.018	0.22652	2.80	0.0327	1.53	0.54741	2
Th1608/032b	528	4	18	0.007	0.22580	3.15	0.0327	1.50	0.47767	4
Th1608/035b	2679	6	94	0.002	0.23014	1.89	0.0333	1.50	0.79310	6

					conventional concordia columns (Pbc corr.)					
Sample/ spot #	[U] ppm	[Th] ppm	[Pb] ppm	Th/U meas	207Pb 235U	±s %	206Pb 238U	±s %	r	Disc. % conv.
Th1608/042c	614	11	[21]	0.017	0.22927	2.76	0.0332	1.51	0.54580	7
Th1608/030a	2734	7	97	0.002	0.23384	1.86	0.0339	1.50	0.80615	8
Th1608/036b	59	1	3	0.017	0.36987	5.32	0.0515	1.68	0.31550	13
Th1608/032c	4373	8	158	0.002	0.23575	1.67	0.0344	1.50	0.89755	21
Th1608/042b	276	3	10	0.013	0.22329	3.34	0.0328	1.53	0.45718	29
Th1608/031b	396	8	[13]	0.020	0.21754	3.95	0.0322	1.54	0.38941	36
Th1611/011a	117	5	[1]	0.046	0.03011	68.10	0.0082	1.82	0.02670	104
Th1611/018a	416	8	[4]	0.020	0.06471	7.28	0.0100	1.50	0.20665	53
Th1611/019a	484	10	[5]	0.020	0.04452	33.53	0.0104	1.54	0.04587	107
Th1611/019b	478	13	[5]	0.026	0.07227	5.18	0.0108	1.53	0.29622	-48
Th1611/020a	36	1	[3]	0.016	0.65087	5.57	0.0792	2.75	0.49352	-17
Th1611/021a	6742	3	244	0.000	0.23743	1.62	0.0345	1.50	0.92629	16
Th1611/021b	139	3	[9]	0.022	0.47817	5.00	0.0638	1.61	0.32184	3
Th1611/023a	3397	2	[31]	0.000	0.05888	2.34	0.0090	1.50	0.64175	-26
Th1611/023b	73	3	[0]	0.040	0.04574	47.98	0.0082	1.76	0.03662	116
Th1611/025a	109	2	9	0.019	0.61899	3.37	0.0802	1.64	0.48500	11
Th1611/025b	922	11	78	0.012	0.62640	1.91	0.0795	1.52	0.79287	-1
Th1611/027a	319	13	[3]	0.041	0.04971	12.78	0.0094	1.50	0.11736	114
Th1611/027b	323	14	[3]	0.044	0.06475	8.43	0.0096	1.51	0.17879	-60
Th1611/028a	283	13	[3]	0.045	no data	no data	0.0108	2.29	no data	no data
Th1611/029a	1480	30	18	0.020	0.07497	3.35	0.0114	2.13	0.63721	-2
Th1611/029b	1244	1	16	0.001	0.07296	6.97	0.0118	2.02	0.28943	234
Th1611/029c	1401	4	[21]	0.003	0.09950	7.19	0.0143	5.12	0.71213	-59
Th1612/073a	1339	3	48	0.003	0.23304	2.51	0.0340	1.51	0.59951	17
Th1612/073b	606	5	[21]	0.009	0.22946	2.74	0.0332	1.51	0.55282	5
Th1612/073c	614	2	21	0.004	0.23151	3.24	0.0328	1.51	0.46701	-16
Th1612/076a	129	2	4	0.016	0.22664	5.92	0.0314	1.59	0.26850	-34

					conventional concordia columns (Pbc corr.)					
Sample/ spot #	[U] ppm	[Th] ppm	[Pb] ppm	Th/U meas	207Pb 235U	±s %	206Pb 238U	±s %	r	Disc. % conv.
Th1612/076b	585	2	20	0.004	0.23097	2.57	0.0330	1.51	0.58908	-10
Th1612/077a	384	6	[70]	0.016	1.73722	1.80	0.1698	1.51	0.84199	-4
Th1612/081a	1256	7	[44]	0.006	0.23437	2.31	0.0334	1.53	0.66310	-10
Th1612/081b	624	5	[21]	0.008	0.22593	2.69	0.0323	1.50	0.55865	-11
Th1612/081c	611	4	22	0.006	0.23896	2.88	0.0340	1.51	0.52640	-10
Th1612/102a	1232	5	[42]	0.004	0.22409	2.16	0.0324	1.51	0.70079	3
Th1612/102b	177	2	6	0.013	0.23515	4.08	0.0331	1.50	0.36801	-20
Th1612/102c	1477	3	51	0.002	0.22967	2.02	0.0331	1.54	0.76137	1
Th1612/103a	438	3	15	0.006	0.22419	2.87	0.0328	1.52	0.52869	17
Th1612/103b	628	6	22	0.009	0.22439	2.55	0.0327	1.51	0.58960	13
Th1612/103c	853	5	[29]	0.006	0.22294	2.56	0.0324	1.51	0.59053	8
Th1612/112a	861	4	[30]	0.005	0.23405	2.40	0.0336	1.50	0.62651	-1
Th1612/112b	314	6	11	0.018	0.23909	3.35	0.0335	1.52	0.45511	-23
Th1612/112c	631	1	[21]	0.002	0.15007	29.52	0.0319	1.50	0.05085	128

Table D.3.: Zircon SIMS data

	TW concordia columns (Pbc corr.)				TW concordia columns (Pbc uncorr.)			
Sample/ spot #	238U 206Pb	±s %	207Pb 206Pb	±s %	238U 206Pb	±s %	207Pb 206Pb	±s %
Th1608/036a	30.086	1.54	0.05231	3.24	30.055	1.54	0.05313	2.99
Th1608/031a	30.727	1.51	0.05101	2.29	30.703	1.51	0.05164	2.09
Th1608/042a	30.785	1.52	0.05081	3.55	30.785	1.52	0.05081	3.55
Th1608/030b	29.528	1.51	0.05088	1.33	29.523	1.51	0.05101	1.31
Th1608/032a	29.575	1.51	0.05072	1.86	29.565	1.51	0.05099	1.81
Th1608/036c	30.168	1.51	0.05062	1.82	30.163	1.51	0.05076	1.79
Th1608/043a	30.504	1.51	0.05049	2.29	30.459	1.51	0.05166	2.00

	TW concordia columns (Pbc corr.)				TW concordia columns (Pbc uncorr.)			
Sample/ spot #	238U 206Pb	±s %	207Pb 206Pb	±s %	238U 206Pb	±s %	207Pb 206Pb	±s %
Th1608/041	30.567	1.51	0.05029	1.77	30.567	1.51	0.05029	1.77
Th1608/035a	29.532	1.50	0.05043	1.46	29.517	1.50	0.05084	1.37
Th1608/043b	30.556	1.53	0.05020	2.34	30.520	1.53	0.05112	2.05
Th1608/032b	30.580	1.50	0.05008	2.77	30.580	1.50	0.05008	2.77
Th1608/035b	30.009	1.50	0.05009	1.15	30.009	1.50	0.05009	1.15
Th1608/042c	30.096	1.51	0.05004	2.31	30.072	1.51	0.05067	2.13
Th1608/030a	29.530	1.50	0.05008	1.10	29.530	1.50	0.05008	1.10
Th1608/036b	19.408	1.68	0.05206	5.05	19.408	1.68	0.05206	5.05
Th1608/032c	29.065	1.50	0.04970	0.74	29.065	1.50	0.04970	0.74
Th1608/042b	30.442	1.53	0.04930	2.97	30.442	1.53	0.04930	2.97
Th1608/031b	31.098	1.54	0.04906	3.63	30.971	1.54	0.05228	2.48
Th1611/011a	122.233	1.82	0.02669	68.08	115.717	1.52	0.06982	7.78
Th1611/018a	99.855	1.50	0.04686	7.12	99.321	1.51	0.05108	4.42
Th1611/019a	96.006	1.54	0.03100	33.49	93.938	1.50	0.04833	8.75
Th1611/019b	92.872	1.53	0.04868	4.95	92.719	1.53	0.04998	4.05
Th1611/020a	12.630	2.75	0.05962	4.85	12.628	2.75	0.05977	4.83
Th1611/021a	28.971	1.50	0.04989	0.61	28.971	1.50	0.04989	0.61
Th1611/021b	15.674	1.61	0.05436	4.74	15.634	1.61	0.05637	2.84
Th1611/023a	111.371	1.50	0.04756	1.79	111.316	1.50	0.04796	1.68
Th1611/023b	121.429	1.76	0.04028	47.95	116.900	1.52	0.06994	10.30
Th1611/025a	12.469	1.64	0.05598	2.95	12.469	1.64	0.05598	2.95
Th1611/025b	12.573	1.52	0.05712	1.17	12.573	1.52	0.05712	1.17
Th1611/027a	106.523	1.50	0.03840	12.69	105.423	1.50	0.04663	5.40
Th1611/027b	104.514	1.51	0.04908	8.29	103.913	1.50	0.05360	5.06
Th1611/028a	92.672	2.29	no data	no data	87.862	1.80	0.05593	9.80
Th1611/029a	87.369	2.13	0.04751	2.58	87.369	2.13	0.04751	2.58
Th1611/029b	85.006	2.02	0.04498	6.67	85.006	2.02	0.04498	6.67

	TW concordia columns (Pbc corr.)				TW concordia columns (Pbc uncorr.)			
Sample/ spot #	238U 206Pb	±s %	207Pb 206Pb	±s %	238U 206Pb	±s %	207Pb 206Pb	±s %
Th1611/029c	70.052	5.12	0.05055	5.05	70.039	5.12	0.05070	5.02
Th1612/073a	29.442	1.51	0.04976	2.01	29.442	1.51	0.04976	2.01
Th1612/073b	30.108	1.51	0.05010	2.28	30.083	1.51	0.05074	2.07
Th1612/073c	30.468	1.51	0.05116	2.86	30.468	1.51	0.05116	2.86
Th1612/076a	31.862	1.59	0.05237	5.70	31.862	1.59	0.05237	5.70
Th1612/076b	30.326	1.51	0.05080	2.08	30.326	1.51	0.05080	2.08
Th1612/077a	5.889	1.51	0.07419	0.97	5.887	1.51	0.07438	0.95
Th1612/081a	29.914	1.53	0.05085	1.73	29.889	1.53	0.05149	1.63
Th1612/081b	30.966	1.50	0.05074	2.23	30.942	1.50	0.05135	2.03
Th1612/081c	29.416	1.51	0.05098	2.44	29.416	1.51	0.05098	2.44
Th1612/102a	30.829	1.51	0.05011	1.54	30.817	1.51	0.05042	1.47
Th1612/102b	30.184	1.50	0.05148	3.79	30.184	1.50	0.05148	3.79
Th1612/102c	30.198	1.54	0.05030	1.31	30.198	1.54	0.05030	1.31
Th1612/103a	30.531	1.52	0.04964	2.44	30.531	1.52	0.04964	2.44
Th1612/103b	30.568	1.51	0.04975	2.06	30.568	1.51	0.04975	2.06
Th1612/103c	30.871	1.51	0.04992	2.06	30.820	1.51	0.05120	1.73
Th1612/112a	29.720	1.50	0.05045	1.87	29.696	1.50	0.05109	1.70
Th1612/112b	29.835	1.52	0.05174	2.98	29.835	1.52	0.05174	2.98
Th1612/112c	31.343	1.50	0.03411	29.48	30.738	1.53	0.04959	8.40

Table D.4.: Zircon SIMS data

Appendix E. Abstract E/DE

E.1. Abstract

Thailand is part of two main terranes which have their origins in the Gondwana continent, Sibumasu in the west and Indochina in the east. In between are the Inthanon Zone and the Sukhothai arc belt. Whereas this model was established for the northern part of the country and is now well accepted, its continuation to the south is still a matter of debate. Therefore the Khanom complex, a polymetamorphic complex located in Peninsular Thailand SE of Surat Thani first described by Kosuwan (1996) was examined. It contains gneisses, schists, calcsilicates, marbles and is crosscut by post-orogenic granites. The objective was to bring more clarity whether these rocks have a similar history to the high-grade metamorphic rocks in the north of the country or not. Petrological investigations combined with geochronological studies were carried out on two gneisses in this area (Haad Nai Phlao gneiss and Laem Thong Yang gneiss), to further understand the timing, metamorphic conditions and tectonic evolution of Peninsular Thailand. These gneisses mainly consist out of feldspar, quartz and two micas. Garnet and aluminosilicate which were described by Kosuwan (1996) could not be found. Whereas the Laem Thong Yang gneiss is coarse-grained and has big feldspar "Augen", the Haad Nai Phlao gneiss is fine to coarse-grained with interlayers of calcsilicate and fine-grained amphibole-bearing gneiss. In-situ CHIME (chemical Th–U–total Pb isochron method) monazite and $^{206}Pb/^{238}U$ zircon SIMS (secondary-ion mass spectrometry) dating was applied: two different events could be determined, one in the Late Triassic (∼210 Ma) the other in the Late Cretaceous (∼80 Ma). In addition Al-in-hornblende barometry (6.1 ± 0.6kbar) coupled with hornblende-plagioclase thermometry (720 ± 35-40°C) as well as Monazite–xenotime miscibility gap thermometry (∼400-770°C) were carried out. Results from this study suggest that the amphibole-bearing gneiss might be derived from the Khao Dat Fa gneiss and that the Haad Nai Phlao gneiss might be the result of contact metamorphism caused by the intrusion of the Khao Pret granite. Similar ages obtained from other metamorphic basement rocks in Thailand (e.g. Doi Inthanon metamorphic core complex) suggest that they are all part of the same tectonic entity (Sibumasu) and therefore share a similar tectono-metamorphic history.

E.2. Zusammenfassung

Thailand besteht geologisch aus zwei Krustenblöcken, die ihren Ursprung in Gondwana haben. Sibumasu im Westen und Indochina im Osten. Dazwischen liegen die Inthanon-Zone und der Sukhothai-Arc Gürtel. Während dieses Modell für den Norden des Landes etabliert wurde und mittlerweile gut akzeptiert ist, ist seine Fortsetzung nach Süden immer noch umstritten. Daher wurde der Khanom Komplex untersucht, ein polymetamorpher Komplex auf der Halbinsel Thailands, SE von Surat Thani, der erstmals von Kosuwan (1996) beschrieben wurde. Er enthält Gneise, Schiefer, Calcsilikate, Marmor und wird von postorogenen Graniten durchschnitten. Ziel war es klar zu stellen, ob diese Gesteine eine ähnliche Geschichte wie die hochgradig metamorphen Gesteine im Norden des Landes haben oder nicht. Petrologische Untersuchungen in Kombination mit geochronologischen Untersuchungen wurden an zwei Gneisen in diesem Gebiet durchgeführt (Haad Nai Phlao Gneis und Laem Thong Yang Gneis), um den Zeitpunkt, die metamorphen Bedingungen und die tektonische Entwicklung der Halbinsel Thailands besser zu verstehen. Diese Gneise bestehen hauptsächlich aus Feldspat, Quarz und zwei Glimmern. Granat und Aluminosilicat, welche von Kosuwan (1996) beschrieben wurden, konnten nicht gefunden werden. Während der Laem Thong Yang Gneis grobkörnig ist und große Feldspat-Augen hat, ist der Haad Nai Phlao Gneis fein bis grobkörnig mit Zwischenschichten aus Kalksilikat und feinkörnigem amphibolhaltigem Gneis. In-situ CHIME (chemische Th-U-gesamt-Pb-Isochron-Methode) Monazit-Datierung und $^{206}Pb/^{238}U$ Zirkon SIMS (Sekundärionen-Massenspektrometrie) Datierung wurden angewendet: Zwei verschiedene Ereignisse konnten bestimmt werden: eines in der späten Trias (∼210 Ma), das andere in der späten Kreidezeit (∼80 Ma). Zusätzlich wurden Al-in-Hornblende-Barometrie (6,1 ± 0,6kbar) gekoppelt mit Hornblende-Plagioklas-Thermometrie (720 ± 35-40°C) sowie Monazit-Xenotim-Mischbarkeitslückenthermometrie (∼400-770°C) durchgeführt. Die Ergebnisse dieser Studie legen nahe, dass der amphibolhaltige Gneis möglicherweise aus dem Khao Dat Fa Granit stammt und dass der Haad Nai Phlao Gneis das Ergebnis einer Kontaktmetamorphose ist, die durch das Eindringen des Khao Pret-Granits verursacht wird. Ähnliche Alter, welche in anderen metamorphen Gesteinen in Thailand gemessen wurden (z.B. metamorpher Kernkomplex von Doi Inthanon), legen nahe, dass sie alle Teil derselben tektonischen Einheit (Sibumasu) sind und daher eine ähnliche tektonometamorphe Geschichte aufweisen.